Institute of Biomechanics
Center of Biomedical Engineering
Kronesgasse 5-I
8010 Graz, Austria

Master Thesis

Mechanical Characterization of Microglia and Glioblastoma Cells

to achieve the degree of
Master of Science

Author: Lars Bollmann, BSc

Supervisors: University Lecturer Kristian Franze,
(*University of Cambridge*)
Professor Gerhard A. Holzapfel
(*Graz University of Technology*)

Head of Institute: Professor Gerhard A. Holzapfel

Contents

Abstract

There is increasing evidence that cell behaviour is not only controlled by biochemical but also by mechanical signaling. While the influence of mechanical stimuli on the behaviour of many cell types has been extensively elaborated, the effect on cells of the nervous system is less well understood. To fill this gap, I performed traction force experiments with microglial and glioblastoma cells on substrates of varying stiffness. Glioblastoma cells were derived from spatially different tumor fractions. Two setups, an upright and an inverted were used for imaging and the results compared. Furthermore, I investigated substrate stiffness-dependent changes of the actin network. In addition, I studied cell size and relative area explored by the cell as a function of substrate stiffness.

My results show that peak and average traction stresses of microglia fluctuate with time, increase with stiffness and saturate for substrates with a shear modulus of G' = 1 kPa. Microglial cell size increased with substrate stiffness. The smallest relative area explored by the cell was found for a substrate with G' = 300 Pa coinciding with the largest substrate deformations. The actin network of microglial cells showed substrate stiffness-dependent morphologies. While a spherical shape was found for microglia on softer substrates, a more spread morphology and an increasing number of processes were observed on the stiff substrates.

The traction stresses of glioblastoma cells from spatially different tumor fractions showed significant differences. This finding indicates that traction force measurements may be a mean to distinguish subgroups of glioblastoma cells. Furthermore, the actin network of glioblastoma cells changed with respect to substrate stiffness. The cells showed a round morphology on soft substrates and a more spread shape with two or three terminal ends on stiff substrates. In addition, dominant stress fibers were formed on stiff substrates. The relative area explored by the glioblastoma cells was significantly larger than for microglia.

Comparing the results from the upright and the inverted setup lead to the conclusion that upright microscopy can lead to imaging artifacts that result in wrong traction force microscopy results.

It can be concluded, that microglia and glioblastoma cells adapt their traction stresses to the stiffness of their environment. Maximal traction stresses are found for a substrate with G' = 1 kPa, a typical value for brain stiffness. Hence, both cell types can be considered mechanosensitive. Further studies investigating the mechanosensitivity of microglia and glioblastoma cells will reveal new insights into the function and malfunction of these cells.

Kurzfassung

Das Verhalten einzelner Zellen wird nicht nur von biochemischen, sondern auch von mechanischen Signalen bestimmt. Der Einfluss von mechanischen Stimuli auf das Verhalten von vielen Zelltypen wurde bereits auführlich in der Literatur beschrieben. In welchem Ausmaß Zellen des zentralen Nervensystems beeinflusst werden, ist jedoch weniger bekannt. Aus diesem Grund wurden Traktionskraft-Experimente mit Mikroglia- und Glioblastom-Zelllinien durchgeführt. Die Glioblastom-Zellen wurden unterschiedlichen Tumorregionen entnommen. Es wurden sowohl ein inverser als auch ein aufrechter Versuchsaufbau für die Bilderfassung verwendet und die jeweiligen Resultate verglichen. Die Abhängigkeit des Aktin-Gerüstes, der Zellfläche und des Bewegungs-Verhältnisses von der Substratsteifigkeit wurden untersucht. Das Bewegungs-Verhältnis beschreibt das Verhältnis von zeitlich summierten Zellprojektionen zur anfänglichen Zellfläche.

Die Ergebnisse dieser Arbeit zeigen, dass die Maximal- und Durchschnittswerte der Traktionskräfte von Mikroglia mit der Zeit schwanken, mit Substratsteifigkeit zunehmen und für ein Substrat mit einem Schubmodul von G' = 1 kPa ein Plateau erreichen. Die Zellfläche nahm mit Substratsteifigkeit zu und das kleinste Bewegungsverhältnis wurde für einen Schubmodul von G' = 300 Pa gefunden. Das Aktingerüst von Mikroglia zeigte eine von der Substratsteifigkeit abhängige Morphologie. Mikroglia nahmen auf weichen Substraten ein runde Form an. Auf steifen Substraten zeigten die Zellen eine ausgebreitete Morphologie mit einer zunehmenden Anzahl von Fortsätzen.

Die Traktionskräfte von Glioblastom-Zellen unterschiedlicher Tumorregionen zeigten statistisch signifikante Unterschiede. Dieses Resultat weist darauf hin, dass Traktionskraft-Experimente zur Unterscheidung von Untergruppen von Glioblastom-Zellen genutzt werden können. Das Aktingerüst von Glioblastom-Zellen zeigte Veränderungen in Abhängigkeit von der Substratsteifigkeit. Während auf weichen Substraten eine runde Form beobachtet wurde, zeigten sich auf steifen Substraten ausgebreitete Zellen mit zwei oder drei Endpunkten. Zusätzlich formten die Zellen auf steifen Substraten Stressfasern. Das Bewegungs-Verhältnis von Glioblastom-Zellen war signifikant größer als für Mikroglia.

Der Vergleich der Resultate vom aufrechten und inversen Versuchsaufbau ließen darauf schließen, dass ein aufrechter Versuchsaufbau zu Artefakten bei der Bildererfassung führen kann und so die Traktionskraft-Messungen verfälscht.

Abschließend lässt sich sagen, dass Mikroglia und Glioblastom-Zellen ihre Traktionskräfte der Steifigkeit ihrer Umgebung anpassen. Maximale Traktionskräfte wurden für einen Schubmodul von G' = 1 kPa gefunden. Dies ist ein typischer Wert für Gehirngewebe. Es lassen sich somit beide Zelltypen als mechanosensitiv beschreiben. Weiterführende Untersuchungen der Mechanosensitivität von Mikroglia und Glioblastom-Zellen versprechen neue Erkenntisse über die Funktion und die Fehlfunktion dieser Zellen zu liefern.

Acknowledgment

First of all, I want to thank the entire *Franze lab* at the University of Cambridge for providing an excellent working environment. This thesis would not have been able without the relentless support of Dr. Rajesh Shahapure. Many thanks to Eva Pillai and Sarah Foster for proof reading my thesis and for their numerous suggestions and recommendations.

In addition, I express my profound gratitude to my supervisors Dr. Kristian Franze and Professor Gerhard A. Holzapfel for their continuous guidance throughout my master thesis.

I am indebted to Kimberley Evans from the *Stem Cell Institute* of the University of Cambridge and Astrid Wengler from the *Cambridge Centre of Brain repair* for providing microglia and glioblastoma cells, respectively.

I want to thank the *Faculty of Computer Science and Biomedical Engineering* at Graz University of Technology and the *Austrian Agency for International Cooperation in Education and Research* (OeAD) for their financial support.

This thesis is dedicated to Anitha Andiappan, for enduring each step of the way with me and my parents, for their unconditional support.

1. Introduction

1.1. Microglia

Microglia are the resident immune cells of the central nervous system. They possess various functions during development, are essential for many physiological processes and play an important role in the course of many diseases. For example, microglial cells are believed to be involved in Parkinson disease, glioma and tumor invasion, multiple sclerosis, Alzheimer's disease, neuronal damage after stroke, neuropathic pain and the recovery after spinal cord injuries [1–5].

There is increasing evidence that cell behavior is not only driven by biochemical cues. Mechanical stimuli seem to play an essential role in determining cell fate, function and behavior [6–8]. Matrix or substrate stiffness was found to influence differentiation, migration, proliferation, formation of adhesion complexes and cell morphology [9, 10].

The acto-myosin cytoskeleton is thought to be a key component for the cells' ability to sense substrate stiffness [10]. The interplay of actin fibers and myosin motors promotes the contraction of the cell [11]. Focal adhesions couple the cell to the substrate and enable the generation of traction forces [12]. A variety of cellular mechanosensors, including stretch-activated ion channels and integrins, are believed to sense either strain or stress to initiate appropriate signaling cascades [13–15]. For example, Solon et al. showed that substrate stiffness influences polymerization and crosslinking of F-actin [16]. Therefore, a substrate-dependent actin network morphology is a strong indicator for the cell's ability to sense the stiffness of it's micro-environment.

It has been shown that endothelial cells and smooth muscle cells are capable of stiffness sensing [9]. Results from Moshayedi et al. suggest that microglia change their morphology and upregulate their gene expression with respect to substrate stiffness [17, 18]. However, how microglia mechanically adapt to substrate stiffness is currently not known. To fill this gap, I performed traction force experiments with microglial cells on substrates with varying stiffness. I acquired fluorescent images of the actin network to investigate substrate stiffness-dependent morphological changes. In addition, I compared and discussed traction force results for an upright and an inverted setup. Cell size and relative area explored by the cells during time-lapse imaging were investigated with respect to substrate stiffness.

1.2. Glioblastoma cells

Glioblastoma cells are derived from glioblastoma multiforme, the most common and deadly primary brain cancer [19]. The median survival of patients affected is approximately one year from the time of diagnosis [20]. Primary treatments include surgery, followed by radiotherapy or chemotherapy with modest effect on survival [21]. Even in the case of optimal therapy, the median survival is less than two years after the diagnosis [20]. The heterogeneity of cells from glioblastoma and their invasiveness are considered the main causes for the failure of available therapies [22]. Certain subgroups of glioblastoma cells are believed to contribute more to the tumor progression than others [19]. In recent years, researchers have become interested in the spatial heterogeneity of single tumors to identify cell characteristics that indicate invasiveness, aggressiveness and survivability [21].

New approaches for therapies include selectively targeting subpopulations of tumor cells by influencing the cellular micro-environment and the interactions between tumor cells and their surroundings [19]. These strategies are based on observations that the stiffness of the extracellular matrix has a major impact on the structure, motility and proliferation of glioma cells and therefore on the tumor progression [22].

Traction stress data of glioblastoma cells from spatially different tumor fractions may reveal a mean to differentiate subgroups. For this study, the glioblastoma cells were derived from three spatially different fragments of the tumor. The classification by Sottorovia et al. defines superficial fragments with (T1,T2) and deeper fragments with (T3,T4,...) [21]. Traction stresses could be linked to invasiveness and aggressiveness of these spatial subgroups.

I performed traction force experiments with glioblastoma cells from three different tumor fractions on substrates with varying stiffness. In addition, I observed substrate stiffness-dependent changes in the cytoskeleton of glioblastoma cells. Cell size and the relative area explored by the cells during time-lapse imaging were determined with respect to substrate stiffness.

2. Background

2.1. The nervous system

Microglia and glioblastoma cells are found in the nervous system. This section gives a brief overview of the nervous system and the cells involved.

The main function of the nervous system is to perceive, transmit and process signals across the body to control and regulate various processes within the organism. It can be divided into the central nervous system (CNS) and the peripheral nervous system (PNS). The CNS is composed of the brain, retina and spinal cord, while the PNS consists of all nervous tissue outside the aforementioned regions.

The fundamental cellular components of the nervous system are neurons and glial cells. Neurons are defined by their ability to transmit electrochemical signals. They form complex networks and make connections via synapses.

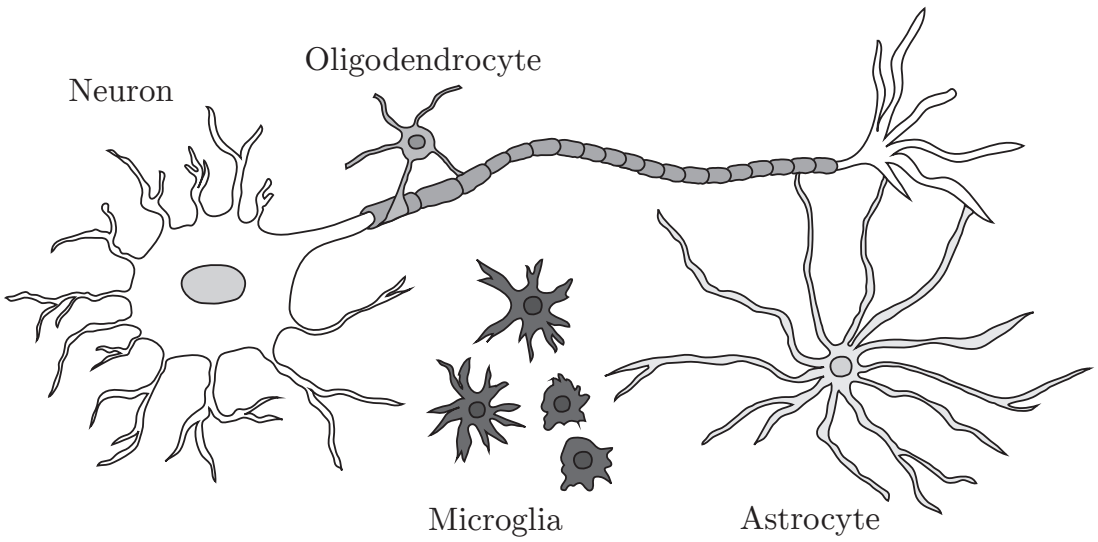

Figure 2.1.: Schematic drawing of a neuron and glial cells.

Glial cells (from the Greek word for 'glue') are not directly involved in the signal conveyance, but majorly contribute to the functionality and development of the signaling mechanism. One of the first studies mentioning the existence glial cells (or 'neuroglia') dates back to the year 1856 [23]. A significant proportion of cells in the brain is composed

of glial cells. Dombrowski et al. [24] showed that the ratio of neurons to glial cells in the brain of rhesus monkeys is approximately one, although there are variations across different areas of the brain. Studies suggest a similar ratio for humans [25]. The ratio of neurons and glial cells is also age and gender dependent [26].

In the CNS, four main types of glial cells can be identified: astrocytes, oligodendrocytes, ependymocytes and microglial cells (see Figure 2.1). They can be distinguished according to their morphology and function. Astrocytes show a star-like shape *in vivo*, hence the prefix 'astro' (from the Greek word '*astron*' for star). They have a large number of processes which contact neuronal cell bodies and blood vessels. Astrocytes fulfill numerous functions; they play an important role in axon guidance and in the regulation of pH and ion concentrations [27]. In addition, astrocytes are believed to be involved in neurovascular coupling [28]. Neurovascular coupling describes how a local neural activity influences the cerebral blood flow in adjacent regions.

Oligodendrocytes are smaller in size and show processes that contain a large number of microtubules. These microtubules might contribute to the stability of the processes [29]. Oligodendrocytes are mainly involved in the formation and maintenance of myelin sheaths which insulate the axons of neurons and greatly facilitate signal transmission. In addition to the myelin forming phenotype, there are also satellite oligodendrocytes [30].

Ependymocytes or ependymal cells surround the cerebrospinal fluid-filled spaces and are believed to play a major role in water and ion transport [31].

The fourth main group of glial cells is microglia. They appear in two different morphologies, namely the resting and the activated state [32]. Microglia are the immune cells of the nervous system and therefore respond to damage, foreign bodies, and pathogens.

2.2. Microglia

While the previous section dealt with the nervous system and described glial cells briefly, this section focuses on microglial cells and their importance in development, health and disease.

Microglia are very versatile cells of the CNS and are believed to be involved in many physiological and pathophysiological processes. In 1919, Rio-Hortega described their morphology, their morphological transformation in the presence of pathogens or injuries, and their capability to migrate, proliferate and perform phagocytosis for the first time [33, 34].

Microglia are thought to play an important role in development. Ferrer et al. showed that microglia perform phagocytosis to remove dead neurons as part of normal development [35]. One theory concerning the influence of microglia during development proposes that microglia may directly regulate neuronal cell death and survival [36]. In addition, microglia are likely to be involved in axonal guidance and growth [37].

In the mature CNS, microglia can be found in all regions of the brain and the spinal cord. They are often described as the resident immune cells of the CNS. *In vivo*, microglia show a ramified morphology in the absence of pathogens, injuries, diseases or foreign bodies [38]. This morphology with many motile processes is also referred to as the 'resting' state (see

Figure 2.2). Nimmerjahn et al. showed that 'resting' microglia probe their environment continuously with motile processes at their terminal ends [39]. Through various receptors microglia are able to sense minute changes in ion concentrations in their microenvironment and can detect signaling molecules [40]. Another important observation of Nimmerjahn's research was that within minutes of injury, microglia form a protective barrier which may shield the rest of the CNS [39]. The barrier between healthy and injured tissue may in some cases also be established by the extension of microglia processes without the movement of the cell bodies [41].

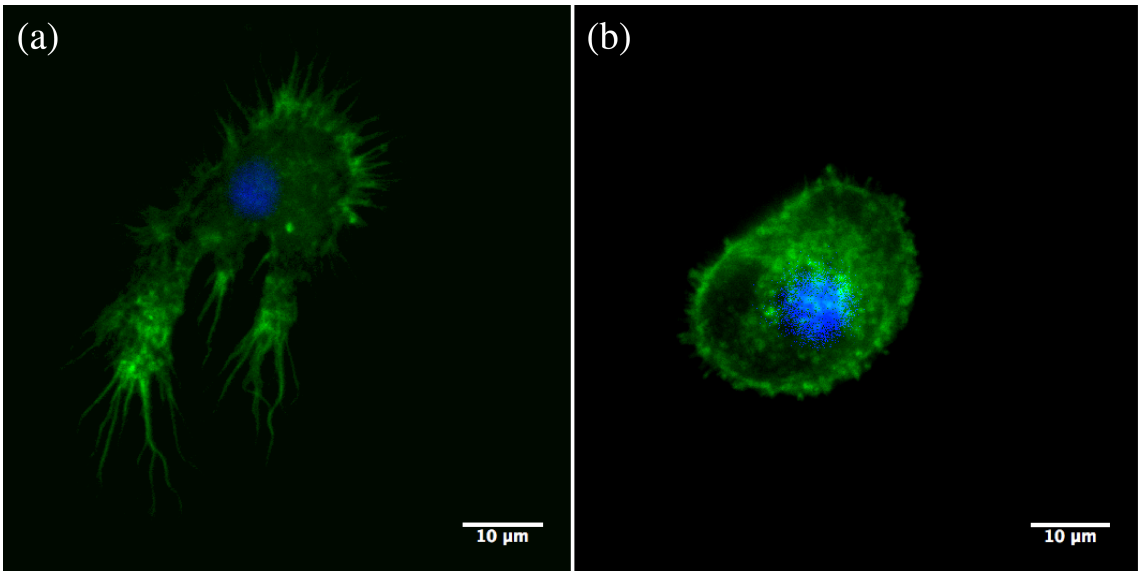

Figure 2.2.: Representative fluorescence images of two microglial cells. Actin is displayed in green, the nuclei appear in blue. Panel (a) shows a ramified morphology with many processes that is often associated with the 'resting' state of microglia. In panel (b) a microglial cell showing an amoeboid macrophage-like shape is displayed. This morphology is often found for 'activated' microglia.

The rapid transformation of microglia from the 'resting' to the 'activated' state is termed microglia activation. The activated phenotype shows an amoeboid macrophage-like shape (see figure 2.2) and is highly motile [42]. A variety of stimuli can trigger the microglia activation, including infections, damaged neurons, ischemia, tumors, trauma, (neurodegenerative) diseases or the presence of foreign bodies [17, 40, 43]. To simulate bacterial contamination under experimental conditions, lipopolysaccharides (LPS) are used [44,45]. LPS are large molecules that are found in the membrane of bacteria. In addition, neurons can promote microglia activation and deactivation through direct signalling [46]. Recent studies have identified different activation states in microglia that correspond to distinct functions [47].

Once activated, microglia can upregulate the expression of potentially cytotoxic substances, proinflammatory cytokines, migrate and are able to perform phagocytosis [1, 48].

Microglia actively initiate apoptosis in neuronal cell cultures or increase neuronal survival through the secretion of various substances [49]. Studies also suggest that microglia can promote tissue repair and undergo proliferation [40]. Neumann et al. show that microglia clear tissue debris after injury to facilitate the regeneration [3]. Furthermore, microglia seem to be able to directly alter synaptic properties in the spinal cord [49]. A marked drawback of most studies is that they were performed *in vitro* and may not accurately reflect the *in vivo* behavior of microglial cells [48].

Since microglia take an active part in many processes of the nervous system, including neuroinflammation and neurodegeneration, they play an important role in many pathologies of the nervous system [50]. These pathologies include Parkinson's disease (PD), glioma and tumor invasion, multiple sclerosis (MS), Alzheimer's disease (AD), neuronal damage after stroke and neuropathic pain. The role of activated microglia has been investigated in diseases characterized by chronic inflammation, such as MS, AD and PD [1]. In MS, microglial cells are found in lesion sites, but seem to be unable to clear all myelin degradation products to facilitate recovery [2, 3].

In AD, microglia play a rather controversial role. On the one hand, microglia may be beneficial in clearing amyloid (abnormal proteins) deposits and secrete growth factors and anti-inflammatory, neuroprotective substances [50, 51]. In addition, they remove damaged cells and therefore promote recovery. On the other hand, over-activation can lead to secretion of neurotoxic substances, which may lead to increase in neuronal damage [51]. Moreover, the secretion of proinflammatory cytokines is believed to contribute to increased plaque formation which potentially leads to cognitive impairment [52].

It has been shown that microglia play a major role in the inflammatory response and the maintenance of chronic pain after a spinal cord injury [4, 5].
Several studies suggest that microglia functionality is altered with respect to organism age. For example, Zhao et al. point out that the remylination capability in the nervous system decreases with age and relate their findings to a change in the inflammatory response [53]. Besides, microglia show age-associated structural deterioration that is likely to lead to a partial dysfunction [54]. Streit et al. claim that microglial senescence might be a reason for impaired neuronal protection, which would eventually lead to neurodegeneration [55].

Microglia have been subjected to intense research, but many questions still remain unanswered. This study focuses on the influence of mechanical stimuli on microglial behaviour and how these cells interact with their surroundings mechanically.

2.3. Mechanics in the nervous system

In the previous section, the various functions and characteristics of microglia were discussed. It is very likely that besides biochemical signals, mechanical stimuli influence microglial cell behaviour as well. In this section, the importance of mechanics in numerous processes in the nervous system are described. In addition, the mechanical properties of the microglial environment are characterized.

During the development of the nervous system, the tissue and embedded cells grow and undergo rearrangements. The cells are deformed, confronted with changing boundary conditions and are exposed to different loads. Therefore, mechanics play an important role in the development of the nervous system [56]. In 1984, Bray outlined the influence of mechanics in axonal growth [57]. In his experiments, neurite elongation was promoted by applying tension through microcapillaries. In another study, Betz et al. [58] demonstrated that growth cones at the tips of developing axons constantly exert forces on their environment. These results suggest that neurons can actively generate forces and respond to mechanical stimuli.

It has been shown that cells of the nervous system adjust their morphology and functionality to substrate stiffness. While primary microglial cells and astrocytes show a ramified morphology on stiffer substrates, a spherical morphology can be observed for both cell types on softer substrates [17, 18]. Moshayedi et al. found an upregulation of inflammatory genes and proteins due to increased substrate stiffness. Furthermore, their study reported an increased number of activated microglia close to stiffer regions of implanted foreign bodies in rat brains indicating an enhanced foreign body reaction. How cells sense mechanical properties of their surroundings is the subject of ongoing research. The concept of mechanosensitivity is further discussed in section 2.4.

The mechanical properties of a tissue are determined by the compliance of all constituents and their interactions. Besides neurons and glial cells, the CNS is composed of fluid-filled spaces (e.g. ventricles), blood vessels and the extracellular matrix.

Often white and gray matter are distinguished when it comes to mechanical characterization of the CNS. White matter consists largely of myelinated axons and can be found in the deeper brain and close to the surface of the spinal cord. Gray matter appears mainly in the depths of the spinal cord and close to the surface of the brain. In the gray matter, numerous neuronal and glial cell bodies and few myelinated axons are found. Studies applying large strain suggest that white matter is stiffer than gray matter,. Van Dommelen et al. measured a shear modulus G' of about 1000 Pa for white matter and 700 Pa for gray matter in porcine brains [59]. Absolute values vary significantly between studies. For small strains, as they are relevant to mechanosensing by cells, white matter appears to be softer than gray matter [60]. Properties of brain tissue are usually measured by indentation tests [59], shear deformation experiments [61], stress relaxation tests [62], magnetic resonance elastography [63, 64], atomic force microscopy (AFM) [65], scanning force microscopy [60] compression tests [66] or rheological experiments [67].

The sample preservation temperature prior to testing seems to have a considerable impact on its mechanical properties [68]. There are also modest differences in brain stiffness across species [62].

Brain tissue is often described as a viscoelastic material using parameters such as the storage modulus (G') and loss modulus (G''). The storage modulus represents the elastic part or energy-storing portion of the material. Across different studies values for the storage modulus range between 100 Pa and about 10 kPa with increasing values for higher frequencies [69]. The loss modulus accounts for dissipated energy or the viscous part. Values are on the order of 10^2 Pa and go up to an order of 10^5 Pa with increasing frequency [69].

Representative experimental results for brain tissue are displayed in Figure 2.3 [59, 66]. Panel (a) shows the stress-strain relationship from a compression test for cortical tissue of a swine brain after five pre-conditioning cycles. One loading-unloading curve was obtained at a frequency of $0.1s^{-1}$. It can be concluded that the tissue is highly nonlinear and shows stiffening and hysteresis. In panel (b) a representative result for an indentation experiment on anterior white matter of a porcine brain is presented. Likewise, non-linearity and hysteresis can be observed. Furthermore, the frequency-dependency of the mechanical response is highlighted.

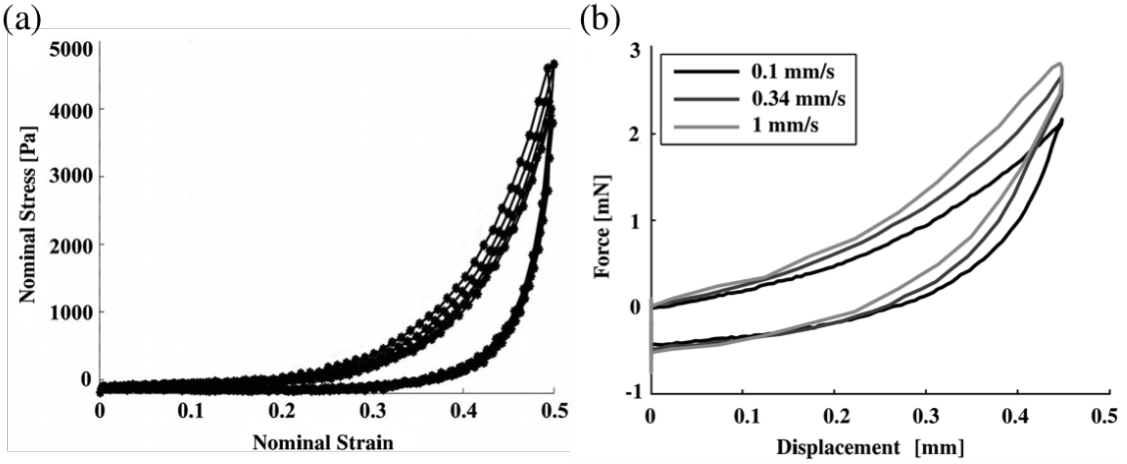

Figure 2.3.: Representative stress-strain curves from a compression test on cortical tissue of a swine brain are presented in panel (a). The displayed curves were recorded after five pre-conditioning cycles at a frequency of $0.1s^{-1}$. Figure adapted from [66]. Panel (b) shows the result of an indentation test on anterior white matter of a porcine brain (adapted from van Dommelen et al. [59]).

In recent years, researchers have started to consider hyperelastic models to capture the complex strain-dependent mechanical behavior of brain tissue. For hyperelastic models, strain-energy functions are defined in order to calculate stresses that arise from known deformations. [70].

In addition to mechanics at a macroscopic level, technological progress of the recent past promoted observations of mechanical behavior at a microscopic level. Researchers from multiple disciplines are trying to achieve a more complete understanding of mechanical properties and mechanical behavior of single cells.

2.4. Cell mechanics

The focus of this study lies on the mechanical characterization of single cells. Therefore, essential components for the active and passive mechanical behaviour of cells are portrayed in this section.

To understand the mechanical behavior and properties of cells as the essential building blocks of biological tissue, all structural components of the cell have to be taken into account. A schematic drawing of a cell with its basic structural constituents is presented in Figure 2.4. The outer boundary of a cell is defined by its membrane. This lipid bilayer

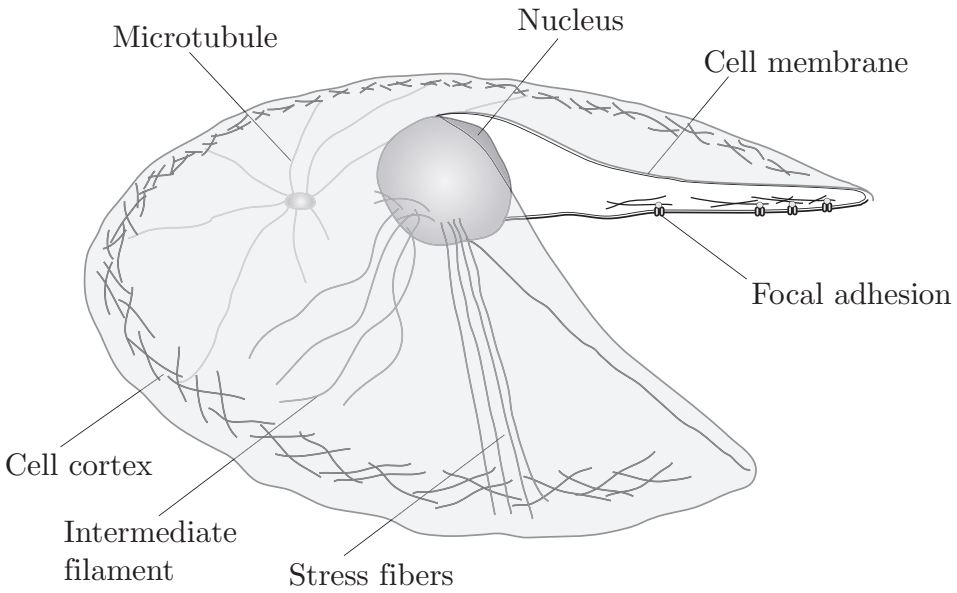

Figure 2.4.: Schematic drawing of a cell on a substrate showing cell components that majorly contribute to the cell's mechanical behaviour. The cytoskeleton is formed by microtubuli, intermediate filaments and the actin network. The actin network comprises stress fibers and the cell cortex. The cell membrane separates the cell from it's surrounding. Focal adhesions mechanically couple the cell cytoskeleton to the substrate.

is selectively permeable, consists of mainly phospholipids and contains various membrane proteins. Membrane proteins perform various functions such as active and passive transport of molecules and play an important role in signal transduction [71]. The bending modulus and the membrane tension are often used to characterize the mechanical properties of

the cell membrane. Pontes et al. [72] found that the bending modulus shows significant differences between activated and resting microglia, indicating that the compliance of the cell membrane changes with cell function. In addition, the membrane tension seems to be involved in cell shape and motility [73].

A cell nucleus is only found within eukaryotic cells. It is enclosed by a membrane and contains the major part of the cell's genetic material. According to Guilak et al. the cell nucleus behaves as a viscoelastic material [74]. Guilluy et al. showed that isolated cell nuclei adjust their stiffness in response to applied forces, indicating the existence of a mechanism for mechanotransduction [75].

The cytoplasm describes all components within the cell membrane apart from the nucleus. It includes the cytosol (intracellular fluid) and cell organelles, such as mitochondria, protein complexes, ribosomes and the cytoskeleton. Recent studies suggest that the cytoplasma can be described as a biphasic material, comprising a porous elastic meshwork and a fluid part [77].

The cytoskeleton is the major mechanical framework of the cell and consists of three structural components: microtubules, intermediate filaments (IFs) and actin. The mechanical behavior of the cell is strongly influenced by all three constituents and their interactions [78]. IFs have a diameter of approximately 10 nm, consist of different IF proteins depending on the cell type, and show a cylindrical morphology [79]. They are believed to majorly contribute to the cell's ability to withstand tensile strain [80]. Flitney et al. [81] found that cells with keratin IFs reorganize their IF network in response to applied forces to resist shear stress. IFs appear in different conformations within cells. They can bind to each other through cross-linking or connect to actin filaments or microtubules to form networks [78].

Microtubules are made of tubulin dimers that form a hollow cylindrical structure with an outer diameter of approximately 25 nm. They are the most rigid component of the cytoskeleton and are believed to resist compressive loads [82]. Microtubules switch constantly between elongation through polymerization and shortening through depolymerization ('dynamic instability') [83]. Microtubules can form bundles by connecting through kinesin motors and binding proteins [84]. The combination of kinesin motors and changing microtubule length promotes the generation of forces [85]. In addition, Karafyllidis et al. hypothesized the hypothesis that microtubules might also act as mechanical force sensors [86].

The third cytoskeletal component is actin with an approximate diameter of 7 nm . Actin filaments (*F*-actin) are double-stranded helices composed of the globular protein *G*-actin [87]. They can elongate through the polymerization of *G*-actin by consuming adenosine-triphospate (ATP). The reversible process of depolymerization is promoted by dissociating actin monomer groups. Polymerization and depolymerization depend on the concentration of free actin monomers [87]. In addition, actin filaments show polarity that influences their assembly and transport.

Actin filaments appear in different conformations within the cell. They can form actin networks through cross-linking [88]. These networks are mainly found in the cell cortex.

In addition, actin filaments can bundle to so-called stress fibers that span across the cell (see Figure 2.4). Actin networks show isotropic visco-elastic behavior and stabilize the cell [89]. Furthermore, the actin network and complementary myosin motors are thought to be involved in cell contractility [11]. Reymann et al. outlined that actomyosin contractility directly influences actin network assembly [90].

In order to exert forces, the cell needs to establish a connection with its surrounding and has to deform. During this process, the cytoskeleton and adhesion sites play an important role. It is believed that the interplay of the aforementioned components enables the cell to sense the stiffness of the local environment [91]. The sensing of mechanical cues and the coupling of mechanical input to biochemical signals is referred to as ”mechanosensitivity”. A common model for the generation of traction by cells is the "motor-clutch" mechanism [91]. The model incorporates F-actin filament bundles that are pulled by molecular motors. A linear force-velocity relationship is used for the motors. Molecular clutches couple the actin filaments to the substrate outside the cell (see figure 2.4). The clutch dynamics are substrate stiffness-dependent. The implementation of the ”motor-clutch” model by Chan et al. explains the cell’s capability to sense and respond to changes in microenvironment stiffness [91]. Experimental results also indicate that substrate stiffness majorly influences the generation of traction forces [92]. In addition, actin polymerization seems to significantly contribute to the exertion of forces [93]. Traction forces are important for various physiological processes including cell migration [94, 95].

3. Methods

3.1. Substrates

Polyacrylamide (PAA) gels with embedded fluorescent beads (*FluoSpheres carboxylate*, 0.2 μm, crimson, Life Technologies, UK) were synthesized on an imaging dish (μ-Dish, Ibidi, Germany) as substrates for cell culture and TFM measurements. The methodology was based on the protocol established by Grevesse et al. [96]. First, the dish was cleaned with 70% ethanol and its surface made hydrophilic with 0.1% sodium hydroxide (NaOH, all chemicals by Sigma-Aldrich Co, UK unless stated otherwise). (3-Aminopropyl)trimethoxysilane (APTMS) was applied for a duration of 3 minutes to the NAOH treated dishes. APTMS facilitates the formation of strong bonds between the dishes and the gel. The dish was then covered with 10% glutaraldehyde for 30 minutes to permit the chemical crosslinking of the PAA gel.

The PAA gel solutions of varying stiffness were made according to table 3.1. The stiffnesses used were selected within the physiological range of brain tissue stiffness. Atomic force microscopy (AFM) measurements were performed to determine the accurate fractions of phosphate buffered saline (PBS), gel premix and fluorescent beads for PAA gels with a defined elasticity. The gel premix consisted of 40% acrylamide (AA), 100% hydroxy-acrylamide (OH-AA) and 2% bis-acrylamide (Bis-AA, Fisher scientific, UK).

Stiffness (Shear modulus G')(Pa)	**Volume of 100% PBS** (μL)	**Volume of Gel Premix** (μL)	**Beads** (μL)
~ 100	437	53	10
~ 200	435	55	10
~ 300	432	58	10
~ 1000	415	75	10
~ 2000	400	90	10
~ 10000	340	150	10

Table 3.1.: Components of PAA gel solutions for different stiffness.

The final gel solution was placed in an ultrasonic bath for 30 seconds to separate the fluorescent beads and degassed under vacuum for 30 minutes. Adding N,N,N',N'-tetramethylethylenediamine (TEMED) and ammonium persulfate solution (APS) initiated the crosslinking of the gel. Immediately after the polymerization was started, 8 μl of the gel was pipetted on the treated imaging dish. A coverslip that had been cleaned and made hydrophobic was lowered onto the drop to create a gel layer of even thickness. The imaging

dish was then inverted to ensure bead movement towards the gel surface. Once the gel polymerized, the surface was covered with 100% PBS to facilitate removing the cover slip. The gels were subsequently washed and sterilized under UV light for approximately 15 minutes. To promote cell adherence, the gel surface was coated poly-D-lysine (PDL).

3.2. Preparation of cells

3.2.1. Microglia

All animal experiments as part of this study were conducted in accordance with the UK Animals (Scientific Procedures) Act (1986).

Neonatal P0-P2 rats were decapitated and their cortices dissected from the exposed brains. Microglia were obtained following Giulian et al. [97] and McCarthy et al. [98]. The cortices were cut into small pieces, minced and incubated in a cell dissociation solution containing papaya proteinase 1 (Papain, Sigma-Aldrich, UK) at 37 $^{\circ}C$ for 1 hour. To stop the papain digestion, an Ovomuccoid (Trypsin inhibitor, Sigma-Aldrich, UK) solution was added. The cell suspension was centrifuged at 1000 rpm for 8 min. The resulting pellet of cells was suspended in a mixed glia medium and incubated in PDL-coated T-75 flasks. The medium was changed every 2-3 days and the mixed glia were kept at 37 $^{\circ}C$ in an CO_2 - incubator. After 10 days, the flasks were shaken overnight at about 200 rpm using an orbital shaker to promote the detachment of microglia and oligodendrocyte precursor cells (OPCs). The medium containing the aforementioned cell types was removed leaving T-75 flasks with predominantly astrocytes. Separation of microglia and OPCs was achieved by pouring the suspension into an untreated plastic dish and incubating it for 30 minutes at 37 $^{\circ}C$. Microglia attach to plastic quickly and the medium containing OPCs was removed and replaced by fresh culturing medium. The resulting plastic dishes with microglia were provided by the *Stem Cell Institute* of the University of Cambridge.

To shake off the microglial cells, the plastic dish was placed on ice and shaken at 400 rpm on an orbital shaker for about 30 minutes. The cell suspension was then transferred to a 15 ml tube and centrifuged at 500 rpm for 1 minute. Subsequent to removing the supernatant, the cell pellet was resuspended using a culturing medium (Dubecco's Modified Eagle Medium (DMEM, Gibco)) and 10% fetal bovine serum (FBS) solution.

The cell suspensions were evenly distributed on the PAA gels and kept in a CO_2 - incubator for 10 minutes to allow for cell adhesion. An additional 2 ml of cell culture medium per imaging dish was then added to ensure cell survival. The cells were kept at 37 $^{\circ}C$ until imaging.

3.2.2. Glioblastoma cells

To derive spatially distinct primary tumour tissue samples, the tumour was divided into objectively defined regions. Superficial tumour fragments were labelled T1 and T2, the deeper tumour fragments were assigned T3 to T8 [21].

To obtain primary glioblastoma cell cultures, the Cambridge protocol by Fael Al-Mayhani et al. was used [99]. Briefly, human brain tumour tissue samples were collected shortly after surgery and minced using razor blades. The minced tissue was incubated with Accutase (Life Technologies, UK) for 45 minutes to 2 hours at $37°C$ to enzymatically digest the extracellular matrix (ECM). Hank's Balanced Salt Solution (HBSS) was added and a single-cell suspension was obtained using a cell strainer. The cells were then kept in cell culture flasks in serum free media (SFM, Life Technologies, UK). The media was changed every three days. After one week, the cells were centrifuged at 1200 rpm for 5 minutes and plated in ECM coated cell culture flasks with SFM. The cell culture was split when 80% confluency was reached.

The primary glioblastoma cell cultures were provided by the *Cambridge Centre for Brain Repair* at the University of Cambridge.

To detach the glioblastoma cells from the culture flask, 500 μl of Accutase was added for 5 minutes. After adding PBS, the cells were centrifuged at 1200 rpm for 5 min. The supernatant was removed and the cell pellet resuspended using a medium consisting of Neuro-basal A (Gibco, Life Technologies, UK), several growth factors (EGF, FGF, B27, N2, all Life Technologies, UK) and an antibiotic (PSF-1, zenbio, UK). The cell suspension was pipetted onto the PAA gels and additional medium was added after approximately 10 minutes. The cells were kept at $37°C$ until imaging.

3.3. Traction Force Microscopy

3.3.1. Time Lapse Imaging

Upright Setup

An upright microscope (Eclipse Ni, Nikon, Japan) inside a microscope incubator (Okolab, Italy) was used to acquire time lapse images. To assure close to physiological conditions the temperature was set to $37°C$, the CO_2 to 5% and humidity to 95% 3 hours prior to imaging to achieve equilibrated conditions. A precentered fiber illuminator (intensilight C-HGFI, Nikon, Japan) was used as a light source. Image acquisition was achieved using a high sensitivity camera (iXON3, Andor Technology Ltd, UK), a 60X water immersion objective (N.A.:1, Nikon, Japan) and NIS-Elements software (Nikon, Japan).

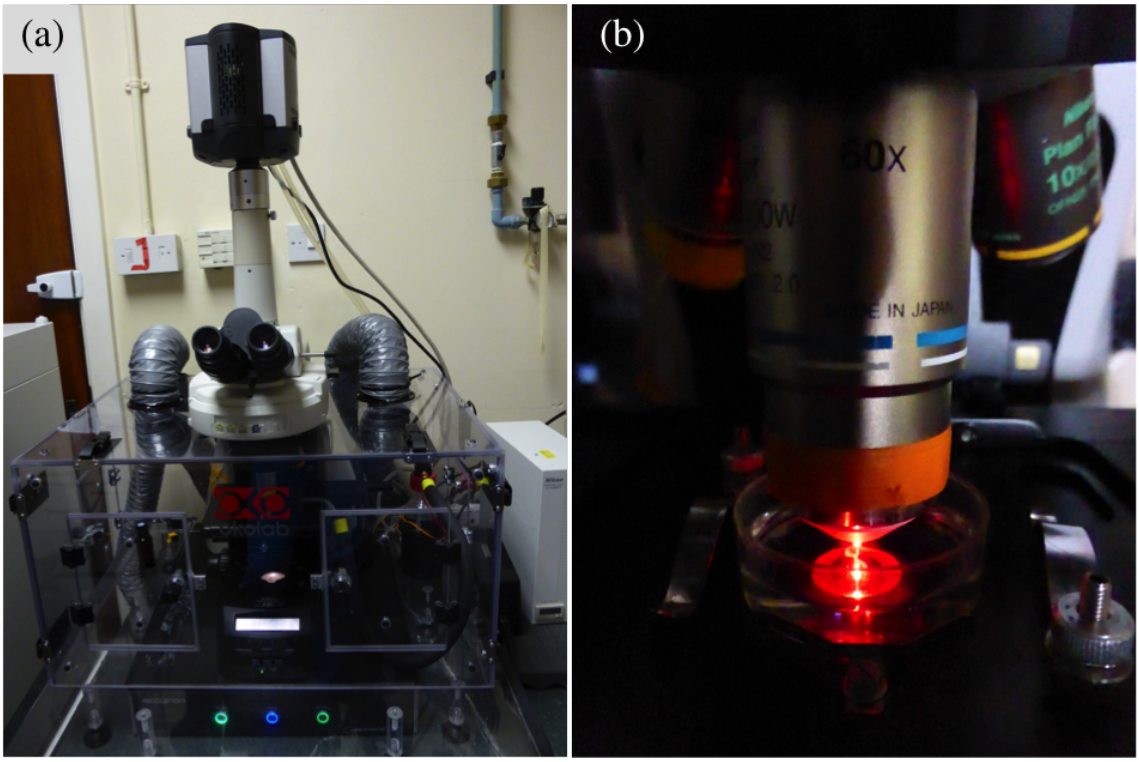

Figure 3.1.: Panel (a) shows the upright setup as it was used for time lapse imaging. The upright microscope is embedded in a microscope incubator that assures close to physiological conditions. Panel (b) displays an imaging dish with PAA gel and microglial cells during imaging.

The imaging dish with gel, adhered cells and sufficient culture medium was placed under the microscope. Initially, continuous imaging of the fluorescent beads (excitation wavelength: 625 nm, emission wavelength: 645 nm) was executed to automatically focus the

image. In order to find the right focus, the motorized stage covered a range of 2 μm in steps of 0.5 μm. This procedure was repeated for every 10 time-steps. Two images, a fluorescent image of beads and a bright field image of cells was acquired every 30 seconds (see Figure 3.2) for the duration of the experiment (45 min to 3 hrs).

When all images had been taken, Trypsin (Gibco, Life Technologies, UK) was added to the culture medium to break down the bonds between cells and the gel. A reference image with fluorescent beads at the 'relaxed' state was taken after approximately 10 minutes.

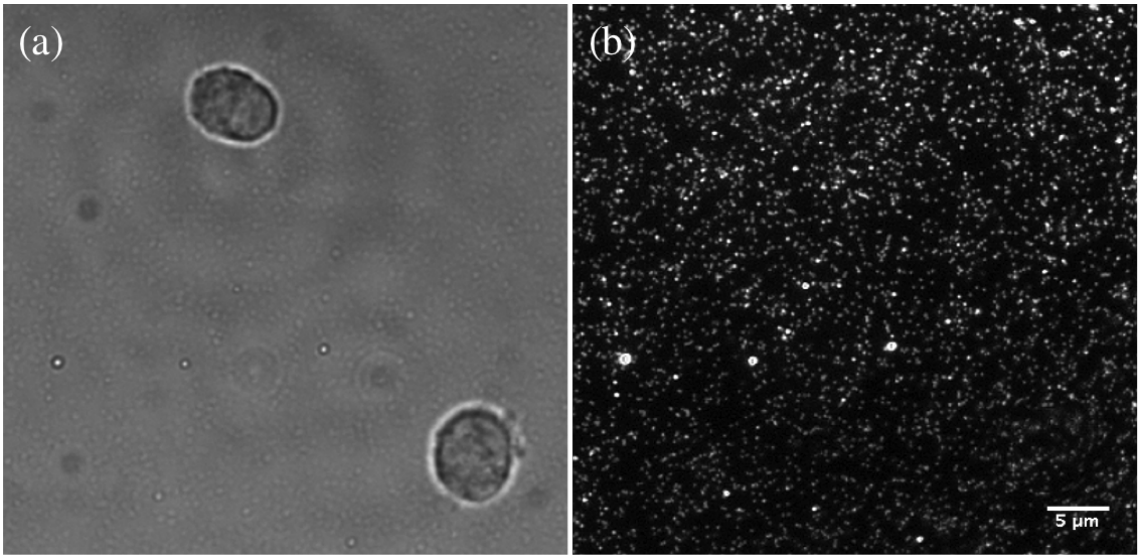

Figure 3.2.: In panel (a) a bright field image of 4 microglial cells on a PAA gel with G' = 300 Pa is displayed. Panel (b) shows an image of fluorescent beads of the same region.

Inverted Setup

The inverted setup consisted of a Zeiss Axio inverted microscope (Zeiss, Germany), a high sensitivity camera (iXON3, Andor Technology Ltd, UK), a HXP 200C illuminator (Zeiss, Germany) and 40X water immersion objective (N.A.:1.1, Zeiss, Germany). A JPK petri dish heater was used to heat the sample to approximately 37$^{\circ}C$. Images were acquired using the software ANDOR Solis (Andor Technology Ltd, UK). For the inverted setup, a bright field image of cells and a fluorescence image of beads was taken every 30 seconds. The focus was manually adjusted after 10 min. At the same time, the medium containing the cells was complemented by a lipopolysaccharide (LPS, Gibco, Life Technologies, UK) solution resulting in a final concentration of 1-2 μg/ml. LPS is a molecule that is found in the membrane of bacteria and therefore simulates bacterial contamination. The duration of the time lapse imaging was limited to approximately 20 min due to the change in CO_2 concentration in the medium.

3.3.2. Pre-processing

In order to automate the pre-processing of time lapse images, a macro in ImageJ (NIH, USA) was written. The macro finds and processes the reference images and .nd2 output files of the NIS-Elements software within a manually selected folder. The generated output can directly be used as an input for the script that calculates the traction forces.

The macro enhances the contrast of images, aligns them and saves the resulting files to the appropriate *bead* and a *cell* folders. In addition, the reference image is aligned with all bead images and saved to a separate folder. A detailed overview of steps is shown in figure 3.3. The macro is given in APPENDIX C.

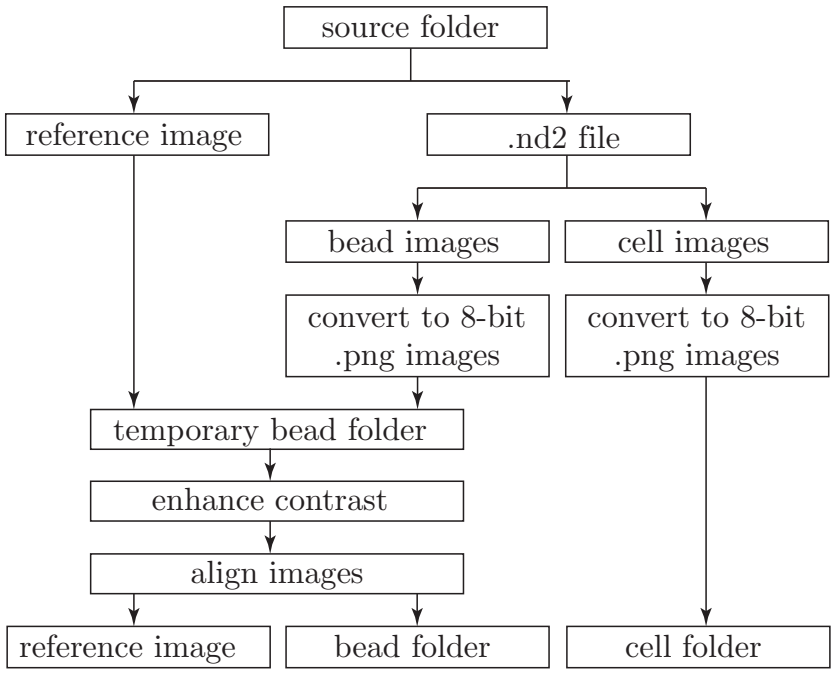

Figure 3.3.: Illustration of steps to automatically process .nd2 files to compute input folders for the traction stress calculations.

3.3.3. Traction Stress Calculation

Traction forces are indirectly measured by observing the deformation of the cell's substrate. For traction force microscopy (TFM), an elastic gel with embedded fluorescent beads is coated with molecules that facilitate the adhesion of cells. Once cells adhere to the substrate, they exert forces which deform the gel. The deformation is quantified by observing the displacement of fluorescent beads.

For the calculation of traction stresses a modified version of the code by Koch et al. was used in MATLAB (MathWorks Inc., MA, USA) [100]. The code is based on the method of Sabass et al. and Betz et al. [101, 102].

An overview of steps involved is displayed in Figure 3.4. First, the first bright field

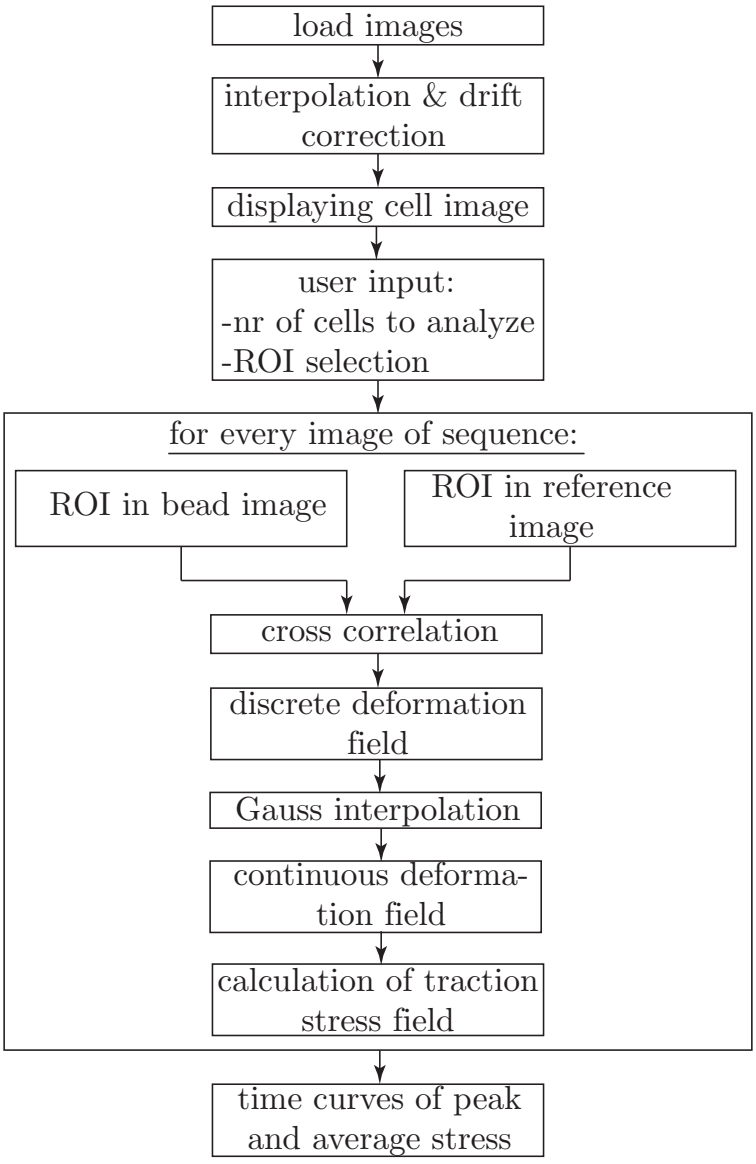

Figure 3.4.: Flowchart illustrating the steps involved in the calculation of traction stresses.

image of the image sequence is displayed for the user to define the number of cells to be analyzed. The region of interest (ROI) for each cell is manually updated for every n-th image, which allows moving cells to be analyzed. Hereafter, the corresponding ROI is selected in both the reference and the current bead image. The reference image defines the

'relaxed' state of beads after the infusion of Trypsin. Both ROIs are used to calculate the discrete deformation field through a cross-correlation algorithm.

The 2D cross-correlation coefficient r can be computed using the following equation (see MATLAB documentation):

$$r = \frac{\sum_m \sum_n (A_{mn} - \bar{A})(B_{mn} - \bar{B})}{\sqrt{(\sum_m \sum_n (A_{mn} - \bar{A})^2)(\sum_m \sum_n (B_{mn} - \bar{B})^2)}} \tag{3.1}$$

Where A and B are subsets of the ROIs and represent the template mask and search mask, respectively. $\bar{A}$ and $\bar{B}$ are the corresponding mean values of the masks and n an m are the matrix indices. The search mask A is shifted with respect to the template mask B to find the position with the maximum correlation. This procedure is repeated with different subsets of the ROIs to cover the entire area. The continuous deformation field is obtained by applying Gauss interpolation to the resulting discrete deformation field.

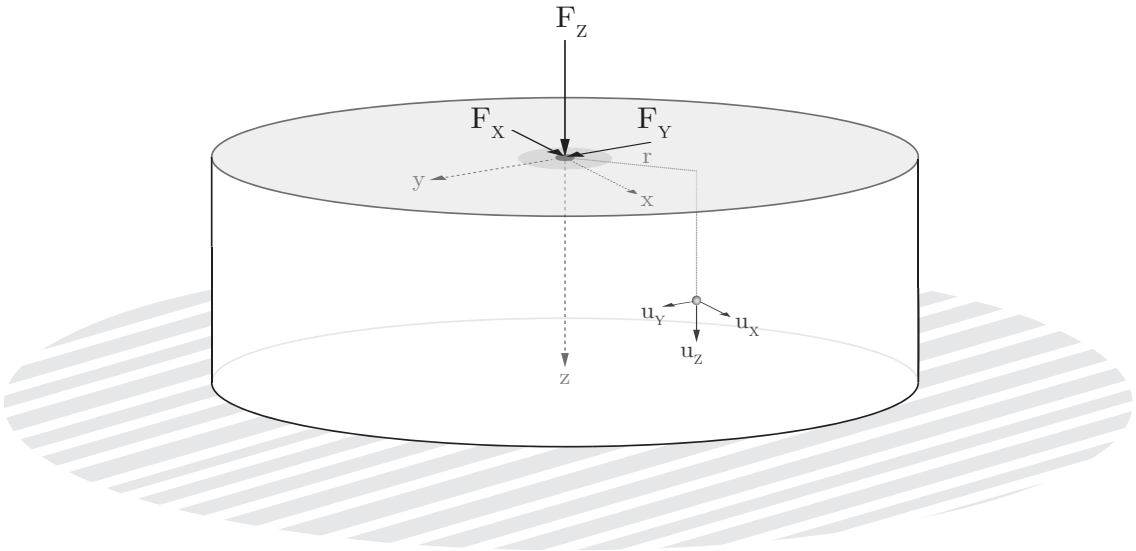

Figure 3.5.: Schematic drawing of an elastic half space. A point load composed of F_x, F_y and F_z is applied on the surface. The resulting displacements u_x, u_y and u_z of an arbitrary point inside the elastic substrate can be calculated using the Boussinesq solution.

The deformation of an elastic half space due to a point-like force can be described by the Boussinesq solution (see [103]. A schematic drawing of an elastic half space is illustrated in figure 3.5. If the beads are distributed closely to the surface, z can be taken to be 0. In this case, the displacements of one point u_x and u_y due to a point load on the surface can be computed:

$$u_x = \frac{1+\nu}{2\pi E} \cdot \frac{1}{r}\left(- \frac{(1-2\nu)x}{r} F_z + 2(1-\nu)F_x + \frac{2\nu x}{r^2}(xF_x + yF_y)\right) \tag{3.2}$$

$$u_y = \frac{1+\nu}{2\pi E} \cdot \frac{1}{r}\left(-\frac{(1-2\nu)y}{r}F_z + 2(1-\nu)F_y + \frac{2\nu y}{r^2}(xF_x + yF_y)\right) \tag{3.3}$$

In the equations above, ν is the Poisson ratio, E the Young's modulus of the substrate and $r = \sqrt{x^2+y^2})$ the in-plane distance between applied load and observed point. F_x, F_y and F_z are the force components in x-, y- and z-direction, respectively. The parameters x and y define the position of the observed point at the surface relative to the applied force. In matrix notation we obtain:

$$\begin{pmatrix} u_x \\ u_y \end{pmatrix} = \frac{1+\nu}{\pi E r^3} \begin{pmatrix} (1-\nu)r^2 + \nu x^2 & \nu xy \\ \nu xy & (1-\nu)r^2 + \nu y^2 \end{pmatrix} \begin{pmatrix} F_x \\ F_y \end{pmatrix} \tag{3.4}$$

The conversion between the Young's modulus E and the shear modulus G' of the substrates is computed using the Poisson's ratio ν and the following relation:

$$E = G' \cdot (2(1+\nu)) \tag{3.5}$$

The method of Green's function is used to decompose the force field exerted by the cell into a set of point-like forces (assuming an elastic medium). To obtain the resulting displacements for a superposition of forces, a convolution with the Boussinesq Green function is performed. Therefore, the forward problem can be described as:

$$\boldsymbol{u} = \boldsymbol{K} \otimes \boldsymbol{F} \tag{3.6}$$

The convolution kernel $\boldsymbol{K}$ is equivalent to the Boussinesq solution in equation 3.4. The displacement field is given by $\boldsymbol{u}$, the force field by $\boldsymbol{F}$. In order to determine the forces that induce the displacement of beads, the inverse problem has to be solved. Since a convolution becomes a simple multiplication in the Fourier space, Fourier transformation is applied to the entire system. The Fourier transform of the convolution kernel is calculated as in Butler et al. [104]:

$$\tilde{\boldsymbol{K}} = \frac{1+\nu}{\pi E k^3} \begin{pmatrix} (1-\nu)k^2 + \nu k_y^2 & \nu k_x k_y \\ \nu k_x k_y & (1-\nu)k^2 + \nu k_x^2 \end{pmatrix} \tag{3.7}$$

The inverse of $\tilde{\boldsymbol{K}}$ can be easily calculated in the Fourier space. Rearranging the transformed equation 3.4 results in the solution for the forces in the Fourier space:

$$\tilde{\boldsymbol{F}} = \tilde{\boldsymbol{K}}^{-1} \cdot \tilde{\boldsymbol{u}} \tag{3.8}$$

The MATLAB code calculates the solutions for $\tilde{\boldsymbol{F}}_{\boldsymbol{y}}$ and $\tilde{\boldsymbol{F}}_{\boldsymbol{x}}$ separately, back-transforms the solutions, and combines them to the force field $\boldsymbol{F}$ in polar coordinates. The stresses are obtained by dividing the force at each pixel by the area of the pixel. An exemplary representation of a traction stress map is displayed in Figure 3.6.

The peak traction stress is defined by the largest value of the traction stress map. The average stress is computed as the mean of all stress values of the ROI that are greater than a threshold value. The threshold value is a function of the noise level and the current peak value [100].

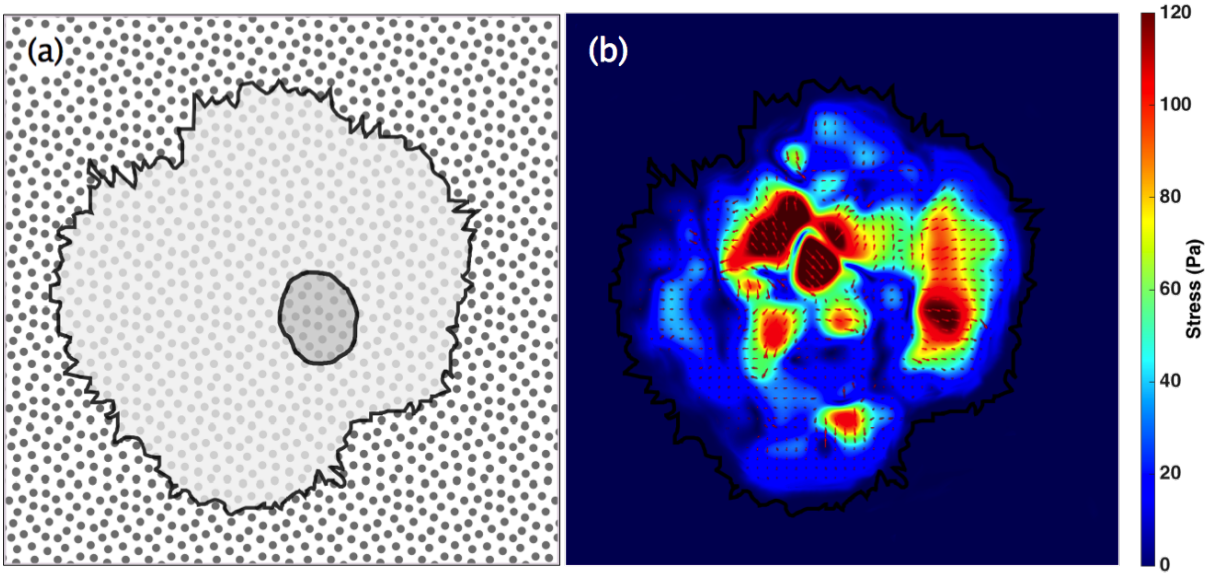

Figure 3.6.: Panel (a) shows a schematic drawing of an arbitrary cell shape on a PAA gel with fluorescent beads. In the right panel (b) a traction stress map is displayed. Traction stresses are obtained by analyzing the displacement of fluorescent beads using a 2D-cross-correlation algorithm.

3.4. Cell size and motion ratio

The cell size and the motion ratio were determined from bright field images using a MATLAB (MathWorks Inc., MA, USA) script (see APPENDIX D.3.). The code was adapted from the section "Detecting a Cell Using Image Segmentation" of the MATLAB documentation.

In essence, the cells are segmented from the background by calculating the gradient representation of the bright field image and by applying threshold filtering to detect the cell edges. Missing components of the cell outline are then complemented and the area within the outline filled. The resulting smoothed binary image is shown in panel (b) of Figure 3.7. Individual objects are then labelled. Objects can represent single cells or accumulations of cells. Therefore, only single cell objects (indicated by red arrows) are selected to calculate the cell size. The area of the selected object A_{object} is computed according to the following equation:

$$A_{object} = n_{pixel,object} \cdot A_{pixel} \tag{3.9}$$

where $n_{pixel,object}$ describes the number of pixels of the object and A_{pixel} the area per pixel.

For the motion ratio, the cell area and cell location are determined for each time step. The superposition of all binary images of the time series is displayed in panel (c) of Figure 3.7. In this case, objects represent areas that were covered by single cells or accumulations of cells during the course of the experiment. Again, only single cells that are present in the first image (b) and the superimposed image (c) are selected (see red arrows). The motion ratio R_{motion} is calculated by dividing the initial cell size $A_{initial}$ by the area explored by the cell during the course of the experiment A_{sum}:

$$R_{motion} = \frac{A_{sum}}{A_{initial}} \tag{3.10}$$

If the value for R_{motion} is equal to one, the cell does not move, but may undergo changes in shape. An increasing R_{motion} value indicates that a larger area is explored by the cell during the experiment.

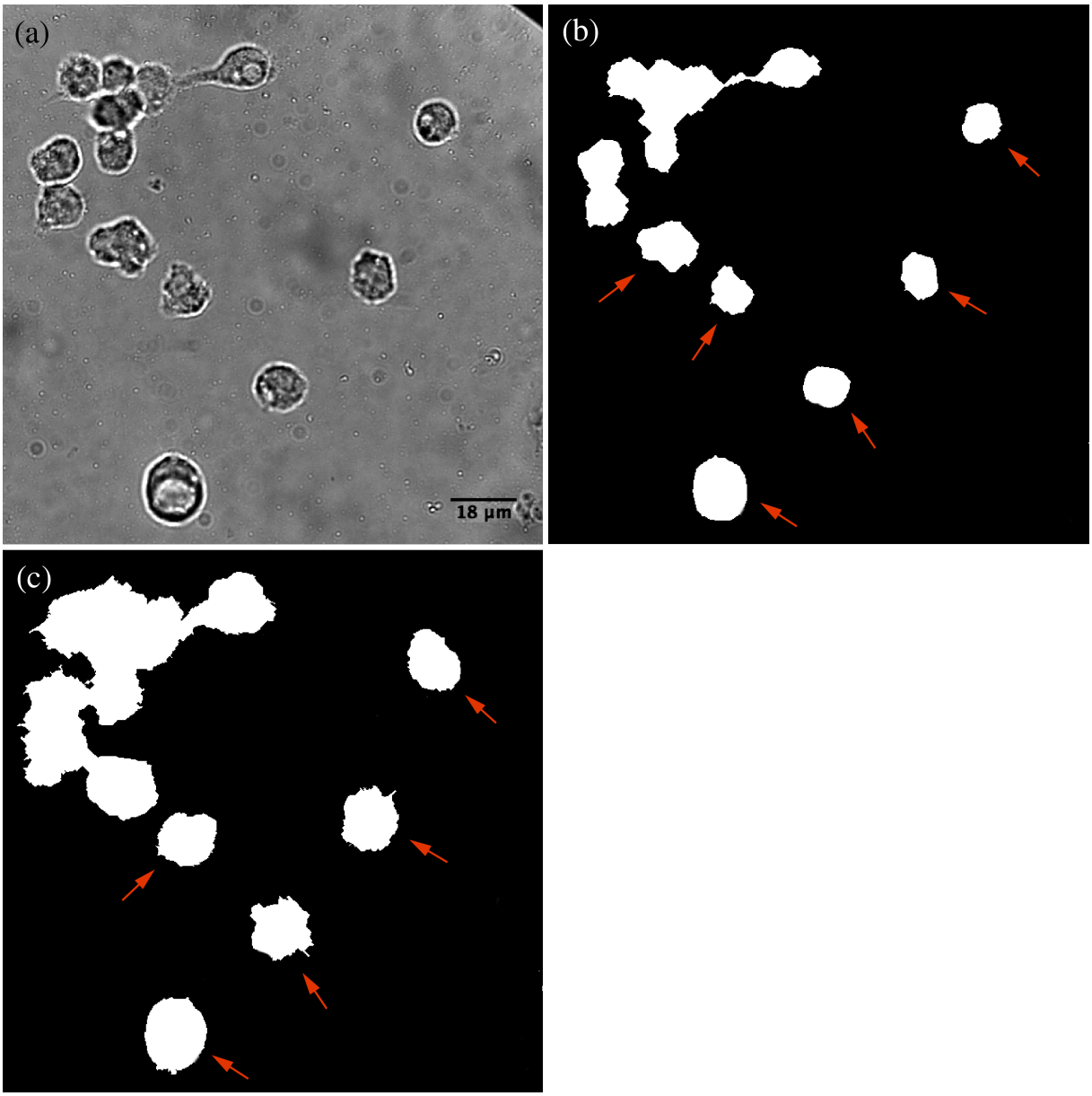

Figure 3.7.: Schematic of steps to compute cell size and motion ratio. In panel (a) a representative bright field image of microglial cells on a PAA gel with G' = 100 Pa is displayed. A gradient representation of the bright field image is computed and threshold filtering applied to detect the cell edges. The cell outline is then filled. The resulting binary image is displayed in panel (b). White areas represent single cells or cell accumulations. To calculate the size of a single cells $A_{initial}$, only objects representing single cells are selected (pointed out by red arrows). The area covered by a single cell during the experiment A_{sum} is computed by projecting the binary images for all time steps. The resulting superimposed binary image is displayed in panel (c). Only objects corresponding to single cells in (b) and (c) are selected as indicated by red arrows. The motion ratio is calculated by dividing $A_{initial}$ by A_{sum} for individual cells.

3.5. Staining

Prior to staining, the cells were fixed by placing them in a 4% paraformaldehyde (PFA) + 96% PBS solution for approximately 20 minutes. PFA promotes the cross-linking of amino acids. The cells were then covered with a 0.1% triton solution to permeabilize the cell membrane. To remove remaining triton and PFA, the cells were washed 3-4 times with 100% PBS.

3.5.1. Actin & Nucleus Staining

In order to stain the cells for F-actin, a solution of 2 Units (equivalent of $10\mu L$) of Alexa-488-phalloidin (Life Technologies, UK) per 300 μL distilled water (dH_20) was applied for one hour. The nuclei were stained using DAPI (Sigma-Aldrich Co, UK). The cover slips with gels and stained cells were then mounted onto imaging slides using Fluoromount G (SouthernBiotech, USA).

3.5.2. Microglia identification

To quantify the ratio of microglia in the used cell cultures, a representative cell culture on a cover slip was stained using OX42. OX42 specifically reacts with microglial cells and macrophages.
The primary antibody OX42 was diluted 1:200 in 100% PBS and added to the fixed cell culture overnight. After 3 washes with PBS, the secondary goat anti-mouse antibody (1:500 in 100% PBS) was applied for 1 hour. The secondary antibody was labeled with Alexa Fluor 488 (Life Technologies, UK). In addition, the nuclei were stained using DAPI (Sigma-Aldrich Co, UK).
The cover slip was then mounted onto an imaging slide using Fluoromount G (Southern-Biotech, USA).

3.6. Fluorescence imaging

For fluorescence imaging an upright microscope (Eclipse Ni, Nikon, Japan) with a pre-centered fiber illuminator (intensilight C-HGFI, Nikon, Japan) was used. Images were acquired using a high sensitivity camera (iXON3, Andor Technology Ltd, UK), a 60X water immersion objective (N.A.: 1), a 20X water immersion objective (N.A.: 0.5), a 10X objective (N.A.: 0.3, all Nikon, Japan) and NIS-Elements software (Nikon, Japan).

4. Results

4.1. Microglia ratio

The method used to obtain microglial cell cultures separates mainly microglial cells from mixed glia cultures. However, a pure microglia culture is unlikely to be obtained. In order to determine the microglia ratio within the cultures used, I stained microglial cells with OX42 (Figure 4.1(a)). The cells were cultured on glass and OX42 positive and OX42 negative cells were counted (Figure 4.1(b)). The fraction of microglia in the analyzed cell culture was found to be 95.5%.

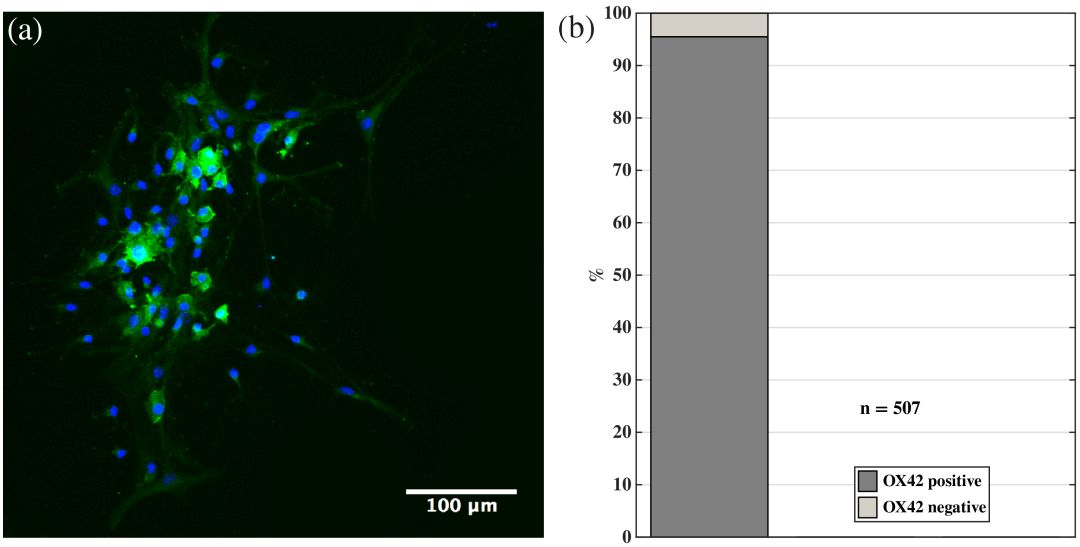

Figure 4.1.: Panel (a) shows representative microglial cells on glass that were labeled with OX42 (green). The nuclei were stained using Dapi and appear in blue. A bar graph showing the fraction of microglial cells (OX42 positive) is displayed in panel (b). According to the number of OX42 positive cells, the analyzed cell culture consisted of 95.5% microglia.

4.2. Traction Stress

4.2.1. Inverted Setup: Microglia

Measuring traction stresses contributes to a better understanding of the mechanosensitivity of microglial cells. It has been shown that other cell types adapt their traction forces to substrate stiffness. To investigate substrate stiffness-dependent deformations and traction stresses of microglia, I performed two independent traction force experiments on five substrates of varying stiffness (G' = 100 Pa, 300 Pa, 1 kPa, 2 kPa, 10 kPa).

The peak deformations of the ROI that are computed by the 2D cross-correlation algorithm increased with stiffness until they declined significantly for a substrate with G' = 2 kPa (Figure 4.2). Applying the Kruskal-Wallis test resulted in a p-value of 1.017e-06. This indicates that the values of peak deformations for different stiffness values are statistically different considering a significance level of α = 0.1.

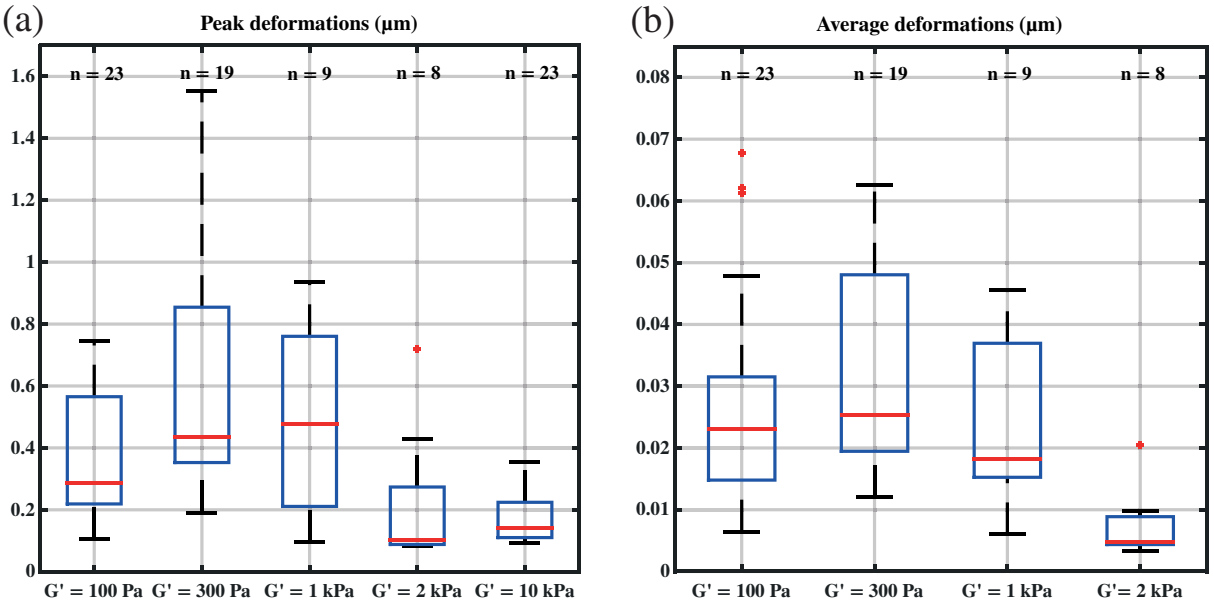

Figure 4.2.: Box plots showing peak (a) and average (b) deformations of the ROI as computed by the 2D cross-correlation algorithm. Values for substrates with varying stiffness (G' = 100 Pa to G' = 10 kPa) are displayed. The number of analyzed cells per substrate is defined by n. Two independent experiments were performed. The median of peak deformations increased with stiffness until it drastically decreased for a substrate with G' = 2 kPa. Average deformations were one order of magnitude smaller then the detected peak deformations. The highest median value for average deformations was found for a substrate with G' = 300 Pa.

Since the smallest detectable displacement of fluorescent beads is limited to approximately 200 nm, the substrate with G' = 2 kPa was set as the upper limit for further analysis. Values for a shear modulus of 10 kPa were neglected.

The average deformations were one order of magnitude smaller than the peak deformations (Figure 4.2). The highest average deformations were found for a substrate with G' = 300 Pa. A significant decline of average deformations was observed for the stiffest gel (G' = 2 kPa). The Kruskal-Wallis test showed that the values for different substrate stiffness are statistically different (p-value = 4.822e-07).

Average and traction stress of microglia showed changes in time as outlined in Figure 4.3. Peak traction stress increased with stiffness (Figure 4.4). For a shear modulus of 2

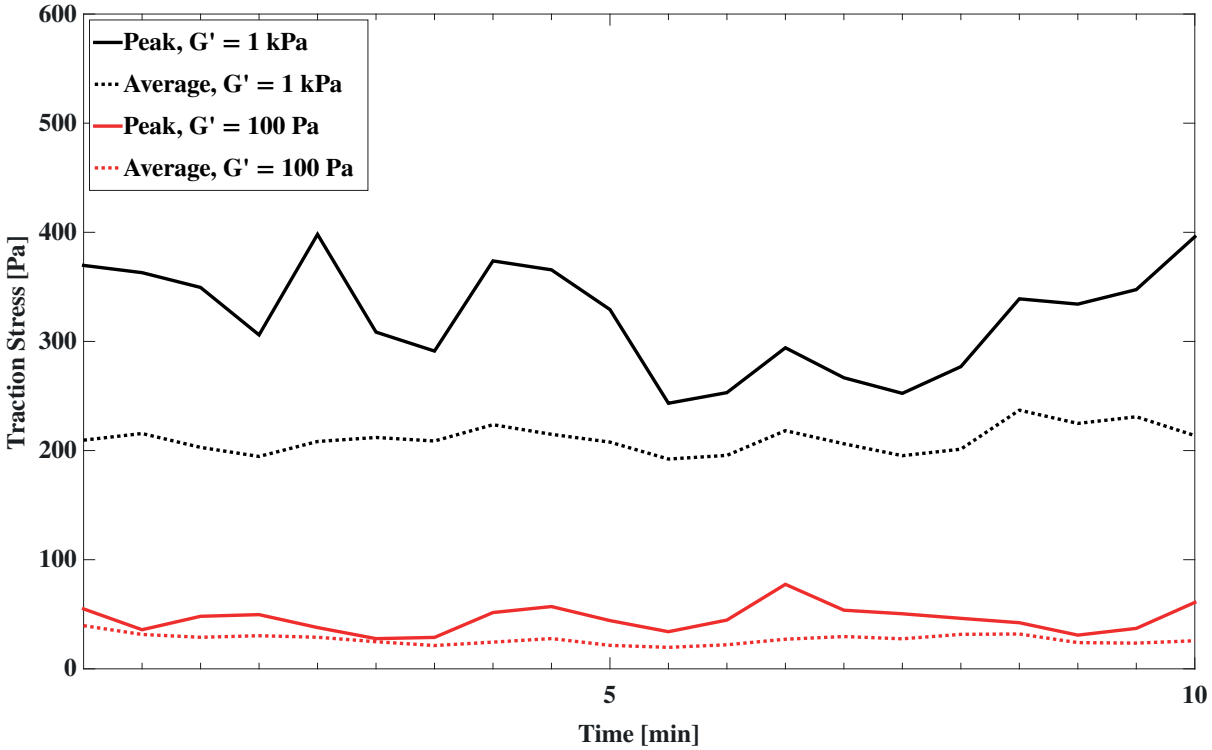

Figure 4.3.: Average and peak traction stress for two representative cells on gels of G' = 100 Pa and G' = 1 kPa for a duration of 10 minutes. Variations with time were apparent for all stresses and stiffness values.

kPa, the peak stress decreased significantly. The highest peak stress values were found for a substrate with G' = 1 kPa. The Kruskal-Wallis test indicated the statistical difference between the values for different substrate stiffness (p-value = 1.867e-14).

The highest average traction stresses were found for a substrate with G' = 1 kPa (see Figure 4.4). The average traction stresses for the softest substrate (G' = 100 Pa) were relatively small compared to the other substrates. The statistical difference was confirmed using the Kruskal-Wallis test (p-value = 2.755e-12).

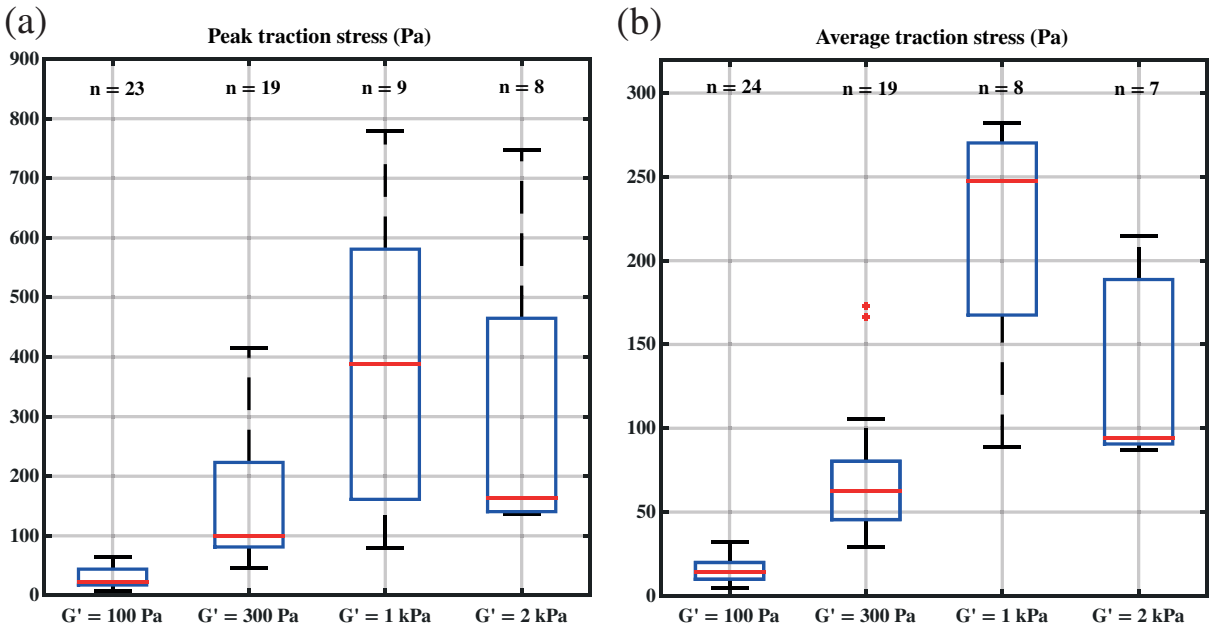

Figure 4.4.: A box plot representing peak traction stress for 4 substrates of different stiffness is displayed in panel (a). The number of cells is defined by n. Two independent experiments were performed. The peak traction stress increased with substrate stiffness. For a substrate with G' = 2 kPa the peak traction stress declined. Panel (b) displays a box plot of average traction stress. The highest values were found for a substrate with G' = 1 kPa. This value corresponds to the shear modulus of brain tissue, and to the 'tactile set-point' described in Moshayedi et al. at which glial cells transition from a 'soft' to a 'stiff' phenotype [18].

4.2.2. Influence of LPS

Microglia can undergo a transformation from a 'resting' to an 'activated' state. The activated phenotype is very motile and plays an important role in the immune response of the central nervous system. In order to observe the influence of microglia activation through LPS on substrate deformations and traction stresses, I performed two independent traction force experiments with 1-2 μg/ml LPS.

The peak deformations seemed to be higher for the LPS measurements on the softest substrate (G' = 100 Pa in Figure 4.5). Statistical significance was not found though (one-sided Mann-Whitney U test: p-value = 0.1711). For the other two substrates (G' = 300 Pa and G' = 1 kPa), peak deformation values appeared to be smaller for the LPS measurements (p-value = 0.1011 and p = 0.1383, respectively).

In the case of average deformations, the influence of LPS seemed to decrease the values for all substrates. The one-sided Mann-Whitney U test revealed statistical significance for the substrates with G' = 100 Pa and G' = 300 Pa (p-value = 0.03993 and p-value = 0.04469, respectively). The p-value for G' = 1 kPa was found to be 0.1179.

Considering a significance level of α = 0.1, the average deformations decreased with LPS for substrates with G' = 100 Pa and G' = 300 Pa.

Taking all results for the deformations into account, LPS had a more significant influence on the average deformations than on the peak deformations.

The effect of 1-2 μg/ml LPS on the traction stresses changed with substrate stiffness (Figure 4.6). For the softest substrate (G' = 100 Pa), the peak traction stress seemed to be slightly higher when LPS was present. The one-sided Mann-Whitney U test revealed that this difference was not statistically significant (p-value = 0.1326). For the two stiffer gels (G' = 300 Pa and G' = 1 kPa), the opposite effect was found: the peak traction stress seemed to decrease in the presence of LPS (p = 0.09506 and p = 0.1606, respectively).

On the soft substrate, the average traction stress seemed to be slightly higher with LPS. The one-sided Mann-Whitey U test revealed that this difference was not statistically significant (p-value = 0.2412). For a substrate with G' = 300 Pa, LPS caused the average traction stress to decrease (p-value = 0.08374). A similar trend was found for a the stiff gel (G' = 1 kPa) with a p-value of 0.09744.

Considering a significance level of α = 0.1 and only results for substrates with G' = 300 Pa, average and peak traction stress decreased with 1-2 μg/ml LPS as compared to the control measurements. In addition, the influence of LPS was more significant for the average traction stresses.

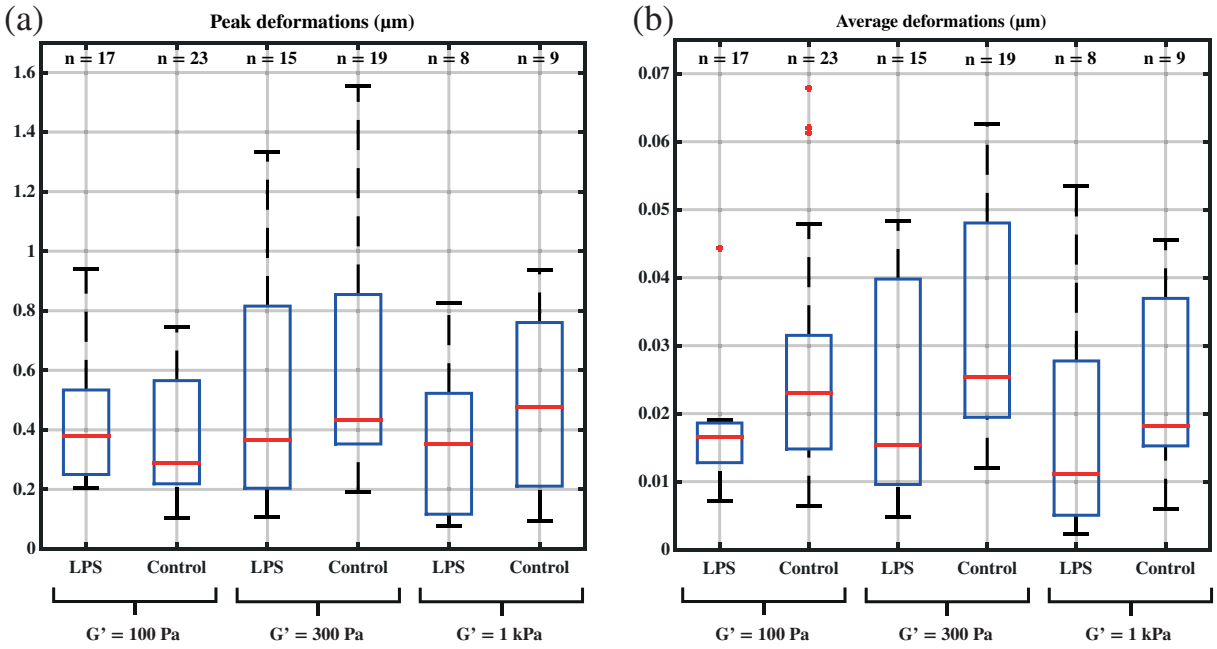

Figure 4.5.: Box plots showing peak (a) and average (b) deformations for cells in standard medium and cells in a medium with 1-2 μg/ml LPS. For a substrate with G' = 100 Pa, peak and average deformations were higher for cells with LPS. The opposite effect was seen for a substrate with G' = 300 Pa and G' = 1 kPa.

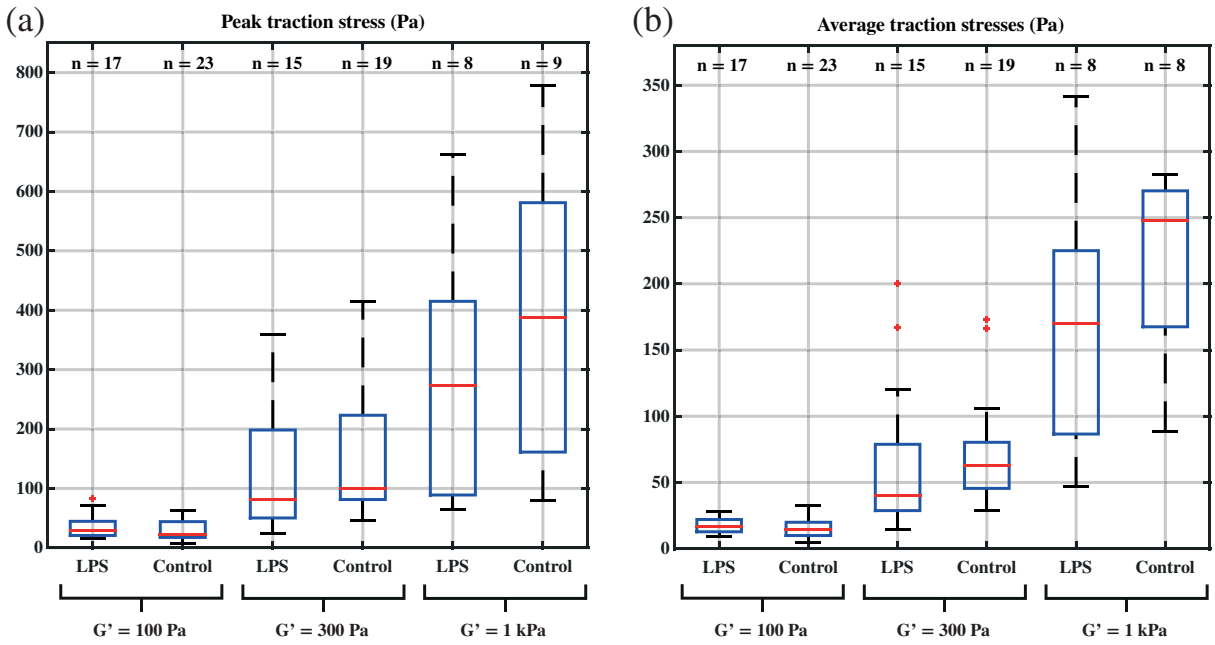

Figure 4.6.: Panel (a) shows a box plot of peak traction stress comparing cells in standard medium and cells in a medium with 1-2 μg/ml LPS. For substrates with G' = 100 Pa, peak traction stresses were higher with LPS. For substrates with G' = 300 Pa and G' = 1 kPa, LPS showed the opposite effect: the peak traction stress decreased. The same trend was observed for the average traction stress as displayed in panel (b).

4.2.3. Upright Setup: Microglia

In this section, results of the inverted setup are compared with results from an upright setup. I performed eight independent traction force experiments using the upright setup. With the same setup, I acquired traction force data of a cell on a very stiff gel.

Deformations of the ROI were higher for the upright setup independent of substrate stiffness (Figure 4.7). The peak deformation values that were calculated by the 2D cross-correlation algorithm for a cell on a very stiff substrate (G' on the order of 100 kPa) ranged between 0.5 and 1.5 μm (Figure 4.8).

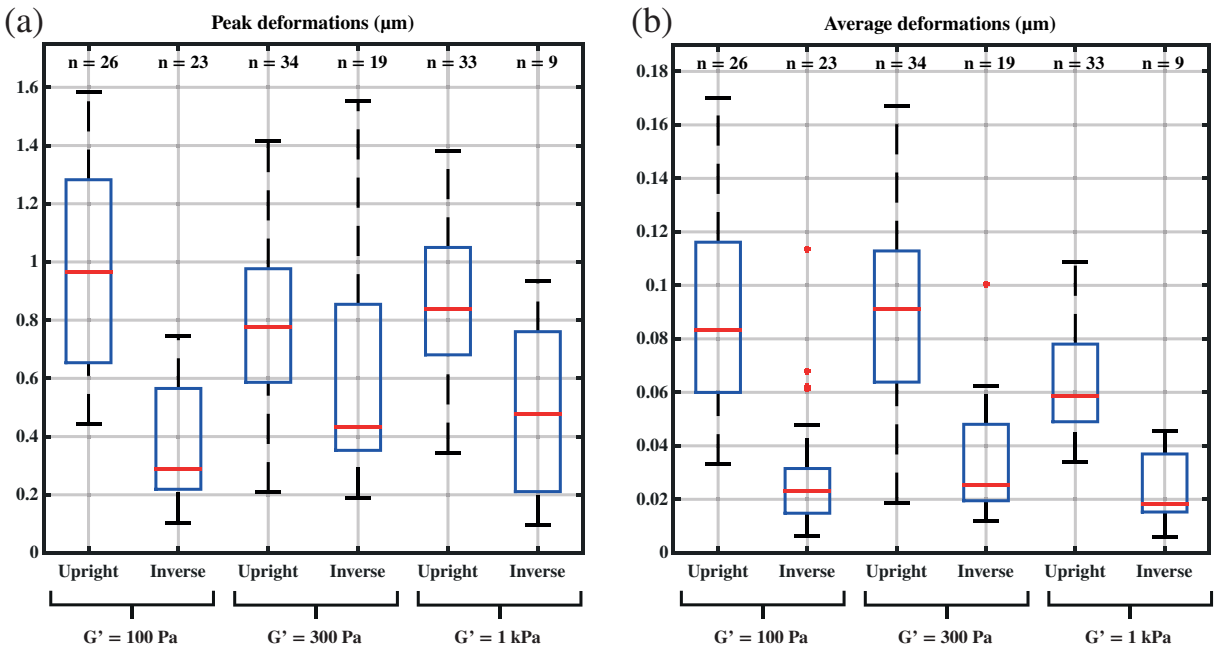

Figure 4.7.: Box plots showing peak (a) and average (b) deformations for the upright and the inverted setup for substrates of varying stiffness. Peak and average deformations were higher for the upright setup when compared to the values of the inverted setup.

Average and peak traction stress for substrates with G' = 100 Pa and G' = 1 kPa showed changes in time as displayed in Figure 4.9.

Average and peak traction stresses were higher for the upright setup for all values of substrate stiffness (Figure 4.10). The relative difference between the medians of peak stress for the two setups was found to be the largest for the soft substrate (73.3 $\%$) and decreased with substrate stiffness (Table 4.1).

The relative difference between the medians of average stress for the upright and the inverted setup was smaller than for the peak stresses and decreased with substrate stiffness (Table 4.2).

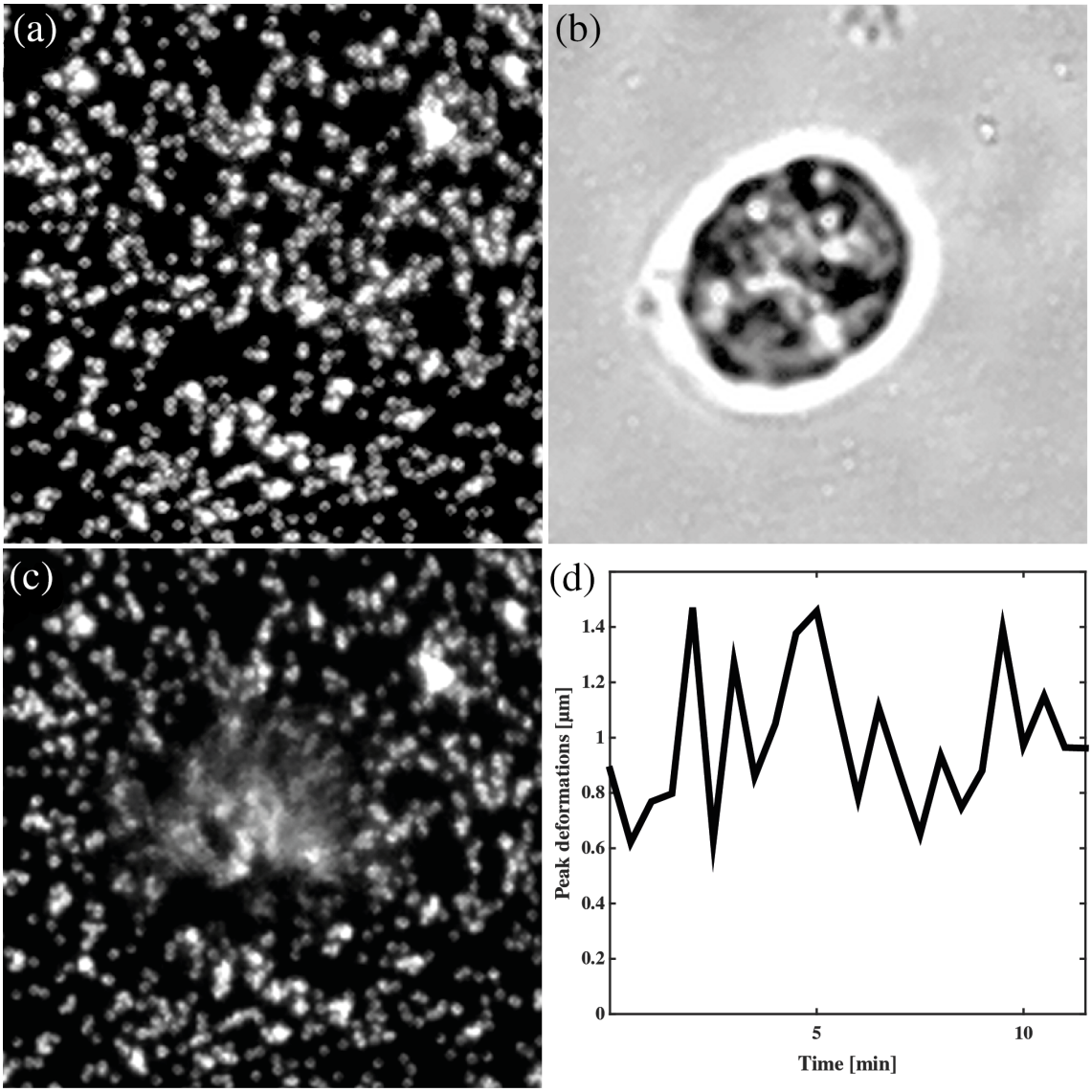

Figure 4.8.: Panel (a) shows fluorescent beads embedded in a PAA gel as seen using the upright setup. The shear modulus is on the order of G' = 100 kPa. The image was acquired when no cell was within the ROI. Panel (b) displays a bright field image of the same region after a microglial cell moved into the ROI. An image of fluorescent beads with the microglial cell within the ROI is displayed in panel (c). Smearing artefacts are visible. Panel (d) shows peak deformations of the ROI with the cell for a duration of 12 minutes as computed by the 2D cross-correlation algorithm. The image in panel (a) was used as the reference image for the deformation calculations.

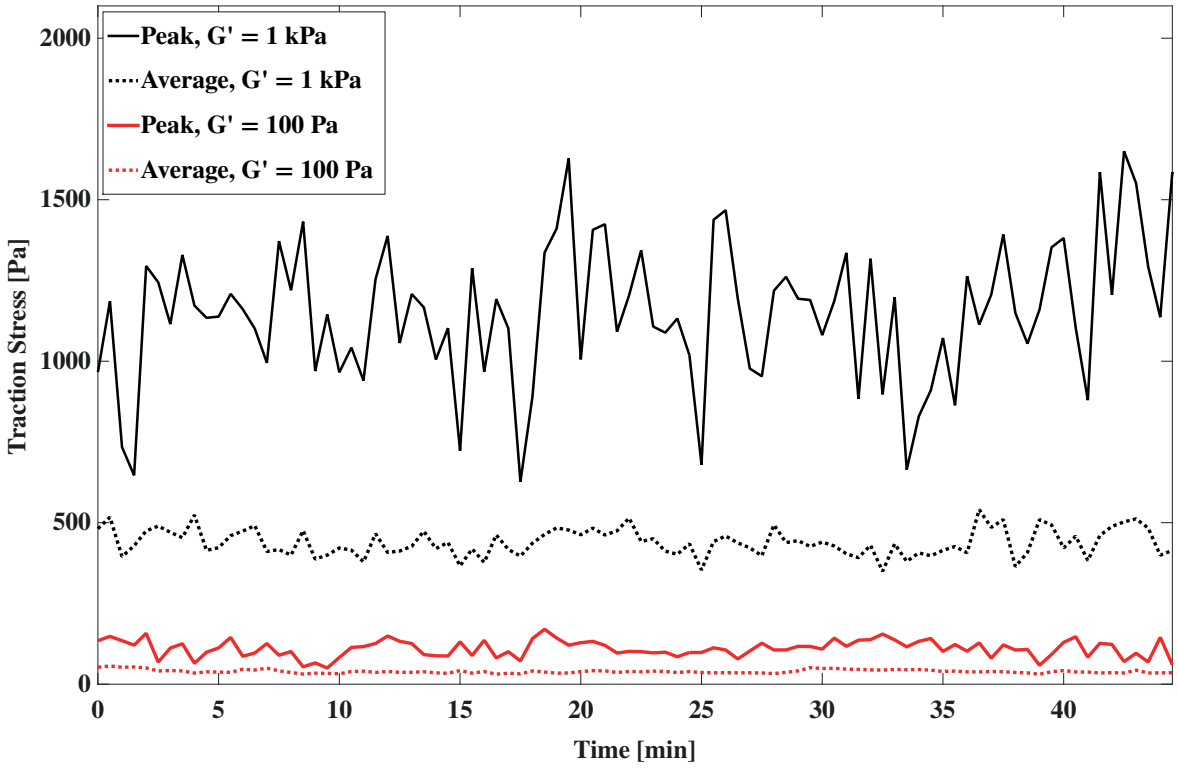

Figure 4.9.: Traction stress for two representative cells on PAA gels of different stiffness (G' = 100 Pa and G' = 1 kPa) are presented. The time curves for a duration of 45 minutes show a pulsatile characteristic for average and peak traction stress.

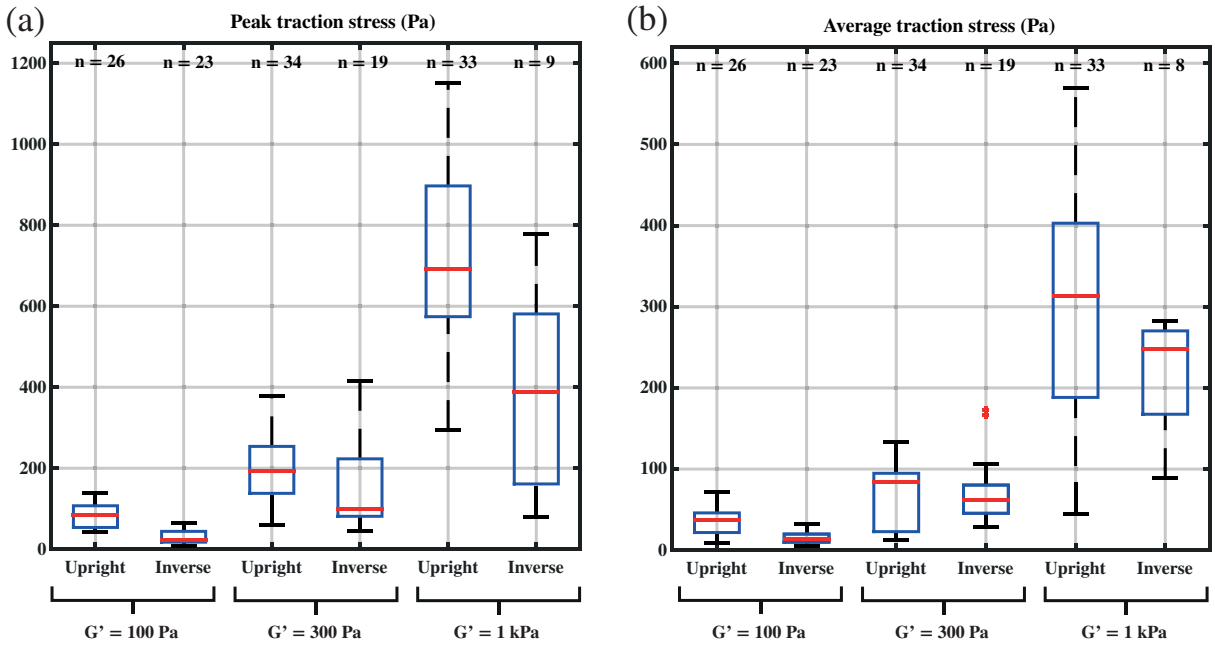

Figure 4.10.: Panel (a) shows a box plot with peak traction stress values for the inverse and the upright setup for cells on substrates of varying stiffness (G' = 100 Pa, G' = 300 Pa, G' = 1 kPa). The computed stress values were higher for the upright setup for all values of substrate stiffness. The same trend was observed for the average traction stress in panel (b).

Substrate stiffness (Shear modulus G')(Pa)	**Median of peak stress** (Pa)		**Relative difference** (%)
	Upright	Inverted	
100	84.7	22.6	73.3
300	192.5	100.0	48.0
1000	691.9	387.7	43.9

Table 4.1.: Median values of peak stress for upright and inverted setup for three different values of substrate stiffness (G' = 100 Pa, G' = 300 Pa and G' = 1 kPa). The relative difference was largest for the softest substrate and decreased with substrate stiffness.

Substrate stiffness (Shear modulus G')(Pa)	**Median of average stress** (Pa)		**Relative difference** ($\%$)
	Upright	Inverted	
100	37.3	14.3	61.7
300	84.6	62.5	26.1
1000	312.9	247.6	20.8

Table 4.2.: Median values of average stress for upright and inverted setup for three different values of substrate stiffness (G' = 100 Pa, G' = 300 Pa and G' = 1 kPa). The relative difference decreased with substrate stiffness.

4.2.4. Upright Setup: Glioblastoma cells

To improve the treatment of glioblastomas, scientists have become interested in targeting subpopulations of tumor cells with distinct characteristics. Traction force microscopy could be used to differentiate subgroups of glioblastoma cells. In addition, results could be used to find patterns that identify invasiveness and aggressiveness of those subgroups. I performed five independent traction force experiments with glioblastoma cells from spatially different tumor fractions.

For the softest substrate (G' = 100 Pa), glioblastoma cells from the tumor fraction T5 showed the highest peak traction stress (Figure 4.11). The Kruskal-Wallis test indicated that the values of the three tumor fractions were statistically different (p-value = 0.03673). The Cells from the tumor fraction T8 were found to show the highest peak traction stress for the two stiffer substrates (G' = 300 Pa and G' = 1000 Pa). The resulting p-values as calculated by the Kruskal-Wallis test were 0.01013 and 0.2295, respectively.

Considering a significance level of α = 0.1 and the substrates with G' = 100 Pa and G' = 300 Pa, the peak traction stresses differed between glioblastoma cells from the three tumor fractions.

The peak traction stress values obtained were on the order of the values for microglia for the upright setup.

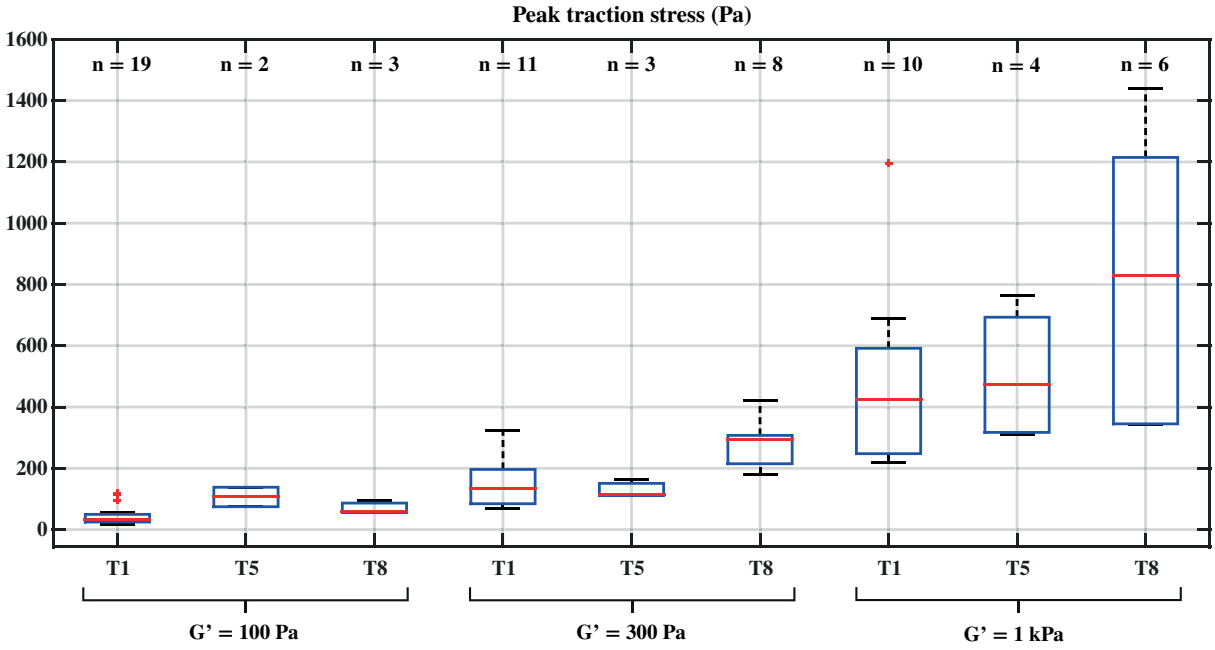

Figure 4.11.: Box plot showing peak stress for glioblastoma cells of three different tumor fractions T1, T5 and T8 on substrates of varying stiffness (G' = 100 Pa, G' = 300 Pa, G' = 1 kPa). On the softest substrate, cells from fraction T5 showed the highest peak stress. On the two stiffer gels, the peak stress was highest for cells from fraction T8.

For the softest substrate (G' = 100 Pa), cells from the tumor fraction T5 showed the highest average traction stress (Figure 4.12). Applying the Kruskal-Wallis test resulted in a p-value of 0.03137, indicating a statistically significant difference between the three fractions. For the other two substrates (G' = 300 Pa and G' = 1 kPa), the cells from tumor fraction T8 exerted the highest forces. The p-values as calculated by the Kruskal-Wallis test were 0.0008638 and 0.2655, respectively.

Considering a significance level of α = 0.1 and substrates with G' = 100 Pa and G' = 300 Pa, the average traction stresses differed between glioblastoma cells from the three tumor fractions.

The values for the average traction stress were on the order of the values for microglia for the upright setup.

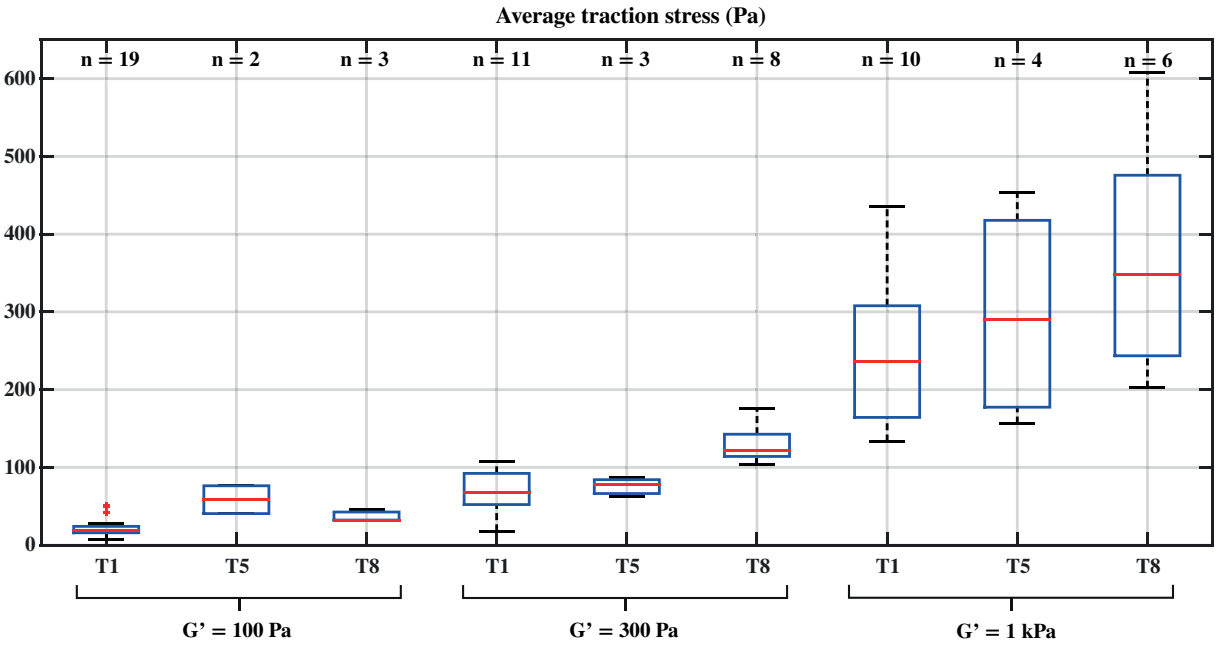

Figure 4.12.: Box plot showing average stress for glioblastoma cells of three different tumor fractions T1, T5 and T8 on substrates of varying stiffness (G' = 100 Pa, G' = 300 Pa, G' = 1 kPa). On the softest substrate, cells from from fraction T5 showed the highest average stress. On the two stiffer gels, the average stress was highest for cells from fraction T8.

4.3. Cell size and motion ratio

The influence of substrate stiffness on traction stresses was investigated in the previous sections. Cell size and cell motility are believed to be tightly coupled with the generation of cell traction forces. In order to contribute to a better understanding of the correlation, I determined the cell size on substrates with varying stiffness from bright field images. In addition, I calculated the substrate stiffness-dependent motion ratio.

4.3.1. Inverted setup: Microglia

For the inverted setup, the cell size of microglia as calculated from bright field images increased with substrate stiffness (see Figure 4.13). The median of the cell size was equal to 111.6 $(\mu m)^2$ for the softest substrate (G' = 100 Pa), 136.7 $(\mu m)^2$ for G' = 300 Pa and 163.0 $(\mu m)^2$ for the stiff substrate (G' = 1 kPa). Applying the Kruskal-Wallis test resulted in a p-value of 0.03305. Considering a significance level of α = 0.1, the cell size was significantly different for the three values of substrate stiffness.

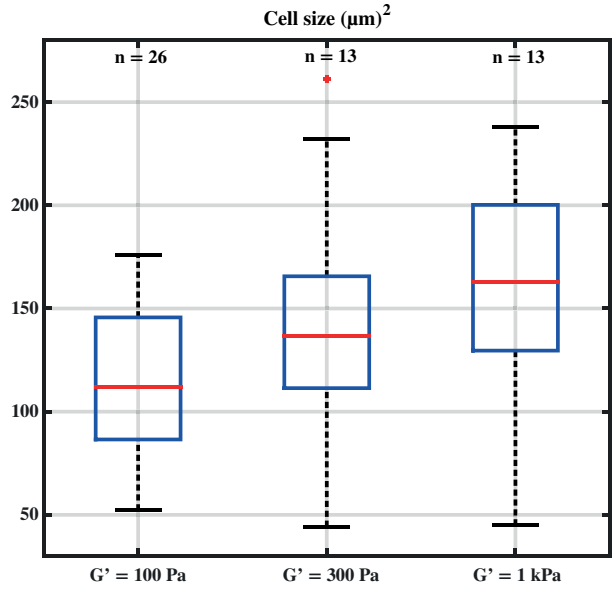

Figure 4.13.: Box plot showing microglial cell size on three substrates of different stiffness. The cell size was calculated from bright field images and increased with substrate stiffness.

4.3.2. Upright setup: Microglia

For the upright setup, the microglia cell size was largest for a substrate with G' = 300 Pa (see Figure 4.14). A decrease in cell size was found for a substrate with G' = 1 kPa. This finding differed significantly from the result of the inverted setup. The median of cell size was equal to 103.8 $(\mu m)^2$ for the soft substrate, 116.5 $(\mu m)^2$ for a substrate stiffness of G' = 300 Pa and 87.7 $(\mu m)^2$ for the stiff substrate (G' = 1 kPa). Statistical significance was found using the Kruskal-Wallis test (p-value = 0.001831).

The motion ratio was smallest for a shear modulus of 300 Pa with a median value of 1.54. The difference between different values of substrate stiffness was not statistically significant though (Kruskal-Wallis test, p-value = 0.1923)

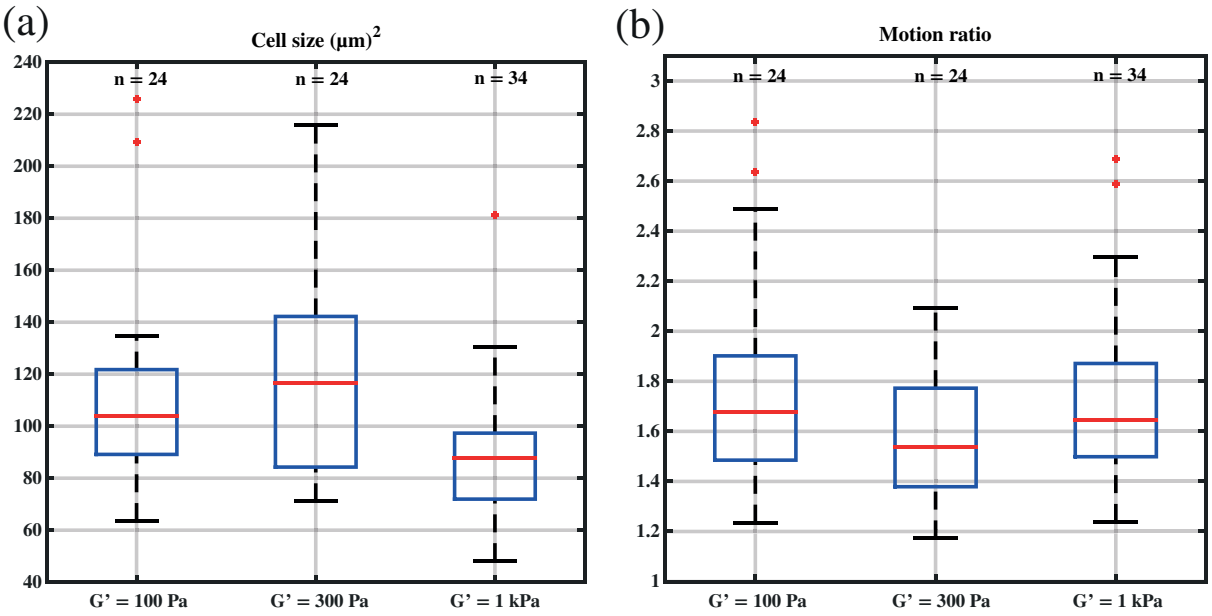

Figure 4.14.: Panel (a) shows a box plot with microglial cell size on substrates with varying stiffness. The cell size was highest for a shear modulus of 300 Pa and decreased significantly for a stiffness with G' = 1 kPa. A box plot showing the motion ratio of microglial cells for different substrate stiffness is depicted in panel (b). The lowest value was found for a substrate with G' = 300 Pa.

4.3.3. Upright setup: Glioblastoma

The median of glioblastoma cell size increased with substrate stiffness as displayed in panel (a) of Figure 4.15. For the softest substrate (G' = 100 Pa), I found a median value of 124.1 $(\mu m)^2$, for G' = 300 Pa a median value of 143.7 $(\mu m)^2$ and for the stiffest substrate (G' = 1 kPa) a median of 155.9 $(\mu m)^2$. Statistical significance was not found (Kruskal-Wallis test, p-value = 0.5278).

The motion ratio of glioblastoma cells was highest for a substrate with G' = 300 Pa (not statistically significant, Kruskal-Wallis test: p-value = 0.7137). The motion ratio for this substrate stiffness was significantly higher than for microglia on the same substrate (Mann-Whitney U test, p-value = 0.0199).

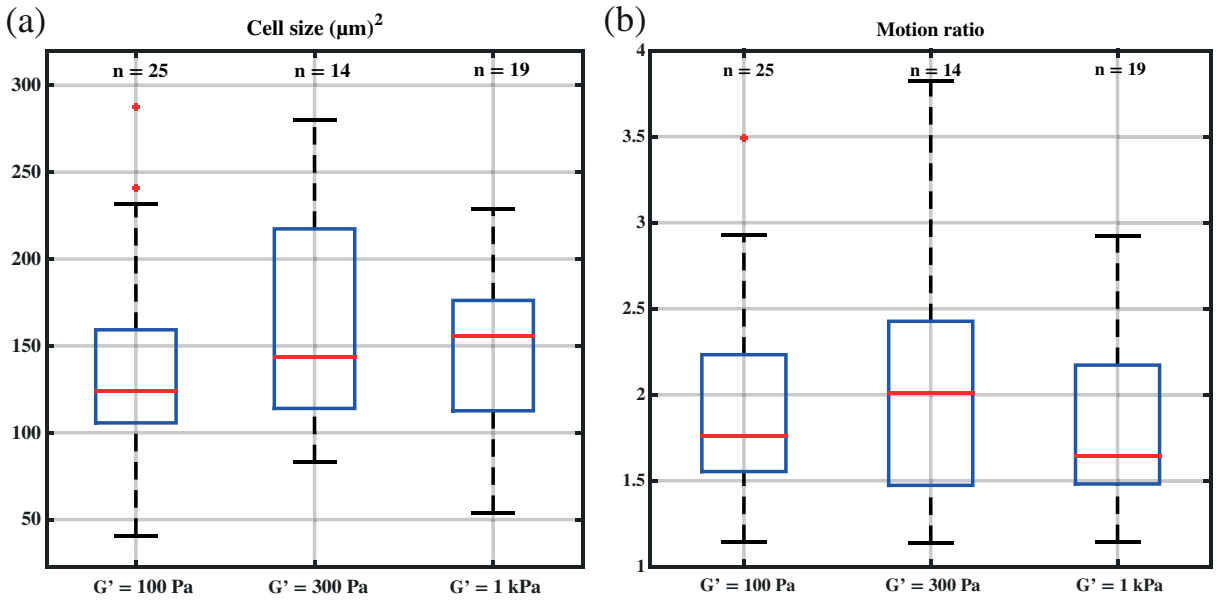

Figure 4.15.: A box plot with cell size values for glioblastoma cells on substrates of varying stiffness is displayed in panel (a). The cell size increased with substrate stiffness. Panel (b) shows a box plot with motion ratio values for different substrate stiffness. The motion ratio was maximal for a shear modulus of G' = 300 Pa.

4.4. Actin network

4.4.1. Microglia

F-actin as part of the acto-myosin cytoskeleton plays an important role in the generation of cell contractility and traction force. In addition, the cytoskeleton including F-actin majorly contributes to the cell shape. In order to study the influence of substrate stiffness on the actin-network, I cultured microglial cells on substrates of varying stiffness. After a defined duration *in vitro* (12 hours and 72 hours), the cells were fixed and the actin network stained.

Microglia that had been cultured on PAA substrates with a shear modulus of 100 Pa for 12 hours showed many processes (44 ± 11, avg$\pm$s.d., n = 14) and few filopodia (Figure 4.16(a)). I found F-actin close to the cell edges and especially visible within the processes. For asymmetric cells, F-actin was mostly found at the most distal parts from the nucleus. I also found fewer processes in close proximity to the cell nucleus.

Microglial cells on a substrate with G' = 300 Pa appeared in a more round or amoeboid shape after 12 hours *in vitro* (Figure 4.16(b)). I found less processes than for the softer substrate (24 ± 13, avg$\pm$s.d., n = 5). Furthermore, F-actin was observed throughout the cell and many single dots of fluorescence were seen.

The cell shape of microglia changed drastically when cultured on glass (Figure 4.16(c)). Long, distinct filopodia with growth cone-like structures at their tips were found. The formation of cell colonies was favored when glass was used as a substrate for cell culturing.

Less distinct substrate stiffness-dependent changes in morphology were observed for microglia after 72 hours *in vitro* (Figures 4.17 and 4.18). For a shear modulus of G' = 100 Pa, I found cells and pairs of cells with a star-like morphology and many long processes (62 ± 14, avg$\pm$s.d., n = 8). F-actin was observed throughout the cell bodies and was predominant within the processes. I identified F-actin in the form of fibers. In cell colonies grown on substrates of G' = 100 Pa, I found F-actin densely distributed around the nuclei and also visible in the processes and filopodia (Figure 4.17(b)).

On PAA substrates with a shear modulus of 300 Pa, single cells showed dominant filopodia with many long and distinct processes (54 ± 23, avg$\pm$s.d., n = 11) after 72 hours *in vitro* (Figure 4.17(a)). F-actin was found within the cell body, inside the filopodia and the processes. Observed cell colonies showed a dense network of F-actin and single fibers were identified (Figure 4.17(b)).

For substrates with G' = 1 kPa, microglia appeared as single cells and in colonies after 72 hours *in vitro* (Figure 4.18, panel (a) and (b)). Single cells were connected through thin filopodia. Cell colonies displayed densely distributed F-actin around the nuclei and fibrous F-actin networks (Figure 4.18(b)). Cells that were cultured on a PAA substrate with shear modulus of 10 kPa for 72 hours *in vitro* cover a large area and show a rather round morphology (Figure 4.18(c)). Cell colonies on the same substrate consisted cells that were connected through filopodia (Figure 4.18(d)). Concentrated F-actin was observed at the most distal ends.

I did not identify F-actin in the form of dominant stress fibers for any substrate stiffness for microglia after 12 or 72 hours *in vitro*.

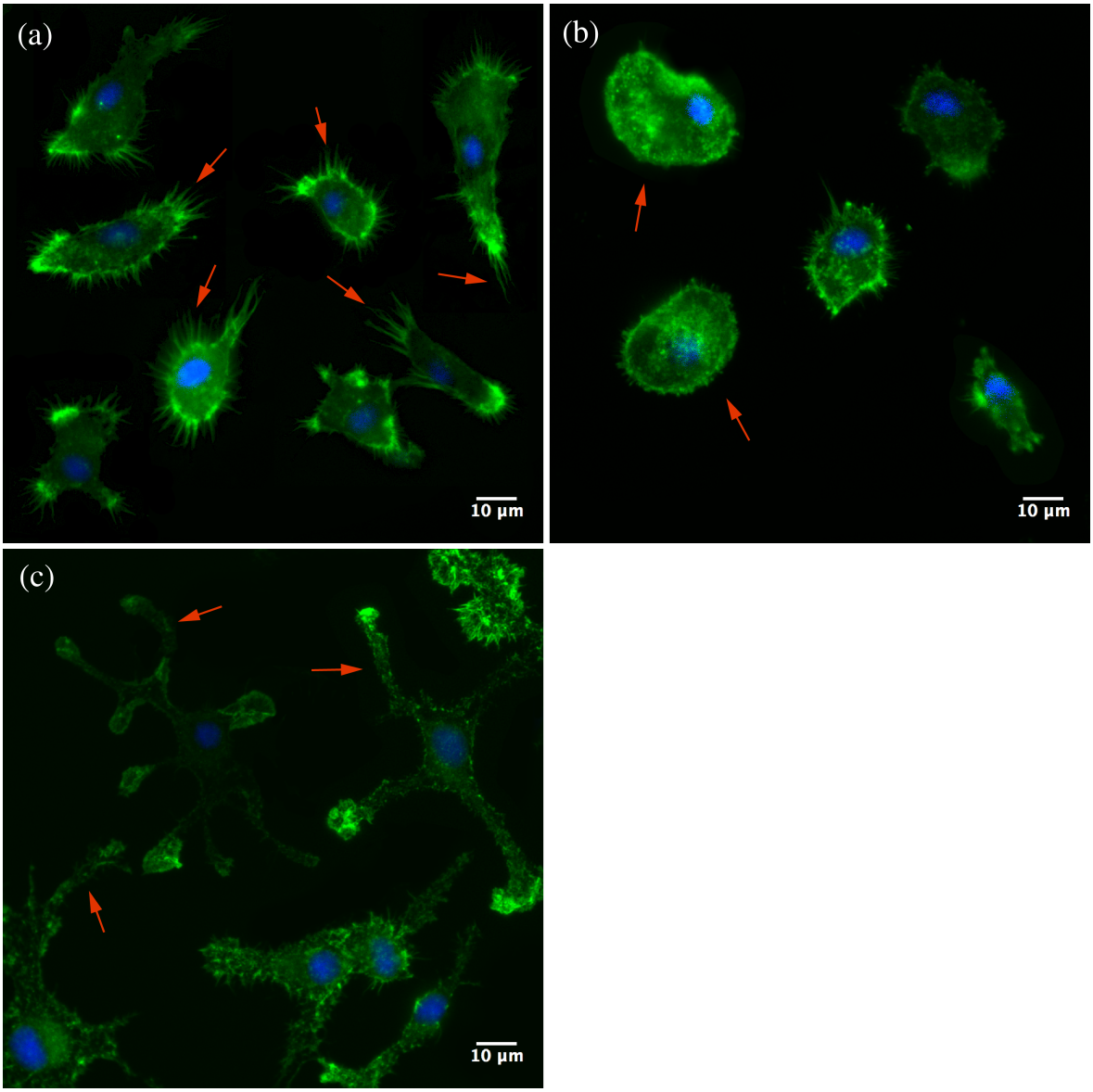

Figure 4.16.: Representative fluorescence images of microglial cells on substrates of different stiffness. The cells were fixed 12 hours after seeding. F-actin appears in green, the nuclei in blue. Panel (a) shows microglial cells on a substrate with G' = 100 Pa. The cells showed various processes (red arrows). The microglial cells in panel (b) had been cultured on gels with a shear modulus of 300 Pa. They showed an ameoboid morphology with few processes (red arrows). Panel (c) shows more complex structures with many filopodia (red arrows) for microglia that were cultured on glass.

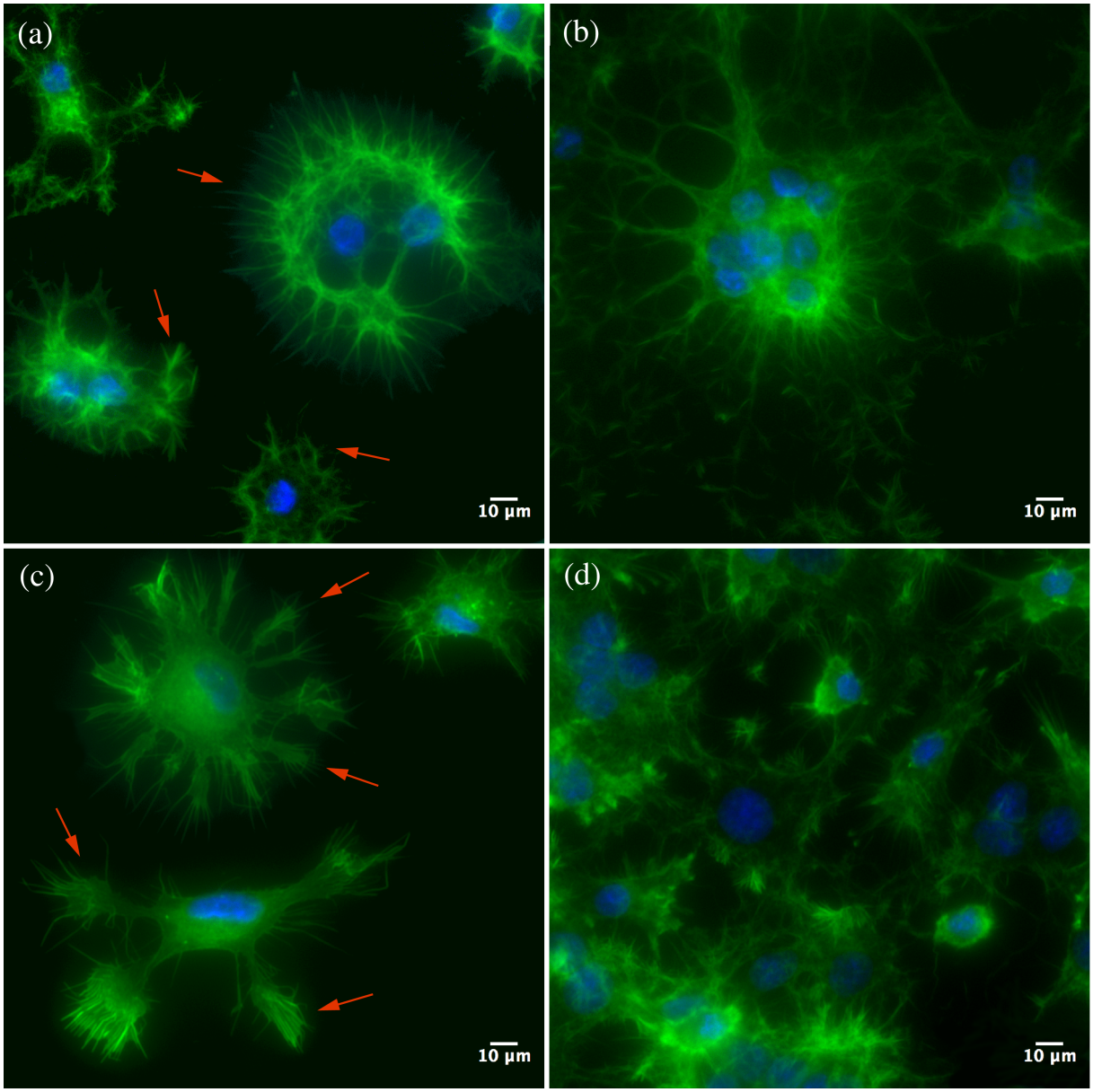

Figure 4.17.: Representative fluorescence images of microglia on substrates of varying stiffness. The cells were cultured for 72 hours prior to fixing. F-actin appears in green, the nuclei in blue. Panel (a) and panel (b) show microglial cells on substrates with G' = 100 Pa. Single cells with many processes ((a), red arrows) and the formation of colonies (b) were found. Panels (c) and (d) show microglial cells on substrates with G' = 300 Pa. The cells appeared as single cells with thick filopodia ((c), red arrows) and in colonies (d).

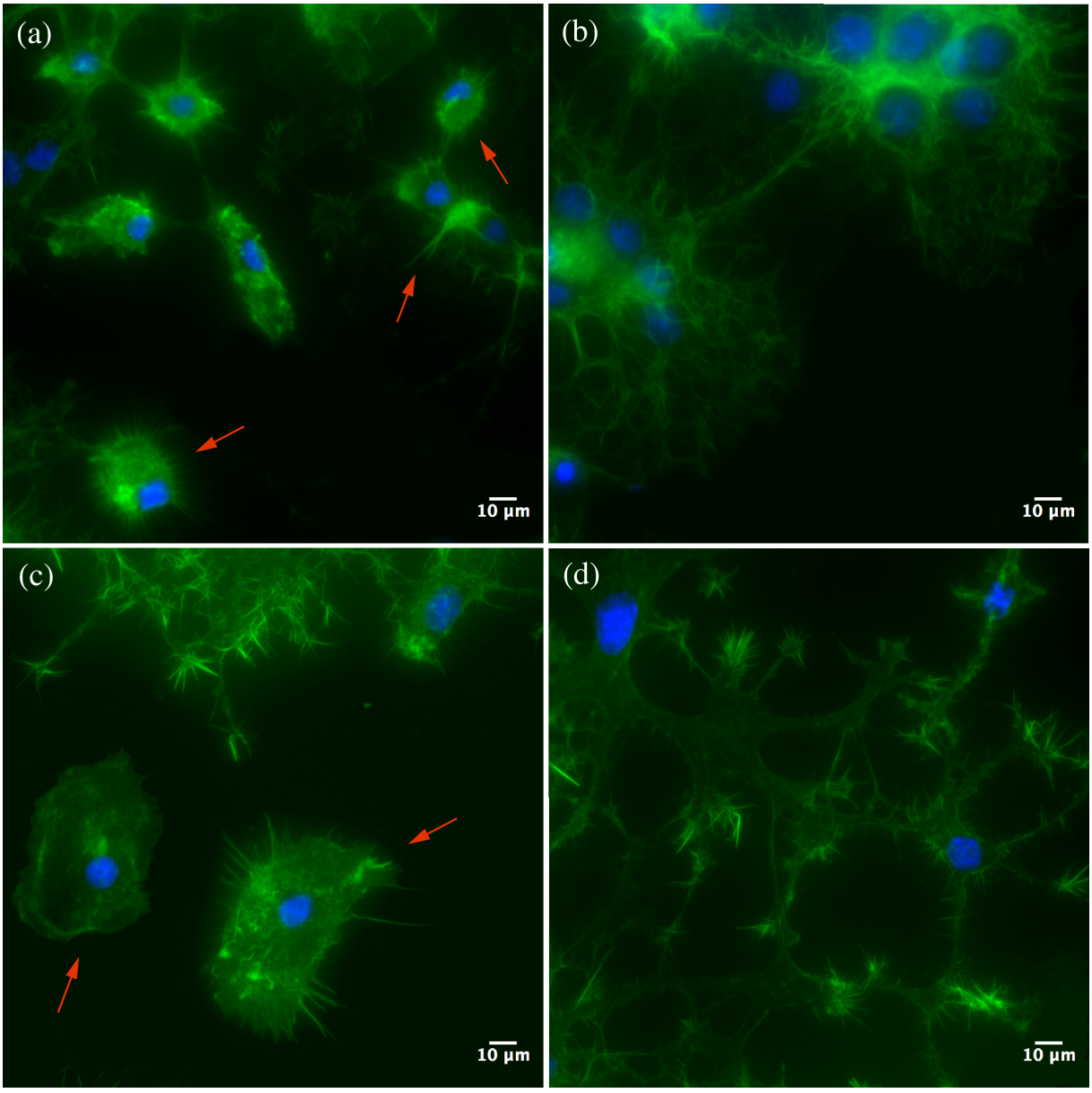

Figure 4.18.: Representative fluorescence images of microglia on substrates with varying stiffness. The cells were fixed 72 hours after seeding. F-actin appears in green, nuclei in blue. Panels (a) and (b) show microglia on a substrate with a shear modulus of G' = 1 kPa. Cells with many processes ((a), red arrows) and colonies consisting of many cells (b) were found. Cells that were grown on substrates with a shear modulus of G' = 10 kPa are displayed in panel (c) and (d). The single cells showed a very large cell size (red arrows) when compared to cells on softer substrates (panel(c)). Colonies of cells were found for the stiff substrate as well (d).

4.4.2. Glioblastoma cells

The previous section dealt with the actin network of microglia cells and the influence of substrate stiffness. In this section, substrate stiffness-dependent changes in the actin network for glioblastoma cells are displayed. In order to obtain images of the actin network of glioblastoma cells, I cultured the cells for a specified duration (4 hours and 15 hours), fixed and stained them.

The actin network of glioblastoma cells that had been cultured on glass for 4 hours *in vitro* did not show a clearly defined cell body (Figure 4.19). F-actin was found in close proximity to the nucleus and also appeared inside the processes.

The morphology of glioblastoma cells changed with substrate stiffness when fixed 15 hours after seeding as outlined in Figures 4.20 and 4.21. On a soft substrate with G' = 100 Pa, glioblastoma cells showed a round shape with F-actin that was distributed throughout the cell (Figure 4.20, panels (a) and (b)). For a stiffer substrate with a shear modulus of G' = 300 Pa, the cells appeared in a slender shape with two or three terminal ends (Figure 4.20, panels (c) and (d)). Stress fibers that span across the cell bodies were observed. I also found cell colonies.

Stress fibers in glioblastoma cells became more predominant on a stiff substrate with G' = 1 kPa (see Figure 4.21). The cells showed a slender shape with either two or three terminal ends and formed colonies.

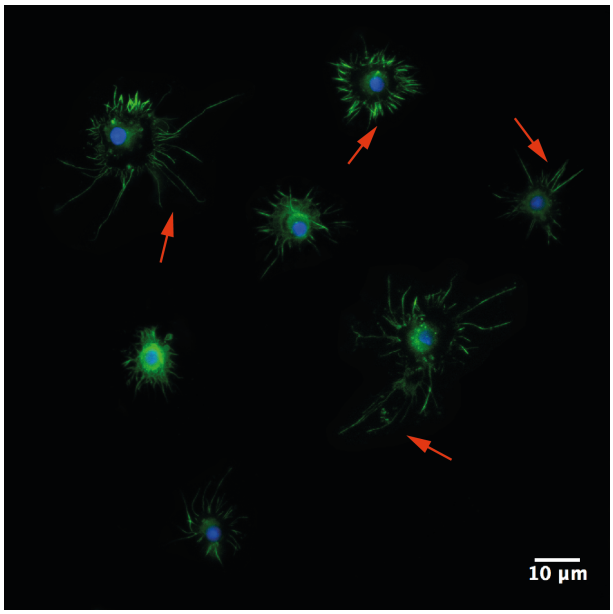

Figure 4.19.: Representative fluorescence image of glioblastoma cells on glass. F-actin appears green, cell nuclei in blue. The cells had been cultured for 4 hours prior to fixing and showed many processes of different length (red arrows).

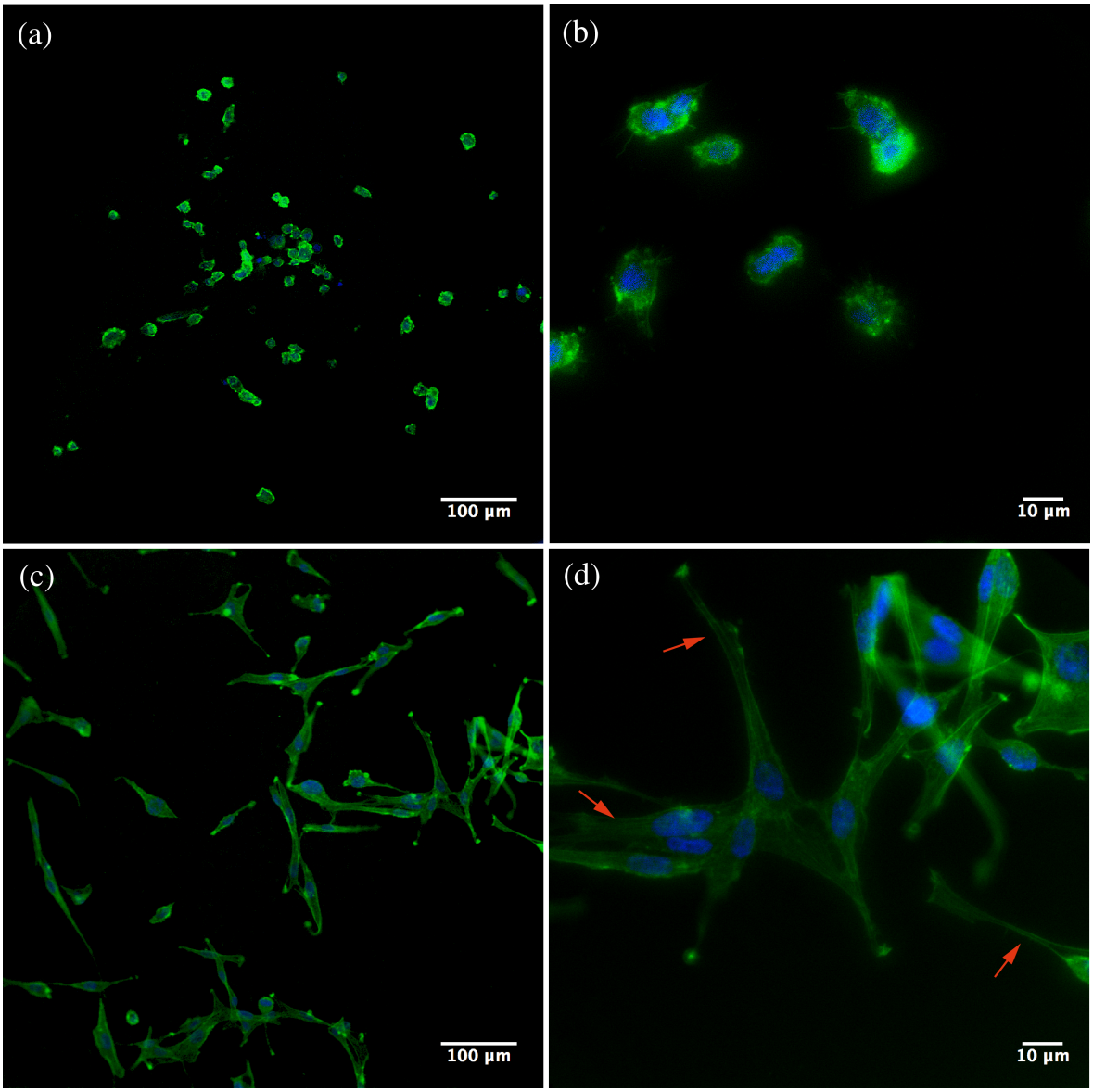

Figure 4.20.: Representative fluorescence images of glioblastoma cells on substrates of varying stiffness. F-actin is displayed in green, nuclei in blue. The cells were fixed 15 hours after seeding. Panel (a) and panel (b) show glioblastoma cells on a substrate with G' = 100 Pa. The cells had a round shape and did not show distinct processes. Glioblastoma cells on a substrate with G' = 300 Pa are displayed in panels (c) and (d). These cells showed a slender shape, with mainly two terminal ends. Stress fibers were visible (red arrows).

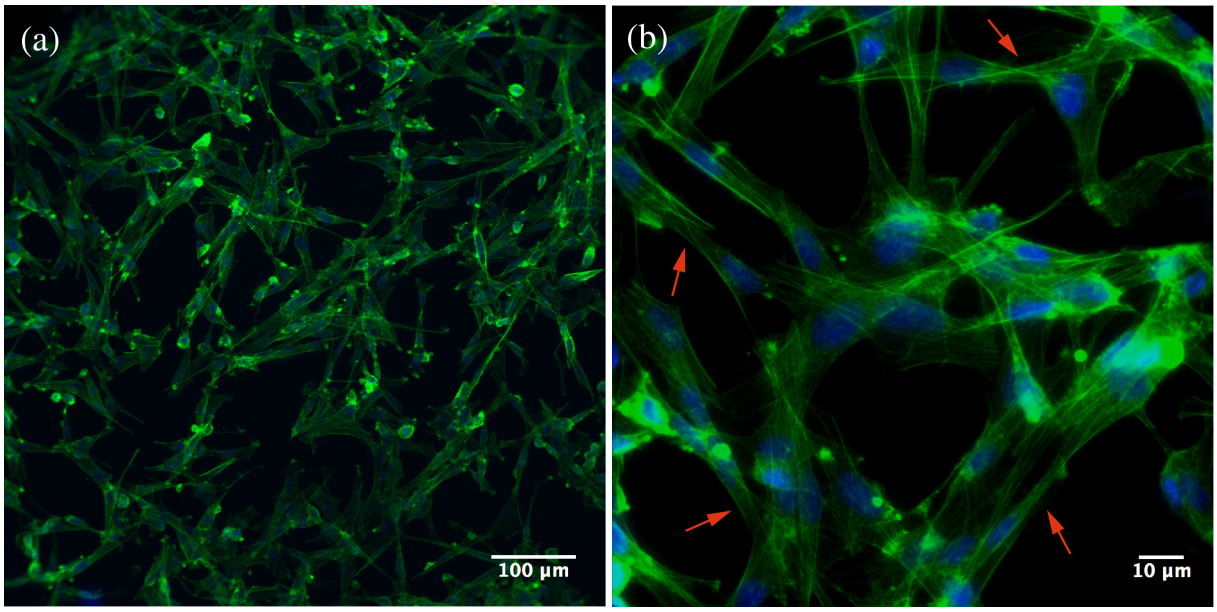

Figure 4.21.: Panel (a) and (b) show representative fluorescence images of glioblastoma cells on a substrate with G' = 1 kPa. The cells were cultured for 15 hours prior to fixing. F-actin appears in green, nuclei in blue. Stress fibers span across cells and were more distinct than for cells on softer substrates (red arrows).

5. Discussion

5.1. Microglia

My results suggest that the traction forces exerted by microglia fluctuate with time and saturate for a shear modulus of 1 kPa. I showed that peak and average traction stresses of microglia increase with substrate stiffness, have a maximum at G' = 1 kPa and decrease for a shear modulus of G' = 2 kPa. Furthermore, measured substrate deformations changed with respect to substrate stiffness and the largest deformations were found at G' = 300 Pa. My findings indicate that the microglial cell size or spread area increases with substrate stiffness. The motion ratio, describing the relative area explored by the cell, showed a dependency on substrate stiffness and was smallest on substrates with a shear modulus of G' = 300 Pa.

Temporal variations of the magnitude of traction forces have also been observed for other cell types e.g. for epithelial cells or amoeboids [105, 106]. It has been shown that the temporal changes in traction forces are tightly linked to cell migration [105]. The oscillations of contractile forces correlate well with the cell's average migration speed [106]. The cell motility cycle is commonly divided into phases with characteristic features. Uchida et al. describe a biphasic locomotory behavior in Dictyostelium cells consisting of retraction and extension phase [107]. Bastounis et al. differentiante a protrusion phase, a contraction phase, a retraction phase and a relaxation phase [108]. These phases are identified by the the location and magnitude of traction forces. In addition to variations of traction forces due to the motility cycle, the extension and retraction of processes could have an influence as well. Nimerjahn et al. showed that microglia constantly probe their environment and change the length of their processes dynamically [39]. This hypothesis is supported be the finding that focal adhesion form preferentially along the cell periphery and cellular protrusions [109, 110].

My results show that peak and average traction stresses fluctuate with time, increase with stiffness and have a maximum at G' = 1 kPa. The detected substrate deformations at G' = 2 kPa are below the smallest detectable displacement of fluorescent beads. Therefore, it is likely that the traction stresses saturate or reach a plateau for a shear modulus of 1 kPa. This is a typical value for brain stiffness [59]. Furthermore, Moshayedi et al. found primary astrocytes (another glial cell type) to change their morphology from a 'soft' to a 'stiff' phenotype on substrates with a shear modulus of 1 kPa [18].

Traction forces of fibroblasts and endothelial cells also increase with substrate stiffness until they reach a plateau for a certain rigidity [92, 111, 112]. One of the reasons for a positive correlation between substrate stiffness and traction forces could be the number

of focal adhesions. Focal adhesions play an important role in the transmission of forces between cells and substrate and their number increases with substrate stiffness [112, 113]. In addition, Tolic-Norrelykke et al. and Califano et al. showed that traction stress increases with cell size [92, 114]. We found a positive correlation between substrate stiffness and cell size for microglial cells. This trend has been shown for fibroblasts as well [111]. The substrate stiffness for the maximum cell traction force depends on the cell type [115]. For example, neurons show the largest traction force values on much softer substrates than endothelial cells.

Exerted forces also depend on surface ligand density [116]. The PAA gels used in our experiments show a constant ligand surface density that is decoupled from the stiffness of the substrate [96].

The measured substrate deformations change with respect to substrate stiffness. Interestingly, the largest substrate deformations are not found for the softest substrate. This characteristic is seen for both, peak and average deformations. One hypothesis is that the molecular clutches of the motor-clutch system fail spontaneously on soft substrates before a deformation can be triggered [115].

My findings suggest that microglial cells adapt both, strain and traction stress to substrate stiffness. This indicates some adaptation of the cell to its mechanical environment due to some feedback mechanism.

Using data from the upright setup, I showed that the motion ratio is substrate stiffness-dependent with the smallest relative area explored on a substrate with G' = 300 Pa. For the same substrate stiffness I found the largest spreading area and the largest substrate deformations. It is likely that the cells are more spread, stronger adhered, deform the substrate more, move less and therefore show a small motion ratio on a substrate with G' = 300 Pa.

5.1.1. Influence of LPS

In my experiments, LPS decreased the traction stresses for substrates with G' = 300 Pa and G' = 1 kPa. My results indicate that the influence is more significant for average traction stress than for peak traction stress.

It has been shown that the injection of LPS induces microglia activation *in vivo* [44, 45]. Once activated, microglia become highly motile [117]. In the course of this transition into the activated stage microglia change their morphology. They start withdrawing their processes immediately and generate new shorter processes after approximately 40 minutes [118]. These newly generated processes are much more dynamic than the initial ones. The initial withdrawal of processes takes place within minutes after activation and is therefore relevant for our experiments. Hence, the decrease in traction forces could be triggered by the withdrawal of processes and the change in cell morphology. The overall contractility of the cell may be affected, hence the larger significance in terms of average traction stress. A decrease in traction force is often coupled to an increase in migration velocity, indicating how force and motility are coupled to cell function [119].

5.1.2. Actin network

Microglial cells showed changes in their actin network morphology with respect to substrate stiffness. Predominantly spherical morphologies were observed on soft substrates. On the contrary, I found well spread microglia with many filopodia on stiffer substrates. Observed differences became less significant the longer the cells were cultured on the substrates. In addition, I did not observe dominant stress fibers irrespective of substrate stiffness.

Microglial cell morphology in bright field images depends on substrate stiffness as outlined by Moshayedi et al. [17]. While microglia show spherical morphologies on softer substrates, they spread more and extend processes and filopodia on stiff substrates. Actin, as a main component of the cytoskeleton, contributes majorly to changes in cell morphology [120]. My results show more spherical shapes of the actin network for softer substrates and complex structures with filopodia on glass.

I noted the absence of dominant stress fibers in microglia irrespective of substrate stiffness. This characteristic has also been noted in macrophages. Allen et al. indicated that macrophages show fine actin cables instead of well defined stress fibers [121]. This may be the case for microglia, the macrophages of the nervous system, as well.

Experiments indicated that the morphology of microglia stays relatively constant for the first 24 hours of culturing on glass [122]. My results suggest that the actin network of microglia changes between 12 hours and 72 hours of culturing. More processes and filopodia were visible after 72 hours and the substrate stiffness appeared to have a less significant influence on the actin network morphology.

5.2. Inverted vs. upright setup

My results show that traction stresses and detected deformations were significantly higher when the upright setup was used. In addition, deformations were detected by the 2D cross-correlation algorithm for cells on substrates that were very likely too stiff to be detectably deformed by microglia. These findings indicate that the upright setup generated flawed input for the traction force analysis.

The smearing effect as shown in Figure 4.8 suggests that the cells scatter the fluorescent light that is emitted by the beads in the gel. It has been shown that scattering properties of cells are influenced by cellular biochemical and morphological structure [123]. In addition, the light-scattering effects of cytoskeletal molecules were observed [124]. Various researchers used multiangle light-scattering to detect morphological differences, cell size and cell volume. [125–128]. Furthermore, light scattering experiments were performed to extract morphological parameters such as radius and cell wall thickness of single bacteria [129]. Therefore, it is likely that the light-scattering effect of cells is responsibly for the the observed imaging artifacts.

The relative difference between median values of the upright and the inverse setup was smaller for the average stress and decreased with substrate stiffness. It is possible that

the effect is larger for softer substrates because in this case the cell morphology favors the scattering of light. On softer gels the cell spread area is smaller, cells are thus likely higher, which leads to more scattering and an apparent movement of the beads with cell movement. Hence, for samples with significant height (a multiple of the wavelength of the emitted fluorescent light), upright microscopy can lead to imaging artifacts leading to wrong TFM results.

5.3. Glioblastoma

Since the traction force experiments with glioblastoma cells were done using the upright setup, the results have to be considered with caution (see **Inverted vs. upright setup**).

My results suggest that the traction stresses and cell size increase with substrate stiffness. I showed that glioblastoma cells of different tumor fractions show differences in terms of traction stress. Furthermore, the motion ratio of glioblastoma cells was found to be significantly higher than for microglial cells.

Increasing traction stresses with substrate stiffness were also found for T24 bladder cancer cells. The results from Ambrosi et al. indicated that T24 cells show the highest velocity of migration on soft substrates [119]. They hypothesized that less-adhering cells exert less traction force and move faster. On the contrary, Ulrich et al. hypothesized that glioblastoma cells migrate more rapidly on stiff substrates [22]. Migration velocities may be correlated with invasiveness [130]. I found that the motion ratio of glioblastoma cells had the smallest value for the stiff gel, where the highest traction stresses were observed. That means the relative area explored by the cells was smaller for the stiff substrate. In addition, I found a higher motion ratio for glioblastoma cells as compared to microglia. This could be an indicator for an increased affinity for glioblastoma cells to migrate and an evidence for their invasiveness [131].

I showed that the cell size of glioblastoma cells increases with substrate stiffness, supporting the findings by Ulrich et al. [22]. My results also agree on substrate stiffness-dependent changes in cell morphology. For stiffer substrates, glioblastoma cells formed stress fibers and showed a more spread morphology. All results taken together, glioblastoma cells are sensitive to changes in substrate stiffness.

Glioblastoma cells of different tumor fractions showed differences in terms of traction stress. Cells from deeper tumor fractions (T8) showed higher average and peak traction stresses on the two stiff substrates (G' = 300 Pa and G' = 1 kPa). On the soft substrate, cells of intermediate depth (T5) showed the highest traction stresses. Glioblastoma cells of different tumor fractions might prefer different values of substrate stiffness. Spatial variations of stiffness in glioblastoma has not been assessed in detail, but studies suggest that increased stiffness of tumor tissue might promote the malignancy [19]. Traction forces of glioblastoma cells may provide a mean to distinguish subgroups of these tumor cells. The data could be used to investigate the invasiveness of cells from different tumor fractions. To generate more meaningful results, an inverted setup should be used to confirm traction stresses of glioblastoma cells.

6. Conclusion

I have demonstrated that microglial cells are capable of sensing and adapting to substrate stiffness.

The cell's ability to convert a mechanical stimuli into a biochemical signal ('mechanotransduction') has been described before [132, 133]. It is likely that microglial cells use mechanotransduction to adapt their functional profile to the stiffness of their microenvironment. The increase in traction stresses on stiffer substrates might lead a change in cellular function. This hypothesis is supported by the finding that microglia respond to unphysiologically stiff surfaces with an acute and chronic inflammatory reaction [17].

Investigating the inflammatory response, traction stresses and migration of microglial cells as a function of substrate stiffness, contributes to a better understanding of numerous pathologies of the nervous system. In addition, new findings potentially lead to the development of novel therapies.

Traction stresses of glioblastoma cells from spatially different tumor fractions showed significant differences. Therefore, traction force microscopy could be a mean to differentiate subgroups of glioblastoma cells. Investigating the relation between traction stresses, invasiveness and aggressiveness of glioblastoma cells will potentially lead to new strategies to treat glioblastomas.

ECM stiffness influences the structure, motility and proliferation of glioblastoma cells [21]. Therefore, further insights could be gained by studying spatial differences in tumor stiffness. Relating the findings to the traction stresses of glioblastoma cells from spatially different tumor fractions will lead to a better understanding of tumor progression.

The comparison of results from an upright and an inverted setup for TFM imaging revealed potential errors that occur with an upright setup. The light-scattering effect of cells can falsify the acquisition of TFM images. It can be concluded that for samples with significant height, upright microscopy can lead to imaging artifacts leading to wrong TFM results.

Bibliography

[1] Frederik Vilhardt. Microglia: Phagocyte and glia cell. *International Journal of Biochemistry and Cell Biology*, 37(1):17–21, 2005.

[2] H Li, J Newcombe, N P Groome, and M L Cuzner. Characterization and distribution of phagocytic macrophages in multiple sclerosis plaques. *Neuropathology and applied neurobiology*, 19(3):214–223, 1993.

[3] H. Neumann, M. R. Kotter, and R. J M Franklin. Debris clearance by microglia: An essential link between degeneration and regeneration. *Brain*, 132(Pt 2):288–295, 2009.

[4] Samuel David and Antje Kroner. Repertoire of microglial and macrophage responses after spinal cord injury. *Nat Rev Neurosci*, 12(7):388–399, 2011.

[5] Bryan C Hains and Stephen G Waxman. Activated microglia contribute to the maintenance of chronic pain after spinal cord injury. *The Journal of neuroscience : the official journal of the Society for Neuroscience*, 26(16):4308–4317, 2006.

[6] Andre Kamkin and Irina Kiseleva, editors. *Mechanosensitivity of Cells from Various Tissues*. Academia, 2005.

[7] Dong Li, Farhan Chowdhury, Jianjun Cheng, Ning Wang, Fei Wang, and Jiaxi Zhou. Role of mechanical factors in fate decisions of stem cells. *Regen Med.*, 6(2):229–240, 2011.

[8] Timothy M Maul, Douglas W Chew, Alejandro Nieponice, and David A Vorp. Mechanical stimuli differentially control stem cell behavior: morphology, proliferation, and differentiation. *Biomechanics and modeling in mechanobiology*, 10(6):939–953, 2011.

[9] Brooke N Mason, Joseph P Califano, and Cynthia a Reinhart-king. Matrix Stiffness: A Regulator of Cellular Behavior and Tissue Formation. *Engineering Biomaterials for Regenerative Medicine*, 2(3):19–38, 2012.

[10] Dennis E Discher, Paul Janmey, and Yu-Li Wang. Tissue cells feel and respond to the stiffness of their substrate. *Science*, 310(5751):1139–1143, 2005.

[11] S. Wang and P. G. Wolynes. Active contractility in actomyosin networks. *Proceedings of the National Academy of Sciences*, 109:6446–6451, 2012.

[12] Juliet Lee, Michelle Leonard, Tim Oliver, Akira Ishihara, and Ken Jacobson. Traction forces generated by locomoting keratocytes. *Journal of Cell Biology*, 127(6 II):1957–1964, 1994.

[13] Boris Martinac. Mechanosensitive ion channels: molecules of mechanotransduction. *Journal of cell science*, 117(Pt 12):2449–2460, 2004.

[14] D Riveline, E Zamir, N Q Balaban, U S Schwarz, T Ishizaki, S Narumiya, Z Kam, B Geiger, and A D Bershadsky. Focal contacts as mechanosensors: externally applied local mechanical force induces growth of focal contacts by an mDia1-dependent and ROCK-independent mechanism. *The Journal of cell biology*, 153(6):1175–1186, 2001.

[15] Catherine G Galbraith, Kenneth M Yamada, and Michael P Sheetz. The relationship between force and focal complex development. *The Journal of cell biology*, 159(4):695–705, 2002.

[16] Jérôme Solon, Ilya Levental, Kheya Sengupta, Penelope C Georges, and Paul a Janmey. Fibroblast adaptation and stiffness matching to soft elastic substrates. *Biophysical journal*, 93(12):4453–4461, 2007.

[17] Pouria Moshayedi, Gilbert Ng, Jessica C F Kwok, Giles S H Yeo, Clare E Bryant, James W Fawcett, Kristian Franze, and Jochen Guck. The relationship between glial cell mechanosensitivity and foreign body reactions in the central nervous system. *Biomaterials*, 35(13):3919–25, 2014.

[18] Pouria Moshayedi, Luciano Da F Costa, Andreas Christ, Stephanie P Lacour, James Fawcett, Jochen Guck, and Kristian Franze. Mechanosensitivity of astrocytes on optimized polyacrylamide gels analyzed by quantitative morphometry. *Journal of physics. Condensed matter : an Institute of Physics journal*, 22(19):194114, 2010.

[19] Andrew Rape, Badriprasad Ananthanarayanan, and Sanjay Kumar. Engineering strategies to mimic the glioblastoma microenvironment. *Advanced Drug Delivery Reviews*, 79-80:172–183, 2014.

[20] Michael Weller, Barbara Fisher, Martin J B Taphoorn, Karl Belanger, Alba A Brandes, Christine Marosi, Ulrich Bogdahn, Jürgen Curschmann, and Robert C Janzer. Radiotherapy plus concomitant and adjuvant temozolomide for glioblastoma. *Cancer/Radiothérapie*, 9(3):196–197, 2005.

[21] Andrea Sottoriva, Inmaculada Spiteri, Sara G M Piccirillo, Anestis Touloumis, V Peter Collins, John C Marioni, Christina Curtis, Colin Watts, and Simon Tavaré. Intratumor heterogeneity in human glioblastoma reflects cancer evolutionary dynamics. *Proceedings of the National Academy of Sciences of the United States of America*, 110(10):4009–14, 2013.

[22] Theresa a. Ulrich, Elena M. De Juan Pardo, and Sanjay Kumar. The mechanical rigidity of the extracellular matrix regulates the structure, motility, and proliferation of glioma cells. *Cancer Research*, 69(10):4167–4174, 2009.

[23] Ugo Ndubaku and Maria Elena De Bellard. Glial cells: Old cells with new twists. *Acta Histochem*, 110(3):182–195, 2008.

[24] S M Dombrowski, C C Hilgetag, and H Barbas. Quantitative architecture distinguishes prefrontal cortical systems in the rhesus monkey. *Cerebral cortex*, 11:975–988, 2001.

[25] Frederico a C Azevedo, Ludmila R B Carvalho, Lea T. Grinberg, José Marcelo Farfel, Renata E L Ferretti, Renata E P Leite, Wilson Jacob Filho, Roberto Lent, and Suzana Herculano-Houzel. Equal numbers of neuronal and nonneuronal cells make the human brain an isometrically scaled-up primate brain. *Journal of Comparative Neurology*, 513(5):532–541, 2009.

[26] D. P. Pelvig, H. Pakkenberg, a. K. Stark, and B. Pakkenberg. Neocortical glial cell numbers in human brains. *Neurobiology of Aging*, 29(11):1754–1762, 2008.

[27] D L Montgomery. Astrocytes: form, functions, and roles in disease. *Veterinary pathology*, 31(1994):145–167, 1994.

[28] Raymond C. Koehler, Richard J. Roman, and David R. Harder. Astrocytes and the regulation of cerebral blood flow. *Trends in Neurosciences*, 32(3):160–169, 2009.

[29] K F Lunn, P W Baas, and I D Duncan. Microtubule organization and stability in the oligodendrocyte. *The Journal of neuroscience : the official journal of the Society for Neuroscience*, 17(13):4921–4932, 1997.

[30] N Baumann and D Pham-Dinh. Biology of oligodendrocyte and myelin in the mammalian central nervous system. *Physiological reviews*, 81(2):871–927, 2001.

[31] C.B. Tomcik. Ependyma. In *Encyclopedia of the Neurological Sciences*, pages 70–71. Elsevier, 2014.

[32] Kettenmann H. Hanisch UK. Microglia: active sensor and versatile effector cells in the normal and pathologic brain. *Nat Neurosci.*, 10(11):1387–94., 2007.

[33] PD Rio-Hortega. El "tercer elemento" de los centros nerviosos. Poder fagocitario y movilidad de la microglia. *Bol de la Soc espa- nola de Biol*, Ano ix:154–166, 1919.

[34] Bertrand Joseph, Jose Luis Venero, and John M Walker. A Brief Overview of Multitalented Microglia. In *Methods in Molecular Biology*, volume 1041, pages 3–8. Springer, 2013.

[35] I Ferrer, E Bernet, E Soriano, T Del Rio, and M Fonseca. Naturally occurring cell death in the cerebral cortex of the rat and removal of dead cells by transitory phagocytes. *Neuroscience*, 39(2):451–458, 1990.

[36] W. J. Streit. Microglia and macrophages in the developing CNS. *NeuroToxicology*, 22(2001):619–624, 2001.

[37] G. Rabchevsky and W. J. Streit. Grafting of cultured microglial cells into the lesioned spinal cord of adult rats enhances neurite outgrowth. *Journal of Neuroscience Research*, 47(1):34–48, 1997.

[38] Helmut Kettenmann, Uwe-Karsten Hanisch, Mami Noda, and Alexei Verkhratsky. Physiology of microglia. *Physiological reviews*, 91:461–553, 2011.

[39] Axel Nimmerjahn, Frank Kirchhoff, and Fritjof Helmchen. Resting microglial cells are highly dynamic surveillants of brain parenchyma in vivo. *Science*, 308(5726):1314–8, 2005.

[40] G W Kreutzberg. Microglia: a sensor for pathological events in the CNS. *Trends Neurosci.*, 19:312–318, 1996.

[41] Dimitrios Davalos, Jaime Grutzendler, Guang Yang, Jiyun V Kim, Yi Zuo, Steffen Jung, Dan R Littman, Michael L Dustin, and Wen-Biao Gan. ATP mediates rapid microglial response to local brain injury in vivo. *Nat Neurosci*, 8(6):752–758, 2005.

[42] E J Davis, T D Foster, and W E Thomas. Cellular forms and functions of brain microglia. *Brain Research Bulletin*, 34(1):73–78, 1994.

[43] Elisabetta Polazzi and Antonio Contestabile. Reciprocal interactions between microglia and neurons: from survival to neuropathology. *Reviews in the neurosciences*, 13(3):221–242, 2002.

[44] Hong Zhou, Benoît M Lapointe, Stephen R Clark, Lori Zbytnuik, and Paul Kubes. A requirement for microglial TLR4 in leukocyte recruitment into brain in response to lipopolysaccharide. *Journal of immunology (Baltimore, Md. : 1950)*, 177(11):8103–8110, 2006.

[45] Z. Chen, W. Jalabi, K. B. Shpargel, K. T. Farabaugh, R. Dutta, X. Yin, G. J. Kidd, C. C. Bergmann, S. a. Stohlman, and B. D. Trapp. Lipopolysaccharide-Induced Microglial Activation and Neuroprotection against Experimental Brain Injury Is Independent of Hematogenous TLR4. *Journal of Neuroscience*, 32(34):11706–11715, 2012.

[46] Knut Biber, Harald Neumann, Kazuhide Inoue, and Hendrikus W G M Boddeke. Neuronal 'On' and 'Off' signals control microglia. *Trends in Neurosciences*, 30(11):596–602, 2007.

[47] Carol A Colton and Donna M Wilcock. Assessing activation states in microglia. *CNS & neurological disorders drug targets*, 9(2):174–191, 2010.

[48] Michal Schwartz, Oleg Butovsky, Wolfgang Brück, and Uwe Karsten Hanisch. Microglial phenotype: Is the commitment reversible? *Trends in Neurosciences*, 29(2):68–74, 2006.

[49] Jason F Harrison, Mikael L Rinne, Mark R Kelley, Nadiya M Druzhyna, Glenn L Wilson, and Susan P Ledoux. Microglial Control of Neuronal Death and Synaptic Properties. *Glia*, 55:1416–1425, 2007.

[50] A E Cardona, R M Ransohoff, and K Akassoglou. Chapter 41 - Microglia. In *Pattering and Cell Type Specification in the Developing CNS and PNS*, volume 1, pages 803–817. Elsevier Inc., 2013.

[51] Egle Solito and Magdalena Sastre. Microglia function in Alzheimer's disease. *Frontiers in Pharmacology*, 3:1–10, 2012.

[52] Tony Wyss-Coray. Inflammation in Alzheimer disease: driving force, bystander or beneficial response? *Nature medicine*, 12(9):1005–1015, 2006.

[53] Chao Zhao, Wen Wu Li, and Robin J M Franklin. Differences in the early inflammatory responses to toxin-induced demyelination are associated with the age-related decline in CNS remyelination. *Neurobiology of Aging*, 27:1298–1307, 2006.

[54] Wolfgang J. Streit. Microglial senescence: does the brain's immune system have an expiration date? *Trends in Neurosciences*, 29(9):506–510, 2006.

[55] Wolfgang J. Streit and Qing Shan Xue. Alzheimer's disease, neuroprotection, and CNS immunosenescence. *Frontiers in Pharmacology*, 3:1–7, 2012.

[56] Kristian Franze. The mechanical control of nervous system development. *Development*, 140:3069–77, 2013.

[57] D Bray. Axonal growth in response to experimentally applied mechanical tension. *Developmental biology*, 102(2):379–389, 1984.

[58] Timo Betz, Daniel Koch, Yun-Bi Lu, Kristian Franze, and Josef a Käs. Growth cones as soft and weak force generators. *Proceedings of the National Academy of Sciences of the United States of America*, 108(33):13420–5, 2011.

[59] J. a W van Dommelen, T. P J van der Sande, M. Hrapko, and G. W M Peters. Mechanical properties of brain tissue by indentation: Interregional variation. *Journal of the Mechanical Behavior of Biomedical Materials*, 3(2):158–166, 2010.

[60] Andreas F. Christ, Kristian Franze, Helene Gautier, Pouria Moshayedi, James Fawcett, Robin J M Franklin, Ragnhildur T. Karadottir, and Jochen Guck. Mechanical difference between white and gray matter in the rat cerebellum measured by scanning force microscopy. *Journal of Biomechanics*, 43(15):2986–2992, 2010.

[61] K K Darvish and J R Crandall. Nonlinear viscoelastic effects in oscillatory shear deformation of brain tissue. *Medical engineering & physics*, 23:633–645, 2001.

[62] Erik G Takhounts, Jeff R Crandall, and Kurosh Darvish. On the importance of nonlinearity of brain tissue under large deformations. *Stapp car crash journal*, 47:79–92, 2003.

[63] Curtis L. Johnson, Matthew D J McGarry, Armen a. Gharibans, John B. Weaver, Keith D. Paulsen, Huan Wang, William C. Olivero, Bradley P. Sutton, and John G. Georgiadis. Local mechanical properties of white matter structures in the human brain. *NeuroImage*, 79:145–152, 2013.

[64] John B Weaver, Adam J Pattison, Matthew D McGarry, Irina M Perreard, Jessica G Swienckowski, Clifford J Eskey, S Scott Lollis, and Keith D Paulsen. Brain mechanical property measurement using MRE with intrinsic activation. *Physics in Medicine and Biology*, 57:7275–7287, 2012.

[65] Benjamin S Elkin, Evren U Azeloglu, Kevin D Costa, and Barclay 3rd Morrison. Mechanical heterogeneity of the rat hippocampus measured by atomic force microscope indentation. *Journal of neurotrauma*, 24(5):812–822, 2007.

[66] Thibault P. Prevost, Asha Balakrishnan, Subra Suresh, and Simona Socrate. Biomechanics of brain tissue. *Acta Biomaterialia*, 7(1):83–95, 2011.

[67] Shaokoon Cheng, Elizabeth C Clarke, and Lynne E Bilston. Rheological properties of the tissues of the central nervous system: a review. *Medical engineering & physics*, 30(10):1318–1337, 2008.

[68] Badar Rashid, Michel Destrade, and Michael D. Gilchrist. Influence of preservation temperature on the measured mechanical properties of brain tissue. *Journal of Biomechanics*, 46:1276–1281, 2013.

[69] M Hrapko, J a W van Dommelen, G W M Peters, and J S H M Wismans. The influence of test conditions on characterization of the mechanical properties of brain tissue. *Journal of biomechanical engineering*, 130(June 2008):031003, 2008.

[70] GerhardA. Holzapfel. *Nonlinear Solid Mechanics: A Continuum Approach for Engineering*, volume 37. Kluwer Academic Publishers, 2000.

[71] R.R.Wayne Wayne Albers. Chapter 2 - Cell Membrane Structures and Functions. In Scott T BradyGeorge J SiegelR. Wayne AlbersDonald L B T Basic Neurochemistry

(Eighth Edition) Price, editor, *Basic Neurochemistry*, pages 26–39. Academic Press, New York, 2012.

[72] Bruno Pontes, Yareni Ayala, Anna Carolina C Fonseca, Luciana F. Romão, Racele F. Amaral, Leonardo T. Salgado, Flavia R. Lima, Marcos Farina, Nathan B. Viana, Vivaldo Moura-Neto, and oysés M. Nussenzveig. Membrane Elastic Properties and Cell Function. *PLoS ONE*, 8(7), 2013.

[73] Alba Diz-Muñoz, Daniel a. Fletcher, and Orion D. Weiner. Use the force: Membrane tension as an organizer of cell shape and motility. *Trends in Cell Biology*, 23(2):47–53, 2013.

[74] F Guilak, J R Tedrow, and R Burgkart. Viscoelastic properties of the cell nucleus. *Biochemical and biophysical research communications*, 269:781–786, 2000.

[75] C Guilluy, L D Osborne, Landeghem L Van, L Sharek, R Superfine, R Garcia-Mata, and K Burridge. Isolated nuclei adapt to force and reveal a mechanotransduction pathway in the nucleus. *Nat.Cell Biol.*, 16(4):376–381, 2014.

[76] Ashkan Vaziri and M. R K Mofrad. Mechanics and deformation of the nucleus in micropipette aspiration experiment. *Journal of Biomechanics*, 40:2053–2062, 2007.

[77] L Mahadevan, E Moeendarbary, and L Valon. Cellular Hydraulics Suggests a Poroelastic Cytoplasm Rheology. Technical report, Harvard University, 2013.

[78] Daniel a Fletcher and R Dyche Mullins. Cell mechanics and the cytoskeleton. *Nature*, 463(January):485–492, 2010.

[79] John E. Eriksson, Thomas Dechat, Boris Grin, Brian Helfand, Melissa Mendez, Hanna Mari Pallari, and Robert D. Goldman. Introducing intermediate filaments: From discovery to disease. *Journal of Clinical Investigation*, 119(7):1763–1771, 2009.

[80] Milos Pekny and E. Birgitte Lane. Intermediate filaments and stress. *Experimental Cell Research*, 313:2244–2254, 2007.

[81] Eric W Flitney, Edward R Kuczmarski, Stephen a Adam, and Robert D Goldman. Insights into the mechanical properties of epithelial cells: the effects of shear stress on the assembly and remodeling of keratin intermediate filaments. *The FASEB journal : official publication of the Federation of American Societies for Experimental Biology*, 23:2110–2119, 2009.

[82] Clifford P. Brangwynne, Frederick C. MacKintosh, Sanjay Kumar, Nicholas a. Geisse, Jennifer Talbot, L. Mahadevan, Kevin K. Parker, Donald E. Ingber, and David a. Weitz. Microtubules can bear enhanced compressive loads in living cells because of lateral reinforcement. *Journal of Cell Biology*, 173(5):733–741, 2006.

[83] Taviare Hawkins, Matthew Mirigian, M. Selcuk Yasar, and Jennifer L. Ross. Mechanics of microtubules. *Journal of Biomechanics*, 43(1):23–30, 2010.

[84] Joshua Pringle, Amutha Muthukumar, Amanda Tan, Laura Crankshaw, Leslie Conway, and Jennifer L Ross. Microtubule organization by kinesin motors and microtubule crosslinking protein MAP65. *Journal of physics. Condensed matter : an Institute of Physics journal*, 25:374103, 2013.

[85] Marileen Dogterom, Jacob W J Kerssemakers, Guillaume Romet-Lemonne, and Marcel E Janson. Force generation by dynamic microtubules. *Current opinion in cell biology*, 17:67–74, 2005.

[86] Ioannis G. Karafyllidis and Dimitris C. Lagoudas. Microtubules as mechanical force sensors. *BioSystems*, 88:137–146, 2007.

[87] Geoffrey M Cooper. *The Cell: A Molecular Approach*. Sunderland (MA): Sinauer Associates, 2nd edition, 2000.

[88] R. Niederman, P. C. Amrein, and J. Hartwig. Three-dimensional structure of actin filaments and of an actin gel made with actin-binding protein. *Journal of Cell Biology*, 96(May):1400–1413, 1983.

[89] P. a. Janmey, S. Hvidt, J. Kas, D. Lerche, a. Maggs, E. Sackmann, M. Schliwa, and T. P. Stossel. The mechanical properties of actin gels: Elastic modulus and filament motions. *Journal of Biological Chemistry*, 269(51):32503–32513, 1994.

[90] Anne-cécile Reymann, Rajaa Boujemaa-paterski, Jean-louis Martiel, Wenxiang Cao, Harvey F Chin, Enrique M De La Cruz, Manuel Théry, and Laurent Blanchoin. Actin Network Architecture Can Determine Myosin Motor Activity. *Science*, 336(6086):1310–1314, 2012.

[91] Clarence E Chan and David J Odde. Traction dynamics of filopodia on compliant substrates. *Science (New York, N.Y.)*, 322(December):1687–1691, 2008.

[92] Joseph P. Califano, Cynthia A., and Reinhart-King. Substrate Stiffness and Cell Area Predict Cellular Traction Stresses in Single Cells and Cells in Contact. *Cell Mol Bioeng*, 3(1):68–75, 2010.

[93] J. Bereiter-Hahn. Mechanics of crawling cells. *Medical Engineering and Physics*, 27(April):743–753, 2005.

[94] Revathi Ananthakrishnan and Allen Ehrlicher. The forces behind cell movement. *International Journal of Biological Sciences*, 3(5):303–317, 2007.

[95] T. Oliver, M. Dembo, and K. Jacobson. Traction forces in locomoting cells. *Cell Motility and the Cytoskeleton*, 31(3):225–240, 1995.

[96] Thomas Grevesse, Marie Versaevel, Géraldine Circelli, Sylvain Desprez, and Sylvain Gabriele. A simple route to functionalize polyacrylamide hydrogels for the independent tuning of mechanotransduction cues. *Lab on a chip*, 13(5):777–80, 2013.

[97] Dana Giulian and T J Baker. Characterization of ameboid microglia isolated from developing mammalian brain. *The Journal of neuroscience : the official journal of the Society for Neuroscience*, 6(8):2163–2178, 1986.

[98] KEND McCARTHY and J De Vellis. Preparation of separate astroglial and oligodendroglial cell cultures from rat cerebral tissue. *The Journal of cell biology*, 85(June), 1980.

[99] Talal M. Fael Al-Mayhani, Siolian L R Ball, Jing Wei Zhao, James Fawcett, Koichi Ichimura, Peter V. Collins, and Colin Watts. An efficient method for derivation and propagation of glioblastoma cell lines that conserves the molecular profile of their original tumours. *Journal of Neuroscience Methods*, 176:192–199, 2009.

[100] Daniel Koch, William J Rosoff, Jiji Jiang, Herbert M Geller, and Jeffrey S Urbach. Strength in the periphery: growth cone biomechanics and substrate rigidity response in peripheral and central nervous system neurons. *Biophysical journal*, 102(3):452–60, 2012.

[101] Benedikt Sabass, Margaret L Gardel, Clare M Waterman, and Ulrich S Schwarz. High resolution traction force microscopy based on experimental and computational advances. *Biophysical journal*, 94(1):207–20, 2008.

[102] Timo Betz. *Actin Dynamics and Forces of Neuronal Growth*. PhD thesis, University of Leipzig, 2007.

[103] L.D. Landau and E.M. Lifshitz. Theory Of Elasticity. In *Course of Theoretical Physics*, volume Vol. 7, 2n. Pergamon Press, Oxford, UK, 1970.

[104] James P Butler, Iva Marija Tolić-Nø rrelykke, Ben Fabry, and Jeffrey J Fredberg. Traction fields, moments, and strain energy that cells exert on their surroundings. *American journal of physiology. Cell physiology*, 282(3):C595–605, 2002.

[105] Olivia du Roure, Alexandre Saez, Axel Buguin, Robert H Austin, Philippe Chavrier, Pascal Silberzan, and Benoit Ladoux. Force mapping in epithelial cell migration. *Proceedings of the National Academy of Sciences of the United States of America*, 102(7):2390–2395, 2005.

[106] Juan C Del Alamo, Ruedi Meili, Baldomero Alonso-Latorre, Javier Rodríguez-Rodríguez, Alberto Aliseda, Richard a Firtel, and Juan C Lasheras. Spatio-temporal analysis of eukaryotic cell motility by improved force cytometry. *Proceedings of*

the National Academy of Sciences of the United States of America, 104(33):13343–13348, 2007.

[107] Kazuhiko S K Uchida, Toshiko Kitanishi-Yumura, and Shigehiko Yumura. Myosin II contributes to the posterior contraction and the anterior extension during the retraction phase in migrating Dictyostelium cells. *Journal of cell science*, 116(Pt 1):51–60, 2003.

[108] Effie Bastounis, Ruedi Meili, Begoña Álvarez González, Joshua Francois, Juan C. Del Álamo, Richard a. Firtel, and Juan C. Lasheras. Both contractile axial and lateral traction force dynamics drive amoeboid cell motility. *Journal of Cell Biology*, 204(6):1045–1061, 2014.

[109] Nan Xia, Charles K Thodeti, Tom P Hunt, Qiaobing Xu, Madelyn Ho, George M Whitesides, Robert Westervelt, and Donald E Ingber. Directional control of cell motility through focal adhesion positioning and spatial control of Rac activation. *The FASEB journal : official publication of the Federation of American Societies for Experimental Biology*, 22(6):1649–1659, 2008.

[110] Ying-Li Hu, Shaoying Lu, Kai W. Szeto, Jie Sun, Yingxiao Wang, Juan C. Lasheras, and Shu Chien. FAK and paxillin dynamics at focal adhesions in the protrusions of migrating cells. *Scientific Reports*, 4:1–7, 2014.

[111] Marion Ghibaudo, Alexandre Saez, Léa Trichet, Alain Xayaphoummine, Julien Browaeys, Pascal Silberzan, Axel Buguin, and Benoît Ladoux. Traction forces and rigidity sensing regulate cell functions. *Soft Matter*, 4(9):1836, 2008.

[112] Sangyoon J. Han, Kevin S. Bielawski, Lucas H. Ting, Marita L. Rodriguez, and Nathan J. Sniadecki. Decoupling substrate stiffness, spread area, and micropost density: A close spatial relationship between traction forces and focal adhesions. *Biophysical Journal*, 103(4):640–648, 2012.

[113] Pere Roca-Cusachs, Armando del Rio, Eileen Puklin-Faucher, Nils C Gauthier, Nicolas Biais, and Michael P Sheetz. Integrin-dependent force transmission to the extracellular matrix by α-actinin triggers adhesion maturation. *Proceedings of the National Academy of Sciences of the United States of America*, 110(15):E1361–70, 2013.

[114] Iva Marija Tolic-Norrelykke and Ning Wang. Traction in smooth muscle cells varies with cell spreading. *Journal of Biomechanics*, 38(7):1405–1412, 2005.

[115] Benjamin L. Bangasser, Steven S. Rosenfeld, and David J. Odde. Determinants of maximal force transmission in a motor-clutch model of cell traction in a compliant microenvironment. *Biophysical Journal*, 105(3):581–592, 2013.

[116] Padmavathy Rajagopalan, William a Marganski, Xin Q Brown, and Joyce Y Wong. Direct comparison of the spread area, contractility, and migration of balb/c 3T3 fibroblasts adhered to fibronectin- and RGD-modified substrata. *Biophysical journal*, 87(4):2818–2827, 2004.

[117] Stefka Gyoneva, Anna G. Orr, and Stephen F. Traynelis. Differential regulation of microglial motility by ATP/ADP and adenosine. *Parkinsonism and Related Disorders*, 15(SUPPL. 3):S195–S199, 2009.

[118] N Stence, M Waite, and M E Dailey. Dynamics of microglial activation: a confocal time-lapse analysis in hippocampal slices. *Glia*, 33:256–266, 2001.

[119] D. Ambrosi, a. Duperray, V. Peschetola, and C. Verdier. Traction patterns of tumor cells. *Journal of Mathematical Biology*, 58(1-2):163–181, 2009.

[120] Thomas D Pollard and John A Cooper. Actin, a Central Player in Cell Shape and Movement. *Science*, 326(5957):1208–1212, 2009.

[121] William E Allen, Gareth E Jones, Jeffrey W Pollard, and Anne J Ridley. Rho , Rac and Cdc42 regulate actin organization and cell adhesion in macrophages. *Journal of cell science*, 720:707–720, 1997.

[122] Y. Nakamura, Q. S. Si, and K. Kataoka. Lipopolysaccharide-induced microglial activation in culture: Temporal profiles of morphological change and release of cytokines and nitric oxide. *Neuroscience Research*, 35(2):95–100, 1999.

[123] R Drezek, A Dunn, and R Richards-Kortum. Light scattering from cells: finite-difference time-domain simulations and goniometric measurements. *Applied optics*, 38(16):3651–3661, 1999.

[124] E W Abrahamson, T J Borys, B D Gupta, R Jones, R Uhl, A Geistefer, and S Deshpande. Correlation of Cellular and Molecular Changes in Visual Photoreceptors by Light Scattering Relaxation Photometry. In Camille Sandorfy and Theophile Theophanides, editors, *Spectroscopy of Biological Molecules SE - 19*, volume 139 of *NATO ASI Series*, pages 385–407. Springer Netherlands, 1984.

[125] G C Salzman, J M Crowell, J C Martin, T T Trujillo, A Romero, P F Mullaney, and P M LaBauve. Cell classification by laser light scattering: identification and separation of unstained leukocytes. *Acta cytologica*, 19(4):374–377, 1975.

[126] P Latimer. Light scattering vs. microscopy for measuring average cell size and shape. *Biophysical journal*, 27(1):117–126, 1979.

[127] A Cunningham and G a Buonnacorsi. Narrow-Angle Forward Light-Scattering From Individual Algal Cells - Implications for Size and Shape-Discrimination in Flow-Cytometry. *Journal of Plankton Research*, 14(2):223–234, 1992.

[128] P. F. Mullaney, M. a. Van Dilla, J. R. Coulter, and P. N. Dean. Cell sizing: A light scattering photometer for rapid volume determination. *Review of Scientific Instruments*, 40(8):1029–1032, 1969.

[129] Philip J Wyatt and David T Phillips. Structure of Single Bacteria from Light Scattering. *Journal of Theoretical Biology*, 37(3):493–501, 1972.

[130] Valentina Peschetola, Valérie M. Laurent, Alain Duperray, Richard Michel, Davide Ambrosi, Luigi Preziosi, and Claude Verdier. Time-dependent traction force microscopy for cancer cells as a measure of invasiveness. *Cytoskeleton*, 70(4):201–214, 2013.

[131] Tim Demuth and Michael E Berens. Molecular mechanisms of glioma cell migration and invasion. *Journal of neuro-oncology*, 70(2):217–228, November 2004.

[132] Donald E. Ingber. Cellular mechanotransduction: putting all the pieces together again. *The FASEB Journal*, 20:1407–1417, 2006.

[133] Hayden Huang, Roger D Kamm, and Richard T Lee. Cell mechanics and mechanotransduction: pathways, probes, and physiology. *American journal of physiology. Cell physiology*, pages 1–11, 2004.

[134] Jodi L. Smith and Gary C. Schoenwolf. Neurulation: Coming to closure. *Trends in Neurosciences*, 20(97):510–517, 1997.

[135] Keiji Itoh and Sergei Y Sokol. *Early Development of Epidermis and Neural Tissue*. Elsevier Inc., second edition, 2015.

[136] Richard H Finnell, Timothy M George, and Laura E Mitchell. *Chapter 114 – Neural Tube Defects*. Elsevier, sixth edition, 2013.

[137] S Cowchock. *Neural tube defects.*, volume 19. Elsevier Inc., second edition, 2015.

[138] Richard Idro, Kevin Marsh, Chandy C. John, and Charles R J Newton. Cerebral malaria: Mechanisms of brain injury and strategies for improved neurocognitive outcome. *Pediatric Research*, 68(4):267–274, 2010.

[139] Krister Kristensson. *Infections and Nervous System Dysfunction*. Elsevier Inc., 2015.

[140] José Eymard Homem Pittella. *Pathology of CNS parasitic infections*, volume 114. Elsevier B.V., first edition, 2013.

[141] David a Hafler. Science in medicine Multiple sclerosis. *Natural History*, 113(6):788–794, 2004.

[142] Harald Hampel, David Prvulovic, Stefan Teipel, Frank Jessen, Christian Luckhaus, Lutz Frölich, Matthias W. Riepe, Richard Dodel, Thomas Leyhe, Lars Bertram, Wolfgang Hoffmann, and Frank Faltraco. The future of Alzheimer's disease: The next 10 years. *Progress in Neurobiology*, 95:718–728, 2011.

[143] Vincent J. Miele, Manohar M. Panjabi, and Edward C. Benzel. *Anatomy and biomechanics of the spinal column and cord*, volume 109. Elsevier B.V., first edition, 2012.

[144] W. Gomes-Leal, D. J. Corkill, M. a. Freire, C. W. Picanço-Diniz, and V. H. Perry. Astrocytosis, microglia activation, oligodendrocyte degeneration, and pyknosis following acute spinal cord injury. *Experimental Neurology*, 190:456–467, 2004.

[145] Anthony S. Burns, Ralph J. Marino, Adam E. Flanders, and Heather Flett. *Clinical diagnosis and prognosis following spinal cord injury*, volume 109. Elsevier B.V., first edition, 2012.

[146] J. Silver, K. P. Horn, S. a. Busch, and a. L. Yonkof. Axonal regeneration: Role of the extracellular matrix and the glial scar. *Encyclopedia of Neuroscience*, 43:1173–1180, 2010.

Statutory Declaration

I declare that I have authored this Thesis independently, that I have not used other than the declared sources/resources, and that I have explicitly marked all material, which has been quoted by the relevant reference.

date

signature

A. Formation and pathologies of the nervous system

The formation of the nervous system includes a sequence of steps. During early embryonic development in vertebrates the three primary germ layers ectoderm, mesoderm and endoderm are formed. The central and peripheral nervous system derive from the ectoderm, the outermost layer of the embryo. The process of forming the nervous system begins with the formation of the neural plate from the dorsal part of the ectoderm [134, 135]. The neural plate subsequently folds to become the neural tube, a process called neurulation. The neural tube divides further and differentiates into the brain and the spinal cord.

There are numerous pathologies of the nervous system. Most of these disorders can be linked to structural defects, trauma, infections, degeneration or tumors.

The initiation of disorder can begin during the development of the nervous system. Neural tube defects (NTDs) are common malformations that are due to complications in the neurulation during embryogenesis. As a result, the neural tube does not close entirely. NTDs can lead to a miscarriage, infant death and severe disabilities [136, 137].

Infections, such as cerebral malaria and rabies are another threat to the functionality of the nervous system [138, 139]. Pathogens can invade the nervous system, leading to varies dysfunctions depending on the affected region [140].

Several diseases of the CNS are associated to inflammatory reactions. One of the most common is multiple sclerosis (MS). The result of MS are plaques and damaged myelin sheaths leading to a partial impairment of neuronal signaling [141]. Since (irreversible) degeneration appears in the course of multiple sclerosis, it can also be characterized as a progressive neurodegenerative disorder.

Alzheimer's disease is an irreversible neurodegenerative disorder of the brain that can lead to the partial loss of cognitive functions, its final stage being dementia [142].

A structural defect affecting the spinal cord is a spinal cord injury (SCI). Depending on the location of the lesion, SCIs might be extremely debilitating. During trauma, the spinal cord is deformed due to compressive loads, shear loads, tensile loads, bending loads or a combination of the aforementioned [143]. If the imposed deformations exceed the physiological limit, they can cause a neurological dysfunction of the spinal cord. Neurons that were connected prior to trauma are separated and the signaling pathway is interrupted. Even cells that are not directly affected through the primary insult, can be perturbed through secondary degeneration [144]. Complete functional recovery after SCI is rare [145]. One of the main reasons is that neurons of the CNS are not able to regenerate after injury [146]. This inability is believed to be influenced by a variety of factors, including

the immediate inflammatory reaction and glutamate-mediated excitotoxicity (cell death or damage of neurons) [144]. Microglia play an important role in the sensing of pathological events, the inflammatory response and the regenerative process [40].

B. Protocols

B.1. PAA gels with beads

⇒ **Gels should be made the day before you plan to put cells on them!**

Before starting:

1. Weigh out *APS* (from cupboard) into small tube and dilute with ddH_2O (prepare fresh each time gels are made)
   - 0.01 g in $100\mu L$ ddH_2O
   - OR 0.02 g in $200\mu L$ ddH_2O
2. Take $500\mu L$ aliquot of 5% *glutaraldehyde* stock solution from -20 $^\circ C$ freezer
3. Take two $7ml$ vials for dilution
4. Take aliquots of 40% *acrylamide*, 100% *hydroxyacrylamide*, and 2% *bis-acrylamide* from 4°C fridge

In gel lab:

1. Cover two round *Petri* dishes with *Parafilm*
2. Clean 22 mm round "bottom" cover slips by dipping into 70% *ethanol* (OR using the ethanol spray) and water, beginning and ending with *ethanol*. Dry with *kimwipe*.
3. Clean again with cotton tip dipped in $0.1M$ $NaOH$ solution. Dry with *kimwipe*.
   - *NaOH: Sodium hydroxide, to make the glass surface hydrophilic*
4. **[FUME HOOD]** Place bottom cover slips on *parafilmed Petri* dish *WITH *NaOH* TREATED SIDE UP*.
   - Pipette 200-400 μL $APTMS$ onto one side of cover slips
     - Cover slips must be completely coated
     - Leave in hood 3 minutes
     - If left too long *APTMS* will corrode the glass!

- *APTMS: (3-Aminopropyl)trimethoxysilane, the goal of silanization is to form bonds across the interface between mineral components (glass) and organic components (gel)*

5. **[FUME HOOD]** Remove excess *APTMS*. Rinse thoroughly with ddH_2O (hold with forceps)
   - Rinse forceps and *Petri* dish too
   - Rinse again using the tab in the main lab
   - Dry all; place back on *Petri* dish WITH TREATED SIDE UP
   - Excess *APTMS* will react with *glutaraldehyde*, forming an orange precipitate $\rightarrow$ not good for cells
   - DO NOT touch treated side hereafter
6. **[FUME HOOD]** Dilute $500\mu l$ *Glutaraldehyde* with $4.5ml$ ddH_2O
   - Cover the bottom cover slips completely with diluted *glutaraldehyde*
   - Leave in hood 30 minutes.
   - *Glutaraldehyde: chemical crosslinking of PAA gel*
7. Meanwhile, prepare 19 mm ("top") coverslips:
   - Clean with ethanol and water
   - Place in 2nd Parafilmed Petri dish and pipette *RainX* solution on one side to completely cover.
   - Leave for 5-10 minutes, remove excess, then dry
   - *REMEMBER TREATED SIDE!*
   - *RainX: makes surface hydrophobic*
8. **[FUME HOOD]** prepare gel solutions for the desired stiffness:
   a) Make up *acrylamide* stock solution:
      - $500\mu L$ of 40% *acrylamide* + $65\mu L$ of 100% *hydroxy-acrylamide* (BE AWARE: *Hydroxy-acrylamide* is very viscous, need to pipette it slowly)
      - *Acrylamide: used to form polyacrylamide*
      - *Hydroxy-acrylamide: induces negative charge on the gel surface so that positively charged Poly-D-Lysine can bind to it*

   b) Prepare Gel Premix: $500\mu L$ of *acrylamide* stock solution from a) + $250\mu L$ 2% *bis-acrylamide*

   c) Add Gel Premix and Beads (VORTEX them before adding) to 100% PBS to make final gel solution for desired stiffness (total volume $500\mu L$):

Stiffness (Shear modulus G')(Pa)	**Volume of 100% PBS** (μL)	**Volume of Gel Premix** (μL)	**Beads** (μL)
~ 100	437	53	10
~ 200	435	55	10
~ 300	432	58	10
~ 1000	415	75	10
~ 2000	400	90	10
~ 10000	340	150	10

d) Vortex mixture properly & place into US-bath for 30 seconds to separate the beads (switch on de-gas setting)

e) De-gas final gel mixture in vacuum desiccator for 7-10 minutes ($\sim 300mbar$)

- Note: this will make $500\mu L$ of final gel mixture. This is enough volume for many (>20) gels but stiffer gels will set more quickly, so need to take this into account!!

9. **[FUME HOOD]** After 30 minutes, remove excess *glutaraldehyde* from bottom cover slips, rinse 2-3 times with ddH_2O. Dry with aerosol spray.

10. Prepare pipettes, bring tips, gel premixes and coverslips to hood, etc.

11. To each $500\mu L$ of final gel solution, add $1.5\mu L$ *TEMED* and $5\mu L$ *APS* solution
    - Mix gently but quickly with $1mL$ pipette (avoid introducing air bubbles)
    - Pipette small drops onto bottom coverslips. (Rajesh uses $8\mu L$)
    - *APS: Ammonium persulfate: oxidizing agent for polymerization*

12. Gently lower top coverslips onto gel drops, with the *RainX* treated side facing down

13. Turn top coverslips upside down so that beads can move downwards (should be close to the substrate surface

14. When the remaining gel premix has polymerised in *eppendorf* tubes (start checking after 10 minutes), place gels (with both coverslips attached) into 100% *PBS*
    - Wait 3-5 minutes, then gently slip off the top coverslips
    - Place each gel in individual wells of a 6-well plate

15. Wash 2 times with sterile 100 % *PBS*

16. To sterilize gels, place uncovered under *UV* (in small amount of 100% *PBS* to prevent drying) for 20 min (or longer if using for long-term cultures)

17. To functionalise the gels for cell cultures:

a) **Poly-D-lysine (PDL)**: incubate overnight in $100\mu g/mL$ solution (keep covered and seal with *Parafilm*, use a few mL of solution to prevent drying)
   - Wash 2-3 times in 100% PBS, 15-30 minutes each.

b) OPTIONAL (FOR NEURONS): **Laminin**: incubate for ~ 2 hours in $1\mu g/mL$ solution
   - Rinse briefly once or twice in 100% *PBS*
   - Remove *PBS* and replace with desired cell culture medium
   - Allow gels to equilibrate for at least 10-15 minutes. They can now be used for cell culture

- *PDL and Laminin: cell adhesion molecules*

B.2. Preparation of Microglia

⇒ **Instructions for microglia that are kept in petri-dishes**

Cold shake off

1. Shake off microglia at 4 degrees (about 400 rpm) for 20-30 min
   - If cells are still attached, shake them longer!
2. Transfer cells & medium from petri-dish to $15ml$ tube using pipette
   - Use pipette with medium to wash of cells from surface
3. Centrifuge cell-medium mixture for 1 min at 500 rpm
4. Remove medium without disturbing cell precipitate at the bottom of the tube
5. Disperse cells by hitting the bottom of the tube
6. Add about $2ml$ of fresh medium (*DMEM+FBS*) to each tube
7. Shake tubes lightly and distribute cell-medium mixture evenly on dishes for imaging

Trypsin shake off

1. Replaced medium by 10mL of a 9:1 DMEM medium (Not FBS containing DMEM) to trypsin solution
   - Shake off in incubator for 5 to 20 minutes
2. Add 5 mL of FBS to stop the trypsin activation
3. Centrifuge at 1000 rpm for 7 minutes
4. Remove supernatant and resuspend pellet in 1mL DMEM+10$\%$FBS medium

B.3. Traction Force Microscopy

Preparing the Microscope

⇒ **Start 3 hours before experiment for pH & temperature to adjust**
(only for mammalian cells)

1. Fill up bottle in chamber with ddH_2O
   - Change lid to sensor lid (tube should be inside the water)
   - Connect sensor
   - Connect tube with insulation to sensor lid
2. Switch on compressor (under table)
3. Open CO_2 cylinder
   - Open valve on top
   - Set valve on the side to 1 bar
   - Set second valve to less than 1 bar
4. Switch on OkoTouch
   - for mammalian cells:
     - $temperature = 37°C$
     - $CO_2 = 5\%$
     - $humidity = 95\%$
5. Switch on shock absorber under micrscope (all switches)
6. Adjust small chamber
   - Connect tube
   - Place temperature sensor close to small chamber
   - Wet foam with tab water and place inside chamber

Starting the Microscope setup

1. Switch on cooling system for camera (blue box)
2. Switch on cooling system for microscope (white Nikon box)
3. Switch on light source (Nikon G-HGFI box)

Operating the Microscope

1. Open *NIS-Element* Software
2. Place petri dish under lense, BE CAREFUL not to touch the lense
3. Use small magnification (e.g. 10X) to identify region of interest
   - Make sure shutter is set to binocular
   - Wheels on the right move in x,y-direction
   - Wheels on the left for z-direction
4. Take objective with desired magnification (BE CAREFUL not to touch the lense)
   - Focus
   - Change shutter to camera
5. Using *NIS-Element* Software:
   - Select *BF* (Bright Field)
   - Adjust brightness
   - Focus
   - Select *TFM F* to use fluorescence, make sure shutter of light source is open

Acquiring images using *NIS-Element* Software

1. Select ND-Acquisition:
   - Tick *TFM F* (will adjust the focus after every 10 steps)
   - Tick *TFM F* (will take one BF image and one F image per minute)
   - Tick *TFM BF* (reference BF image)
   - Select Advanced for: *TFM F(TFM F)*
   - Select Autofocus: *Step in Range* $\rightarrow$ define: *step*: $0.5\mu m$, *range*: $2\mu m$ (keep minimum) $\rightarrow$ save and close
   - Give right path & filename
   - Click *One Time Loop* to see that everything is working
   - Click *Run now*

After use

1. CAREFULLY clean lense with isopropanol
2. Use lense cleaning paper to clean the lense
3. replace sensor lid of ddH_2O-bottle with standard lid

B.4. Staining Microglia and Glioblastoma cells

Fixing cells

1. Remove medium gently and wash with PBS
2. Cover cells with 4% paraformaldehyde + 96% PBS (100%) solution
   - Be careful not to wash of the cells
   - Leave for 10 - 20 min
   - *paraformaldehyde: cross-links amino acids*
3. Remove paraformaldehyde-PBS solution and cover cells with 0.1% Triton
   - Leave it for 5 min (not longer!)
   - *Triton: makes cell membrane permeable*
4. Remove solution and wash 3-4 times with 100% PBS

Staining for Actin

1. Apply Alexa-488-phalloidin 2 Units/300μl (1 Unit = $5\mu l$)
   - Leave for 1 hour
   - $[fluorophore] - [wavelength] - [substance\ that\ attaches\ to\ actin]$
2. Stain with Dapi to see nuclei
3. Wash 3 times with PBS (15 min each time)

Staining with OX42

1. Apply 10% goat serum + 90% PBS
   - Leave for 1 hour
2. Primary antibody OX42 (1:200 in PBS) over night
3. Wash 3 times with PBS (15 min each time)
4. Apply secondary antibody goat anti-mouse (1:500 in PBS) for 1 hour
5. Add Dapi if needed

C. ImageJ Macro for pre-processing

```
//-------------------------------------------------------------------------------------------------
//-------------------------------------------------------------------------------------------------
//  Macro that reads .nd2 files and reference images, processes them and stores
//  them in folders. Output is ready to use for Koch's TFM code
//
//  Author: Lars Bollmann, Graz University of Technology
//          bollmann@student.tugraz.at
//
//  Input: folder containing .nd2 files and .png reference images with according
//         names:
//
//          [NUMBER]_Pa_[CELL TYPE]_[NUMBER]hr.nd2
//          [NUMBER]_Pa_[CELL TYPE]_[NUMBER]hr.png
//
//  Last modification: 24/11/2014
//
//-------------------------------------------------------------------------------------------------
//-------------------------------------------------------------------------------------------------

ref_image = 20; // reference slice for stack alignment

//-------------------------------------------------------------------------------------------------
// Main loop
//-------------------------------------------------------------------------------------------------

input = getDirectory("Input directory");

// input format: /User/LarsBollmann/Desktop/Test/
processFolder(input);

//-------------------------------------------------------------------------------------------------
// Function definitions
//-------------------------------------------------------------------------------------------------

function processFolder(input) {
    list = getFileList(input);
    for (i = 0; i < list.length; i++) {
        // Read .nd2 files, create according folders and save images
        if(endsWith(list[i], ".nd2")){
            folder_name = substring(list[i], 0, lengthOf(list[i])-4);
            File.makeDirectory(input);
            folder = input + folder_name;
            File.makeDirectory(folder);
            bead_folder = folder +"/beads/";
            tmp_bead_folder = folder +"/tmpbeads/";
            File.makeDirectory(bead_folder);
            File.makeDirectory(tmp_bead_folder);
            cell_folder = folder +"/cells/";
            File.makeDirectory(cell_folder);
            OpenSavePNG(folder_name, tmp_bead_folder);
            OpenSaveND2(list[i], input, cell_folder, tmp_bead_folder);
            ProcessImages(folder_name,tmp_bead_folder ,bead_folder);
            FindCopyDeleteRef(folder, folder_name, bead_folder);
        }
    }
}
```

```
function OpenSaveND2(file, input, cell_folder, bead_folder){
    file_id = input + file;
    // file format: 1000_Pa_MG_2hr.nd2
    // Open .nd2 file
    run("Bio-Formats Windowless Importer", "open="+ file_id );
    // close stack with images for focus adjustment
    selectWindow(file+" - C=0");
    close();
    // Process cell images and save them
    selectWindow(file+" - C=2");
    run("8-bit");
    run("Enhance Contrast...", "saturated=0.4");
    run("Image Sequence... ", "format=PNG save="+cell_folder);
    close();
    // Make bead images 8 bit and save them
    selectWindow(file+" - C=1");
    run("8-bit");
    run("Image Sequence... ", "format=PNG save="+bead_folder);
    close();
}

function OpenSavePNG(folder_name,bead_folder){
    for (i1 = 0; i1 < list.length; i1++) {
        // Open, process and save reference image
        if(list[i1] == folder_name + ".png"){
            open(list[i1]);
            run("8-bit");
            // save reference image to folder/beads
            saveAs(".png", bead_folder + "z_" +list[i1]);
            close();
        }
    }
}

function ProcessImages(folder_name,tmp_bead_folder, bead_folder){
    run("Image Sequence...", "open="+tmp_bead_folder+" sort");
    // Unsharpen mask
    run("Unsharp Mask...", "radius=1 mask=0.60 stack");
    // Stabilize bead images
    run("Image Stabilizer",      "transformation=Translation maximum_pyramid_levels=1"
    + "template_update_coefficient=0.90 maximum_iterations=200 error_tolerance=0.0000001");
    width = getWidth();
    height = getHeight();
    x_coord = toString( floor(0.08 * width));
    y_coord = toString(floor(0.08 * height));
    rect_width = toString(floor(0.8 * width));
    rect_height = toString(floor(0.8 * height));
    param1 = "method=5 windowsizex="+rect_width+" windowsizey="+rect_height+" x0="+x_coord+"
             y0="+y_coord;
    param2 = " swindow=0 subpixel=false itpmethod=0 ref.slice="+ref_image+" show=true";
    run("Align slices in stack...",param1+param2);
    run("Image Sequence... ", "format=PNG name=beads save="+bead_folder);
    close();
    // Delete temporary list
    tmp_list = getFileList(tmp_bead_folder);
    for (i=0; i<tmp_list.length; i++){
        File.delete(tmp_bead_folder+tmp_list[i]);
    }
    File.delete(tmp_bead_folder);
}
```

```
function FindCopyDeleteRef(folder, folder_name, bead_folder ){
    image_list = getFileList(bead_folder);
    max_ind = image_list.length - 1;
    nr_string = toString(max_ind);
    length_nr = lengthOf(nr_string);
    // Find reference image
    if(length_nr == 1){
        ref_image ="beads000"+max_ind +".png";
    }
    if(length_nr == 2){
        ref_image ="beads00"+max_ind +".png";
    }
    if(length_nr == 3){
        ref_image ="beads0"+max_ind +".png";
    }
    if(length_nr == 4){
        ref_image ="beads"+max_ind +".png";
    }
    for (i2 = 0; i2 < image_list.length; i2++) {
        if(image_list[i2] == ref_image){
            save_to = folder +"/"+ image_list[i2];
            save_from = bead_folder + image_list[i2];
            File.copy(save_from,save_to);
            File.delete(save_from);
        }
    }
}
```

D. MATLAB scripts

D.1. Combining TFM results

```
%-------------------------------------------------------------------------
%-------------------------------------------------------------------------
% Combine TFM RESULTS
%
% Input: Folder containing TFM experiments
% Output: .mat files containing desired results
%
% Author: Lars Bollmann
% Email: bollmann@student.tugraz.at
% Graz University of Technology - Jan 2015
%
%
% Last modification: 12.01.2015, Lars Bollmann
%
%-------------------------------------------------------------------------
%-------------------------------------------------------------------------

%-------------------------------------------------------------------------
% Initialize
%-------------------------------------------------------------------------

clear all;
addpath('Subroutines');

init_path = fullfile(...
'/Users/LarsBollmann/Documents/Studium/Cambridge/Experiments/TFM/Results');
data_path = uigetdir(init_path,...
'Select directory containing TFM data (Format: 20XX_XX_XX)');

% Extract only folders containing experimental data
%-------------------------------------------------------------------------
folder_list = FindFolders(data_path);

clear init_path;

% Process one experiment after the other
%-------------------------------------------------------------------------
for ex_id = 1:1:length(folder_list)
folder_path = strcat(data_path,'/',folder_list(ex_id));

% Identify result folder (format: 'results' or 'traction_analysis...')
%-------------------------------------------------------------------
subfolder_list = FindFolders(folder_path{1,1});
subfolder_list(ismember(subfolder_list,{'beads','cells'}))=[];

if(~isempty(subfolder_list))
    result_folder = strcat(folder_path{1,1},'/',subfolder_list{1,1});
else
   break;
end

% Process one cell folder after the other
%-------------------------------------------------------------------
cell_folder_list = FindFolders(result_folder);

for cell_id = 1:1:length(cell_folder_list)
```

```
        result_file = strcat(result_folder,'/',...
            cell_folder_list{cell_id,1},'/','traction_analysis.mat');

        load(result_file,'results');


        % Find correct .mat file to save data & determine variable name
        %--------------------------------------------------------------------

        id_mat = {'100Pa','300Pa','1000Pa','2000Pa','10000Pa'};

        for i = 1:1:length(id_mat)
            id = strfind(folder_list{ex_id}, id_mat{i});
            if ~isempty(id)
                stiff_ind = i;
            end
        end

        sep_dat = strsplit(data_path,'/');
        date_id = sep_dat{length(sep_dat)};

        sep_id = strsplit(folder_path{1},'/');
        stiff__time_id = sep_id{length(sep_id)};

        variable_name = strcat('E',date_id,'_',stiff__time_id,'_',...
            cell_folder_list{cell_id});

        save_file = strcat(pwd,'/','CombinedResults.mat');


        id_save_mat = {'Pa100','Pa300','Pa1000','Pa2000','Pa10000'};

        if exist('CombinedResults.mat', 'file') == 2
            load('CombinedResults.mat');
        end

        % Save peak and mean stress
        %--------------------------------------------------------------------
        combined.(id_save_mat{stiff_ind}).(variable_name).peak_stress = ...
            results.v_Fmax;
        combined.(id_save_mat{stiff_ind}).(variable_name).mean_stress = ...
            results.v_Fmean;

        % Save max and mean deformation
        %--------------------------------------------------------------------
        combined.(id_save_mat{stiff_ind}).(variable_name).max_def = ...
            results.max_deformation_gauss;
        combined.(id_save_mat{stiff_ind}).(variable_name).mean_def = ...
            results.mean_deformation_gauss;

        if exist('CombinedResults.mat', 'file') == 2
            save(save_file,'combined','-append');
        else
            save(save_file,'combined');
        end

        clear results peak_stress mean_stress;
    end
    end
```

D.2. TFM post-processing

```
%-------------------------------------------------------------------------
%-------------------------------------------------------------------------
% Post Processing script for TFM data
%
% Input: Folder containing .mat files
% Output: Selected display option
%
% Author: Lars Bollmann
% Email: bollmann@student.tugraz.at
% Graz University of Technology - Jan 2015
%
%
% Last modification: 13.01.2015, Lars Bollmann
%
%-------------------------------------------------------------------------
%-------------------------------------------------------------------------

clear all;
addpath('Subroutines','Results');

%-------------------------------------------------------------------------
% Parameters
%-------------------------------------------------------------------------

% name of input file
input_file = 'MG_IM_LPS.mat';

% name of excel file (for write_to_excel and write_for_R):
write_file_name = 'InvertedMG_LPS.xlsx';

% requested variables:
var_req = {'dis_mean', 'dis_peak', 'stress_mean', 'stress_peak'};

% results to be included:
variable_list = {'peak_stress'; 'mean_stress'};

% Sampling frequency
Fs = 1/30;


%-------------------------------------------------------------------------
% Options
%-------------------------------------------------------------------------

write_to_excel = 0;
write_for_R = 1;
plot_stress_box = 0;
plot_dis_box = 0;
plot_super_power_spec = 0;

%-------------------------------------------------------------------------
% Initialize
%-------------------------------------------------------------------------


% Initialization of POI Libs: Only if xlwrite for Mac is used
% Add Java POI Libs to matlab javapath
%-------------------------------------------------------------------------
javaaddpath('poi_library/poi-3.8-20120326.jar');
javaaddpath('poi_library/poi-ooxml-3.8-20120326.jar');
javaaddpath('poi_library/poi-ooxml-schemas-3.8-20120326.jar');
```

```
javaaddpath('poi_library/xmlbeans-2.3.0.jar');
javaaddpath('poi_library/dom4j-1.6.1.jar');
javaaddpath('poi_library/stax-api-1.0.1.jar');
%-------------------------------------------------------------------------


init_path = fullfile(pwd);
load(input_file);


% Access every stiffness
%-------------------------------------------------------------------------

stiff_list = fieldnames(combined);

for stiff_id = 1:1:length(stiff_list)

    sample_list = fieldnames(combined.(stiff_list{stiff_id}));

    stiffness_id = stiff_list{stiff_id};
% Process one sample after the other
%-------------------------------------------------------------------------
for sample_id = 1:1:length(sample_list)

    sample_name = sample_list{sample_id};

    variable_list = fieldnames(...
        combined.(stiff_list{stiff_id}).(sample_list{sample_id}));


    % Write data to excel sheet
    %---------------------------------------------------------------------
    if write_to_excel

        ToExcel(init_path, sample_id, write_file_name,...
        stiff_list{stiff_id}, 0,'A',{sample_name});


        for variable_id = 1:1:length(variable_list)
                % Write variable name in first column
                %-------------------------------------------------------
                ToExcel(init_path, sample_id, write_file_name, ...
                stiffness_id,variable_id,'A',{variable_list{variable_id}});

                % Write variable content next to name
                %-------------------------------------------------------

                data = combined.(stiff_list{stiff_id}). ...
                    (sample_list{sample_id}).(variable_list{variable_id});

                ToExcel(init_path, sample_id, write_file_name, ...
                stiffness_id,variable_id,'B',data);

        end
    end


    % Try finding selected results
    %---------------------------------------------------------------------

    try

    stress_peak_mean = mean(combined.(stiff_list{stiff_id}).(...
```

```
        sample_list{sample_id}).peak_stress);

    stress_avg_mean = mean(combined.(stiff_list{stiff_id}).(...
        sample_list{sample_id}).mean_stress);

    general_peak.(stiffness_id)(sample_id) = stress_peak_mean;
    general_mean.(stiffness_id)(sample_id) = stress_avg_mean;

    catch
        continue;
    end

    % Power spectrum
    %--------------------------------------------------------------------------

    if plot_super_power_spec
        input = combined.(stiff_list{stiff_id}).(...
        sample_list{sample_id}).peak_stress(1:70);

        T = 1/Fs;
        L = length(input);
        % time vector
        t = (0:L-1)*T;

        NFFT = 2^nextpow2(L);
        Y = fft(input,NFFT)/L;
        f = Fs/2*linspace(0,1,NFFT/2+1);

        spectrum.(stiffness_id)(sample_id,:) = 2*abs(Y(1:NFFT/2+1));

    end


    try

    dis_peak_mean = mean(combined.(stiff_list{stiff_id}).(...
        sample_list{sample_id}).max_def);

    dis_avg_mean = mean(combined.(stiff_list{stiff_id}).(...
        sample_list{sample_id}).mean_def);

    dis_peak.(stiffness_id)(sample_id) = dis_peak_mean;
    dis_mean.(stiffness_id)(sample_id) = dis_avg_mean;

    catch
        continue;
    end


end




end

% Delete all zero elements
%--------------------------------------------------------------------------
for stiff_id = 1:1:length(stiff_list)
    dis_peak.(stiff_list{stiff_id})(dis_peak.(stiff_list{stiff_id})==0)...
        = [];
    dis_mean.(stiff_list{stiff_id})(dis_mean.(stiff_list{stiff_id})==0)...
        = [];
```

```
    general_peak.(stiff_list{stiff_id})(general_peak. ...
        (stiff_list{stiff_id})==0)= [];
    general_mean.(stiff_list{stiff_id})(general_mean. ...
        (stiff_list{stiff_id})==0)= [];
end



if write_for_R

    letters = ['A' 'B' 'C' 'D' 'E'];
    results.dis_mean = dis_mean;
    results.dis_peak = dis_peak;
    results.stress_peak = general_peak;
    results.stress_mean = general_mean;

    for var = 1:1:length(var_req)

        for i = 1:1:length(stiff_list)

            xlwrite(write_file_name,...
                {stiff_list{i}},var_req(var),[letters(i),'1']);
            xlwrite(write_file_name,(...
            results.(var_req{var}).(stiff_list{i}))',...
            var_req(var),[letters(i),'2']);


        end

    end

end



%%
if plot_stress_box

    figure
    subplot(1,2,1)

    group = [repmat({['G1, n=' num2str(length(general_peak1.Pa100))]},...
    length(general_peak1.Pa100), 1); ...
    repmat({['G2, n=' num2str(length(general_peak2.Pa100))]},...
    length(general_peak2.Pa100), 1); ...
     repmat({['G3, n=' num2str(length(general_peak3.Pa100))]},...
     length(general_peak3.Pa100), 1); ...
      repmat({['G1, n=' num2str(length(general_peak1.Pa300))]},...
      length(general_peak1.Pa300), 1); ...
    repmat({['G2, n=' num2str(length(general_peak2.Pa300))]},...
    length(general_peak2.Pa300), 1);...
 repmat({['G3, n=' num2str(length(general_peak3.Pa300))]},...
    length(general_peak3.Pa300), 1);...
    repmat({['G1, n=' num2str(length(general_peak1.Pa1000))]},...
      length(general_peak1.Pa1000), 1); ...
    repmat({['G2, n=' num2str(length(general_peak2.Pa1000))]},...
    length(general_peak2.Pa1000), 1);...
 repmat({['G3, n=' num2str(length(general_peak3.Pa1000))]},...
    length(general_peak3.Pa1000), 1)];

     boxplot([(general_peak1.Pa100)';(general_peak2.Pa100)'; ...
         (general_peak3.Pa100)'; (general_peak1.Pa300)';...
         (general_peak2.Pa300)'; (general_peak3.Pa300)';...
```

```
        (general_peak1.Pa1000)';...
        (general_peak2.Pa1000)'; (general_peak3.Pa1000)'],group)
    grid on;

    title('Peak stresses (Pa)')

    subplot(1,2,2)

    group = [repmat({['G1, n=' num2str(length(general_mean1.Pa100))]},...
    length(general_mean1.Pa100), 1); ...
    repmat({['G2, n=' num2str(length(general_mean2.Pa100))]},...
    length(general_mean2.Pa100), 1); ...
    repmat({['G3, n=' num2str(length(general_mean3.Pa100))]},...
    length(general_mean3.Pa100), 1); ...
    repmat({['G1, n=' num2str(length(general_mean1.Pa300))]},...
    length(general_mean1.Pa300), 1); ...
    repmat({['G2, n=' num2str(length(general_mean2.Pa300))]},...
    length(general_mean2.Pa300), 1);...
    repmat({['G3, n=' num2str(length(general_mean3.Pa300))]},...
    length(general_mean3.Pa300), 1);...
    repmat({['G1, n=' num2str(length(general_mean1.Pa1000))]},...
    length(general_mean1.Pa1000), 1); ...
    repmat({['G2, n=' num2str(length(general_mean2.Pa1000))]},...
    length(general_mean2.Pa1000), 1);...
    repmat({['G3, n=' num2str(length(general_mean3.Pa1000))]},...
    length(general_mean3.Pa1000), 1)];

    boxplot([(general_mean1.Pa100)';(general_mean2.Pa100)'; ...
        (general_mean3.Pa100)'; (general_mean1.Pa300)';...
        (general_mean2.Pa300)'; (general_mean3.Pa300)';...
        (general_mean1.Pa1000)';...
        (general_mean2.Pa1000)'; (general_mean3.Pa1000)'],group)
    grid on;

    title('Average stresses (Pa)')
end

if plot_dis_box


    figure
    subplot(1,2,1)

    group = [repmat({['LPS, n=' num2str(length(dis_peakLPS.Pa100))]},...
    length(dis_peakLPS.Pa100), 1); ...
    repmat({['Control, n=' num2str(length(dis_peak.Pa100))]},...
    length(dis_peak.Pa100), 1); ...
    repmat({['LPS, n=' num2str(length(dis_peakLPS.Pa300))]},...
    length(dis_peakLPS.Pa300), 1); ...
    repmat({['Control, n=' num2str(length(dis_peak.Pa300))]},...
    length(dis_peak.Pa300), 1); ...
    repmat({['LPS, n=' num2str(length(dis_peakLPS.Pa1000))]},...
    length(dis_peakLPS.Pa1000), 1);...
    repmat({['Control, n=' num2str(length(dis_peak.Pa1000))]},...
    length(dis_peak.Pa1000), 1)];

    boxplot([(dis_peakLPS.Pa100)';(dis_peak.Pa100)'; ...
        (dis_peakLPS.Pa300)'; (dis_peak.Pa300)';...
        (dis_peakLPS.Pa1000)'; (dis_peak.Pa1000)'],group)
    grid on;

    title('Peak deformations (µm)')
```

```
    subplot(1,2,2)
    group = [repmat({['LPS, n=' num2str(length(dis_meanLPS.Pa100))]},...
    length(dis_meanLPS.Pa100), 1); ...
    repmat({['Control, n=' num2str(length(dis_mean.Pa100))]},...
    length(dis_mean.Pa100), 1); ...
    repmat({['LPS, n=' num2str(length(dis_meanLPS.Pa300))]},...
    length(dis_meanLPS.Pa300), 1); ...
    repmat({['Control, n=' num2str(length(dis_mean.Pa300))]},...
    length(dis_mean.Pa300), 1); ...
    repmat({['LPS, n=' num2str(length(dis_meanLPS.Pa1000))]},...
    length(dis_meanLPS.Pa1000), 1);...
    repmat({['Control, n=' num2str(length(dis_mean.Pa1000))]},...
    length(dis_mean.Pa1000), 1)];

    boxplot([(dis_meanLPS.Pa100)';(dis_mean.Pa100)'; ...
         (dis_meanLPS.Pa300)'; (dis_mean.Pa300)';...
         (dis_meanLPS.Pa1000)'; (dis_mean.Pa1000)'],group)


    grid on;

    title('Average deformations (µm)')

end


if(plot_super_power_spec)

   for i = 1:1:length(spectrum.Pa100)
       Pa100spectrum(i) = mean(spectrum.Pa100(:,i));

   end
   for i = 1:1:length(spectrum.Pa300)
       Pa300spectrum(i) = mean(spectrum.Pa300(:,i));

   end
   for i = 1:1:length(spectrum.Pa1000)
       Pa1000spectrum(i) = mean(spectrum.Pa1000(:,i));

   end
    subplot(3,1,1)
    plot(f,Pa100spectrum);
    subplot(3,1,2)
    plot(f,Pa300spectrum);
    subplot(3,1,3)
    plot(f,Pa1000spectrum);

end
```

D.3. Computing motion ratio and cell size

```
%--------------------------------------------------------------------------
%--------------------------------------------------------------------------
% MotionDetect
%
% Detects cells, determines cell area and area explored by the cell
% from time lapse images
%
% Input: Folder with bead and cell images
% Output: File defined by 'save_file' containing motion_ratio, size_cell
% and covered_area in (µm)^2
%
% Author: Lars Bollmann
% Email: bollmann@student.tugraz.at
% Graz University of Technology - Mar 2015
%
%
% Last modification: 13.03.2015, Lars Bollmann
%
%--------------------------------------------------------------------------
%--------------------------------------------------------------------------

clear all;
close all;

init_path = fullfile(...
'/Users/LarsBollmann/Documents/Studium/Cambridge/Experiments/TFM/Results');

data_path = uigetdir(init_path,...
'Select directory containing TFM data (Format: XXXPa_MG_XXhr)');

% Parameters
%--------------------------------------------------------------------------

% Nikon (with C-mount, 63X): 3*0.0763333333333 µm
% Zeiss (40X): 0.193 µm

pixel_size = 3*0.0763333333333;

save_file = ('combined.mat');


% read cell and bead folders
%--------------------------------------------------------------------------

cell_folder = strcat(data_path,'/cells/');
bead_folder = strcat(data_path,'/beads/');

cell_list = dir([cell_folder,'*.png']);
bead_list = dir([bead_folder,'*.png']);

nr_images = length(cell_list);


% Define range for analysis
%--------------------------------------------------------------------------


prompt = {'Define first image:',...
    ['Define last image, max:',num2str(nr_images)],'Stiffness: e.g. Pa100'};
dlg_title = 'Define sequence range';
def = {'1',num2str(nr_images),''};
num_lines = 1;
```

```
range = inputdlg(prompt,dlg_title,num_lines,def);

stiffness = range{3,1};
min = str2num(range{1,1});
max = str2num(range{2,1});

% find cell shape and superimpose to get static cell shape
%--------------------------------------------------------------------------

for im = min:1:max

    cell_im = imread([cell_folder,cell_list(im).name]);
    %figure, imshow(I), title('original image');


    [~, threshold] = edge(cell_im, 'sobel');
    fudgeFactor = 0.5;
    BWs = edge(cell_im,'sobel', threshold * fudgeFactor);
    se90 = strel('line', 3, 90);
    se0 = strel('line', 3, 0);
    BWsdil = imdilate(BWs, [se90 se0]);
    BWdfill = imfill(BWsdil, 'holes');
    BWnobord = imclearborder(BWdfill, 4);
    seD = strel('diamond',4);
    BWfinal = imerode(BWnobord,seD);
    BWfinal = imerode(BWfinal,seD);
    %figure, imshow(BWfinal), title('segmented image');

    BWfinal = im2uint8(BWfinal);
    if (im ~= min)
        superimp = superimp + BWfinal;
    else
        superimp = BWfinal;
        first_image = superimp;
    end

    %imwrite(superimp,[bead_folder,bead_list(im).name]);

end

% Show first image and superimposed image for user selection of cells to
% be analyzed
%--------------------------------------------------------------------------

first_image = im2bw(first_image);
superimp = im2bw(superimp);
figure;

subplot(1,3,1);
imshow(imread([cell_folder,cell_list(min).name]));
imwrite(imread([cell_folder,cell_list(min).name]),'cell.png');


subplot(1,3,2);
super_labeled = bwlabel(superimp);
imshow(super_labeled);
imwrite(super_labeled,'super.png');

subplot(1,3,3);
first_labeled = bwlabel(first_image);
imshow(first_labeled);
imwrite(first_labeled,'first.png');
```

```
answer = inputdlg('Enter number of cells to analyze:');
nr_cells = str2num(answer{1,1});


[coord_x, coord_y] = ginput(nr_cells);

% Computed solution for selected cells
%--------------------------------------------------------------------------

for i = 1:1:(nr_cells)

   first_image_cell_ids(i) = ...
       first_labeled(round(coord_y(i)),round(coord_x(i)));
   first_pixel_sum(i) = sum(first_labeled(:) == first_image_cell_ids(i));
   cell_size(i) = first_pixel_sum(i)*(pixel_size)^2;

   superimp_image_cell_ids(i) = ...
       super_labeled(round(coord_y(i)),round(coord_x(i)));
   super_pixel_sum(i) = sum(super_labeled(:) == superimp_image_cell_ids(i));
   covered_area(i) = super_pixel_sum(i)*(pixel_size)^2;


end

motion_ratio = super_pixel_sum./first_pixel_sum;

sep_dat = strsplit(data_path,'_');
dur_id = strcat(sep_dat{length(sep_dat)-1},sep_dat{length(sep_dat)});

name = strcat(dur_id,num2str(nr_cells));

if exist(save_file, 'file') == 2
     load(save_file);
end


results.(stiffness).(name).motion_ratio = motion_ratio;
results.(stiffness).(name).size_cell = cell_size;
results.(stiffness).(name).covered_area = covered_area;

save(save_file,'results');


close all;
```

D.4. Displaying motion ratio and cell size

```
%-------------------------------------------------------------------------
%-------------------------------------------------------------------------
% MotionDisplay
%
% Displays output from MotionDetect.m
%
% Input: .mat file containint motion_ratio, size_cell, covered_area
% Output: Plots
%
% Author: Lars Bollmann
% Email: bollmann@student.tugraz.at
% Graz University of Technology - Mar 2015
%
%
% Last modification: 13.03.2015, Lars Bollmann
%
%-------------------------------------------------------------------------
%-------------------------------------------------------------------------

clear all;

% motion_ratio, size_cell, covered_area
variable = 'size_cell';

addpath('Results')

load('Gliomas.mat');
stiffness_list = {'Pa100', 'Pa300', 'Pa1000'};


for a =1:1:length(stiffness_list)

id_list = fieldnames(results.(stiffness_list{a}));

for i=1:1:length(id_list)

    if (i == 1)
       motion_ratio = results.(stiffness_list{a}).(id_list{i}).(variable);
    else
       motion_ratio = horzcat(motion_ratio, ...
           results.(stiffness_list{a}).(id_list{i}).(variable));
    end
end

    combined.(stiffness_list{a}) = motion_ratio;

end

group = [repmat({['100 Pa, n=' num2str(...
    length(combined.(stiffness_list{1})))]},...
    length(combined.(stiffness_list{1})), 1);...
    repmat({['300 Pa, n=' num2str(...
    length(combined.(stiffness_list{2})))]},...
    length(combined.(stiffness_list{2})), 1);...
    repmat({['1000 Pa, n=' num2str(...
    length(combined.(stiffness_list{3})))]},...
    length(combined.(stiffness_list{3})), 1)];

figure
boxplot([combined.(stiffness_list{1})';...
    combined.(stiffness_list{2})';combined.(stiffness_list{3})'], group);
```